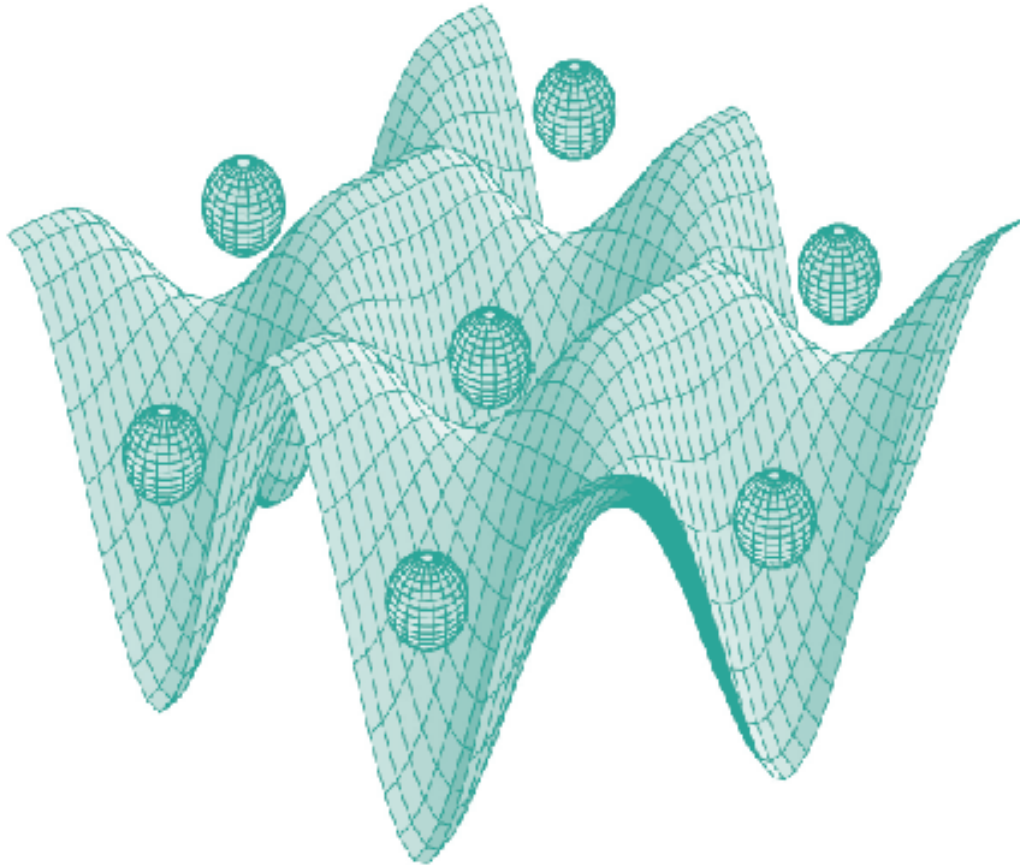




STUDIA UNIVERSITATIS
BABEȘ-BOLYAI



PHYSICA

2/2015

**STUDIA
UNIVERSITATIS BABEŞ-BOLYAI
PHYSICA**

**2/2015
December**

EDITORIAL OFFICE OF STUDIA UBB PHYSICA:

1, M. Kogălniceanu St., Cluj-Napoca, ROMANIA, Phone: +40 264 405300

http://www.studia.ubbcluj.ro/serii/physica/index_en.html

EDITOR-IN-CHIEF:

Professor Aurel POP, Ph.D., Babeş-Bolyai University, Cluj-Napoca, Romania

EDITORIAL BOARD:

Professor Simion AŞTILEAN, Ph.D., Babeş-Bolyai University, Cluj-Napoca, Romania

Professor Istvan BALLAI, Ph.D., The University of Sheffield, United Kingdom

Zoltan BALINT, Ph.D., Ludwig Boltzmann Institute Graz, Austria

Professor Titus BEU, Ph.D., Babeş-Bolyai University, Cluj-Napoca, Romania

Prof. Boldizsár JANKÓ, Ph.D., University of Notre Dame, USA

Professor Emil BURZO, Ph.D., Babeş-Bolyai University, Cluj-Napoca, Romania,
member of Romanian Academy

Professor Vasile CHIŞ, Ph.D., Babeş-Bolyai University, Cluj-Napoca, Romania

Professor Olivier ISNARD, Ph.D., University J. Fourier & Institut Neel, Grenoble,
France

Professor Ladislau NAGY, Ph.D., Babeş-Bolyai University, Cluj-Napoca, Romania

Professor Zoltan NEDA, Ph.D., Babeş-Bolyai University, Cluj-Napoca, Romania

Professor Jurgen POPP, Ph.D., Dr.h.c., Institute of Physical Chemistry, Friedrich-
Schiller-University Jena, Germany

Professor György SZABÓ, Ph.D., Research Institute for Technical Physics and
Materials Science, Hungarian Academy of Sciences, Budapest, Hungary

Professor Simion SIMON, Ph.D., Babeş-Bolyai University, Cluj-Napoca, Romania

Professor Romulus TETEAN, Ph.D., Babeş-Bolyai University, Cluj-Napoca, Romania

Professor Dietrich ZAHN, Ph.D., Dr.h.c., Technical University, Chemnitz, Germany

EXECUTIVE EDITOR:

Lecturer Claudiu LUNG, Ph.D., Babeş-Bolyai University, Cluj-Napoca, Romania

YEAR
MONTH
ISSUE

Volume 60 (LX) 2015
DECEMBER
2

STUDIA UNIVERSITATIS BABEȘ-BOLYAI PHYSICA

2

STUDIA UBB EDITORIAL OFFICE: B.P. Hasdeu no. 51, 400371 Cluj-Napoca, Romania,
Phone + 40 264 405352

CUPRINS – CONTENT – SOMMAIRE – INHALT

L. BIZO, K. MAGYARI, <i>Substitution of Couple Sn(IV)/Zn(II) For In(III) in the Fluorite-Like Transparent Conductors: $In_{5-2x}Sn_{1+x}SbZn_xO_{12}$</i>	5
M. BOSCA, V. POP, E. CULEA, I. VIDA-SIMITI, <i>Spectroscopic Properties of Cerium-Boro-Bismuthate Glasses</i>	13
M. BOSCA, E. CULEA, L. BOLUNDUT, P. PASCUTA, V. POP, N. TOTHAN, I. VIDA-SIMITI, <i>Role of Gd^{3+}: Ag Co-Doping on Structural and Optical Properties of Lead Tellurite Glass Ceramics</i>	25
IOAN COSMA, DIANA IOANA POPESCU, <i>Phenomenological Modeling of Sound Field Generated by Transversal Vibrations of Strait-Lined and Cylindrical Sources</i>	33
C. CRĂCIUN, <i>Uniformity Degree of Some Spherical Grids Used in Magnetic Resonance Powder Simulations</i>	43

R. HIRIAN, S. MICAN, B. NEAMȚU, V. POP, <i>Surfactant Effect on the Structural and Magnetic Properties of Fe Powders Prepared by Wet Milling</i>	53
A. M. JUNCAN, <i>Formulation and Optimizing of a Skin Barrier Regenerating Cosmeceutical Product</i>	59
LOREDANA F. LEOPOLD, CRISTINA COMAN, ISTVAN SZ. TODOR, LASZLO SZABO, OLGA SORIȚĂU, PIROSKA VIRAG, CARMEN M. MIHU, VLAD MOISOIU, NICOLAE LEOPOLD, <i>Raman Imaging of Dental Follicle Mesenchymal Stem Cells</i>	69
M. POP, D. FRUNZA, <i>Experimental and Finite Element Analysis Regarding the Influence of Friction Conditions on Material Flow in Metal Forming Processes</i>	77
R. A. POPESCU, K. MAGYARI, I. PAPUC, L. BAIA, SYNTHESIS, <i>Structural Characterization and in Vitro Evaluation of Bioactivity of Silver Containing Bioactive Glasses</i>	89

SUBSTITUTION OF COUPLE Sn(IV)/Zn(II) FOR In(III) IN THE FLUORITE-LIKE TRANSPARENT CONDUCTORS:



L. BIZO^{1*}, K. MAGYARI²

ABSTRACT. Three new compositions ($x = 0.1$, $x = 0.2$ and $x = 0.3$) belonging to $\text{In}_{5-2x}\text{Sn}_{1+x}\text{SbZn}_x\text{O}_{12}$ system, have been successfully synthesized by substitution of pair Sn(IV)/Zn(II) for In(III). The compositions were studied from point of view of structural, optical and electrical properties. Structure calculations shows an ordered cationic distribution over the octahedral and highly distorted sevenfold coordinated site. For $\text{In}_{4.4}\text{Sn}_{1.3}\text{SbZn}_{0.3}\text{O}_{12}$ composition a small amount of unreacted SnO_2 was identified, which decreases from 5.76 wt % to 3.17 wt %, by increasing preparation temperature from 1300 °C to 1350 °C. The electrical conductivity of the $x = 0.1$ composition was enhanced by approximately one order of magnitude with respect to $\text{In}_4\text{Sn}_3\text{O}_{12}$.

Keywords: *indium-based transparent conductors, oxygen-deficient fluorite-type structure, optical properties, electrical properties.*

INTRODUCTION

Due to the fact that a critical component in all flat panel displays (FPDs) are the electrodes which control the orientation of the liquid-crystal molecules, many effort are focuses on the discovery of new n- or p- type transparent conducting oxides (TCOs) [1]. TCOs oxide compositions space is dominated by following oxides and their combination: ZnO, In_2O_3 , Ga_2O_3 , SnO_2 and CdO. Besides the most famous ITO ($\text{In}_2\text{O}_3:\text{Sn}$), which combine highest transmissivity for visible light with the lowest electrical resistivity, another indium-rich oxide, with properties

¹ Babes-Bolyai University, Faculty of Chemistry and Chemical Engineering, 11 Arany Janos, RO-400028 Cluj-Napoca, Romania.

* Corresponding author e-mail: lbizo@chem.ubbcluj.ro

² Institute for Interdisciplinary Research on Bio-Nano-Sciences, Babeş-Bolyai University, Treboniu Laurian 42, RO-400271 Cluj-Napoca, Romania

close to ITO, was identified for the composition $\text{In}_4\text{Sn}_3\text{O}_{12}$. The structural studies of the later showed a rhombohedral unit cell which is viewed in a hexagonal basis, and is in fact a doubly ordered oxygen-deficient fluorite structure. Within the unit cell, there are two nonequivalent cationic sites, the six coordinate $3a$ position, a distorted cube with anion vacancies on a pair of opposite vertices, and a general $18f$ position, sevenfold coordinated with anions sets at the corners of a highly distorted cube with a vacancy at one vertex [2]. As previously shown, the $3a$ positions are exclusively occupied by the Sn cations, while the $18f$ positions are occupied by both Sn and In cations. Several transparent conductors have been previously reported [3-5], which shown that introduction of antimony revealed a great ability to form M_7O_{12} ordered oxygen-deficient fluorite structure [6]. Moreover, by the synthesis of $\text{In}_{4+x}\text{Sn}_{3-2x}\text{Sb}_x\text{O}_{12}$ solid solution, the electrical properties of $\text{In}_5\text{SnSbO}_{12}$ composition were improved by increasing the electronic conductivity up to one order of magnitude if compare to $\text{In}_4\text{Sn}_3\text{O}_{12}$. First-principles band-structure calculations performed on these compositions demonstrate strong similarities between the electronic structures of $\text{In}_4\text{Sn}_3\text{O}_{12}$ and $\text{In}_5\text{SnSbO}_{12}$ which suggest comparable physical properties in these materials [7, 8]. Consequently, the aim of this work is to investigate the possible substitution of the pair Sn(IV)/Zn(II) for In(III) in M_7O_{12} structure. $\text{In}_{5-2x}\text{Sn}_{1+x}\text{SbZn}_x\text{O}_{12}$ system was analysed from point of view of structural, optical and electrical properties.

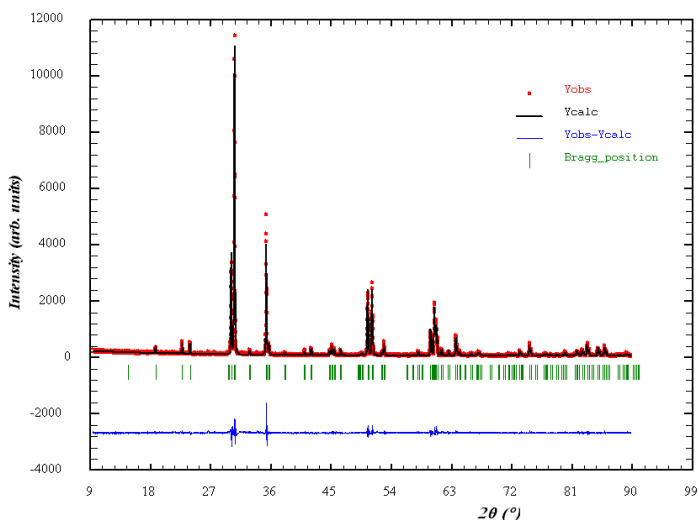
EXPERIMENTAL

Different compositions with the M_7O_{12} structure were prepared from mixtures of pure In_2O_3 , SnO_2 , Sb_2O_3 and ZnO , in alumina crucibles heated in air up to 1300 °C and 1350 °C, respectively. Crystalline phases were determined by X-ray diffractometry (XRD, Shimadzu 6000) using $\text{Cu-K}\alpha$ radiation ($\lambda = 1.5406 \text{ \AA}$) equipped with Ni-filter in a 2θ range of 5°-90°. The patterns were analyzed using Rietveld method (FullProf program [9]). The diffuse reflectance spectra of the as-prepared compositions were recorded with a double beam spectrophotometer (Cary Varian 100 Spectrofotometer) in the range 190-900 nm with a scan rate of 600 nm/min. The electrical resistivity of pellets sintered in air at 1350 °C was measured at room temperature by the four-probe method using a PPMS facility.

RESULTS AND DISCUSSION

XRPD structure calculation were performed in terms of a Rietveld analysis of the diffractograms, using the structural model of $\text{In}_4\text{Sn}_3\text{O}_{12}$, S.G. $\bar{R}\bar{3}$, with two

sets of cationic positions 3(a), 18(f) and three sets of oxygen positions 18(f), in the corresponding hexagonal cell. Results obtained from the Rietveld analysis of three compositions of the $\text{In}_{5-2x}\text{Sn}_{1+x}\text{SbZn}_x\text{O}_{12}$ system, corresponding to two different temperature, 1300 °C and 1350 °C, are reported in Table 1. For the different compositions analyzed, the convergence of the refinements was easily obtained, resulting in satisfying values of the reliability factors. For comparison, the data concerning $\text{In}_4\text{Sn}_3\text{O}_{12}$ ($x = 0$) and our previous results obtained from XRPD Rietveld analysis for $\text{In}_5\text{SnSbO}_{12}$ [6] are also reported. The calculated patterns fit with the experimental one, as exemplified for the $x = 0.1$ and $x = 0.3$ compositions (Fig.1). For $\text{In}_{4.4}\text{Sn}_{1.3}\text{SbZn}_{0.3}\text{O}_{12}$ composition a small amount of unreacted SnO_2 was identified. Consequently, for $x = 0.3$ composition it was decided to systematically include in the calculation procedure the possible extra phases SnO_2 . One can notice the presence of corresponding supplementary bars in Fig. 1b. In the retained example the calculated amount of the extra phases is equal to 5.76 wt% and 3.17 wt%, respectively. It should be emphasized that increasing temperature from 1300 °C to 1350 °C a decrease of secondary phase amount, was evidenced. Regarding the cationic distribution the 3(a) sites are preferentially occupied by antimony, whereas the additional Sb is statistically distributed in the 18(f) sites together with In and Zn. This cationic distribution is also supported by the tendency of Sb^{5+} to accommodate a highly symmetrical octahedral coordination, as previously demonstrated [10]. The smaller size of Sb^{5+} compared to In^{3+} , Sn^{4+} and Zn^{2+} , according to Shannon and Prewitt [11], are in agreement with this view point.



a)

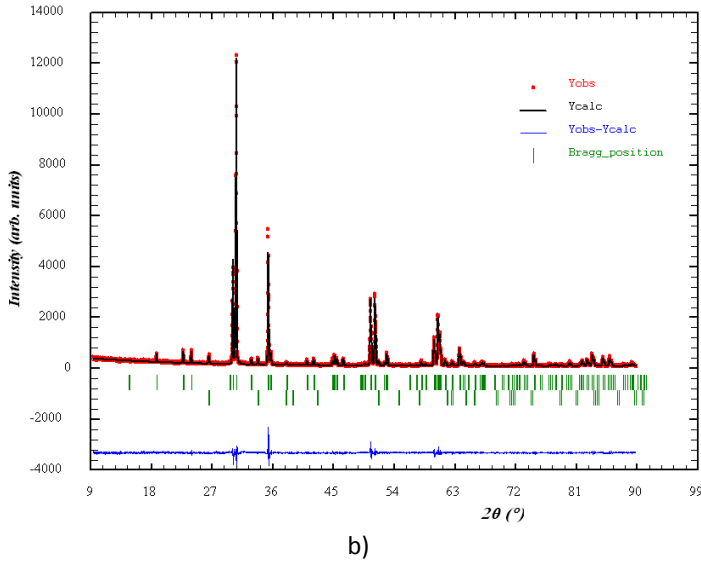


Fig. 1. Observed (dots), calculated (lines) and difference XRPD pattern of $x = 0.1$ (a) and $x = 0.3$ (b) composition, after heating at 1350 °C.

Table 1. Crystal chemical data for the compositions $x = 0.1$, $x = 0.2$ and $x = 0.3$ of the $\text{In}_{5-2x}\text{Sn}_{1+x}\text{SbZn}_x\text{O}_{12}$ system and compare to $\text{In}_5\text{SnSbO}_{12}$ [6].

Comp. x	Temperature (°C)	Cell parameters			Reliability factors		
		a (Å)	c (Å)	V (Å) ³	Rb	Rp	χ^2
$x = 0$ [6]	1400 °C	9.4478(2)	8.9034(2)	688.76	4.7	12.5	-
x = 0.1	1300 °C	9.443854	8.903104	687.655	4.21	11.9	2.725
	1350 °C	9.453803	8.911015	689.717	4.52	13.9	2.238
x = 0.2	1300 °C	9.44517	8.906440	688.184	3.96	12.5	2.828
	1350 °C	9.445716	8.907287	688.534	3.56	12.8	2.296
x = 0.3	1300 °C	9.439899	8.901480	686.954	3.38	12.1	2.129
	1350 °C	9.444859	8.904285	687.893	3.37	13.5	2.034

Figure 2 shows the diffuse reflectance (%R) spectra of $x = 0.1$, $x = 0.2$ and $x = 0.3$ compositions belonging to $\text{In}_{5-2x}\text{Sn}_{1+x}\text{SbZn}_x\text{O}_{12}$ system, prepared at 1350 °C. All samples exhibit a reflectance varied from 7-5% at wavelengths approximately 450 nm. The reflectance spectra of $\text{In}_{4.4}\text{Sn}_{1.3}\text{SbZn}_{0.3}\text{O}_{12}$, and $\text{In}_4\text{Sn}_3\text{O}_{12}$ and $\text{In}_5\text{SnSbO}_{12}$ for comparison, are displayed in Fig. 3. One indeed observes that introduction of tin and zinc in the presence of antimony, decreases

the maximum percent reflectance around 450 nm, by approximately 10%, with respect to $\text{In}_4\text{Sn}_3\text{O}_{12}$ and $\text{In}_5\text{SnSbO}_{12}$, respectively. Simultaneously, a small shift of the optical bandgap to higher energies, occurs.

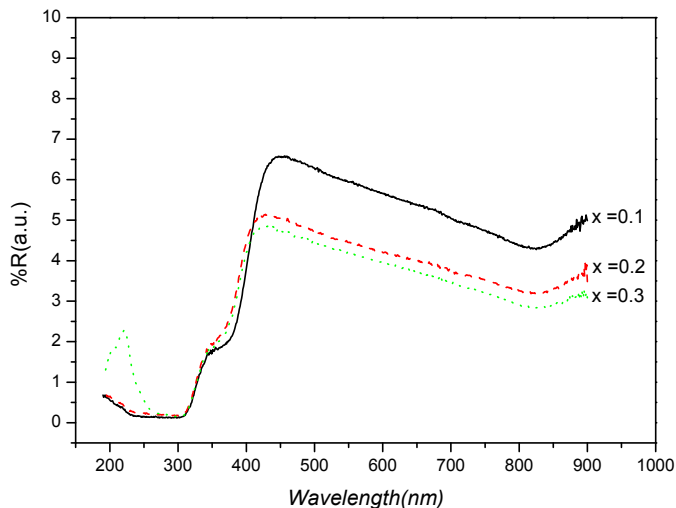


Fig. 2. Measured optical reflectance spectra in the compositions $x = 0.1$, $x = 0.2$ and $x = 0.3$ of the $\text{In}_{5-2x}\text{Sn}_{1+x}\text{SbZn}_x\text{O}_{12}$ system, after heating at 1350°C .

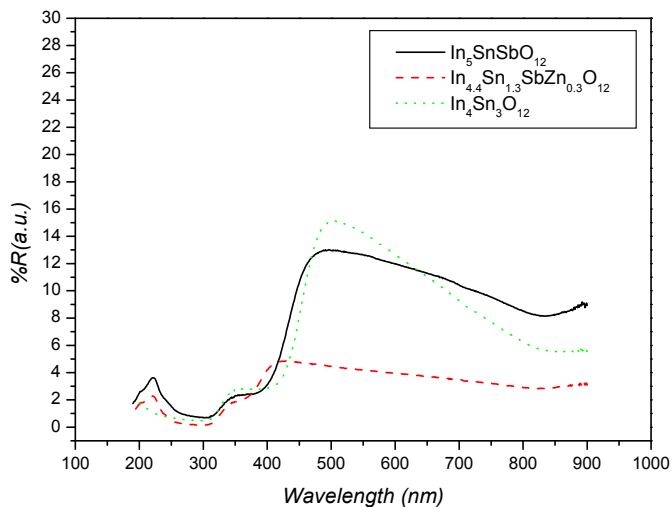


Fig. 3. Measured optical reflectance spectra in the compositions $x = 0$ ($\text{In}_5\text{SnSbO}_{12}$ treated at 1400°C), $x = 0.3$ (1350°C) and compared to $\text{In}_4\text{Sn}_3\text{O}_{12}$ (1400°C).

Electrical resistivity measurements were carried out by the four probe method at room temperature (RT) on pellets sintered at 1350 °C in air. For these experimental conditions, three samples corresponding to compositions $x = 0.1$, 0.2 and 0.3 were explored. For reference, two sample of $\text{In}_4\text{Sn}_3\text{O}_{12}$ and $\text{In}_5\text{SnSbO}_{12}$, sintered at 1400 °C, were also considered. The resistivity values (Table 2) show a decrease of the resistivity for $x = 0.1$ composition, by approximately one order of magnitude, if compare to $\text{In}_4\text{Sn}_3\text{O}_{12}$. For $x = 0.2$ and $x = 0.3$ compositions, introduction of couple Sn/Zn in the presence of Sb does not triggers increase of electrical resistivity, as shown in Table 2. These values are less than one magnitude order if compare with those reported for $\text{In}_4\text{Sn}_3\text{O}_{12}$ by several authors [2, 12, 13]. Thus, the resistivity of the new oxide $\text{In}_{4.4}\text{Sn}_{1.3}\text{SbZn}_{0.1}\text{O}_{12}$ is approximately one order of magnitude smaller than that of $\text{In}_4\text{Sn}_3\text{O}_{12}$ and less than one order of magnitude larger than that of $\text{In}_5\text{SnSbO}_{12}$.

Table 2. Room temperature electrical resistivity values measured for $x = 0.1$, $x = 0.2$ and $x = 0.3$ compositions belonging to $\text{In}_{5-2x}\text{Sn}_{1+x}\text{SbZn}_x\text{O}_{12}$ system (1350 °C), and compared to $\text{In}_5\text{SnSbO}_{12}$ and $\text{In}_4\text{Sn}_3\text{O}_{12}$ (1400 °C).

Composition	$x = 0$ [6]	$x = 0.1$	$x = 0.2$	$x = 0.3$	$\text{In}_4\text{Sn}_3\text{O}_{12}$ [2,12,13]
ρ_{RT} ($\Omega\cdot\text{cm}$)	2.8×10^{-3}	5×10^{-3}	9×10^{-2}	6×10^{-2}	$2 - 2.6 \times 10^{-2}$

CONCLUSIONS

The compositions $x = 0.1$, $x = 0.2$ and $x = 0.3$, belonging to $\text{In}_{5-2x}\text{Sn}_{1+x}\text{SbZn}_x\text{O}_{12}$ system, have been successfully synthesized by solid state reaction in air. Structure calculations performed by Rietveld analysis of the X-ray powder diffraction (XRPD) data revealed a ordered cationic distribution over the two cationic sites. For $\text{In}_{4.4}\text{Sn}_{1.3}\text{SbZn}_{0.3}\text{O}_{12}$ composition a small amount of unreacted SnO_2 was identified. By increasing temperature from 1300 °C to 1350 °C, a decrease of secondary phase amount, from 5.76 wt% to 3.17 wt%, was evidenced. The optical spectra show their potential as transparent conductor. The electrical conductivity of the $x = 0.1$ composition was enhanced by approximately one order of magnitude with respect to $\text{In}_4\text{Sn}_3\text{O}_{12}$.

REFERENCES

1. D. S. Ginley, H. Hosono, and D. C. Paine, "Handbook of Transparent Conductors", Springer, Berlin, 2010, DOI: 10.1007/978-1-4419-1637-2.
2. N. Nadaud, N. Lequeux, M. Nanot, *J. Solid State Chem.*, 135, 140 (1998).
3. L. Bizo, *Studia UBB Physica*, Vol. 59 (LIX), 2, 69 (2014).

4. L. Bizo, *Studia UBB Physica*, Vol. 57(LVII), 1, 15 (2012).
5. L. Bizo, C. I. Anghel, *Rev. Roum. Chim.*, 57(4-5), 369 (2012).
6. J. Choynet, L. Bizo, R. Retoux, S. Hebert, B. Raveau, *J. Solid State Chem.*, 177 (10), 3748 (2004).
7. C. Y. Ren, S. H. Chiou, and J. Choynet, *J. Appl. Phys.*, 99, 023706 (2006).
8. D. H. O'Neil, A. Walsh, R. M. J. Jacobs, V. L. Kuznetsov, R. G. Egdell, P. P. Edwards, *Physical Review B*, 81, 085110 (2010).
9. J. Rodriguez-Carvajal, T. Roisnel, "Line Broadening Analysis Using FullProf: Determination of Microstructural Properties", in: European Powder Diffraction Conference (EPDIC) 8, 2004, Vol. 443, pp 123–126.
10. J. Choynet, P. Mouron, *Mater. Res. Bull.*, 22, 1355 (1989).
11. R. D. Shannon, C. T. Prewitt, *Acta Cryst.*, 25B, 925 (1969).
12. J. L. Bates, C. W. Griffin, D. D. Marchant, J. E. Garnier, *Am. Ceram. Soc. Bull.*, 65, 673 (1986).
13. W. Pitschke, J. Werner, G. Behr, K. Koumoto, *J. Solid State Chem.*, 153, 349 (2000).

SPECTROSCOPIC PROPERTIES OF CERIUM-BORO-BISMUTHATE GLASSES

M. BOSCA^{1*}, V. POP, E. CULEA, I. VIDA-SIMITI

ABSTRACT. X-Ray diffraction (XRD), density measurements, Fourier transform infrared (FTIR), diffuse reflectance ultraviolet–visible (DR-UV-Vis) and photoluminescence (PL) spectroscopies were performed on the glasses in the $x\text{CeO}_2 \cdot (100-x)[4\text{Bi}_2\text{O}_3 \cdot \text{B}_2\text{O}_3]$ system, with $0 \leq x \leq 15$ mol%, in order to point out the effect of CeO_2 addition to the boro-bismuthate host glass matrix on the local structure, optical and luminescent properties. The XRD patterns confirm a long-range structural disorder characteristic of amorphous network. FT-IR spectroscopy reveals absorption bands which are characteristic of BiO_3 , BiO_6 , BO_3 and BO_4 structural units. The optical band gap values for the studied glasses were calculated from the DR-UV-Vis spectra. The peaks evidenced by PL spectroscopy measurements are due to the presence of bismuth, in different valence states, in the studied glasses. Luminescence data show that the peaks intensity decrease over a content of 5 mol% CeO_2 , this concentration representing the critical value over which the luminescence quenching becomes important.

Keywords: Boro-bismuthate glasses; Cerium ions; XRD; FTIR; Optical and luminescent properties.

INTRODUCTION

In recent technological world, glass materials doped with rare earth (RE) ions play an important role due to their multiple applications such as optical data transmission, detection, and information processes, undersea cameras, data storage, display technology, sensing (gas sensors, temperature sensors, etc.), laser technologies, producing low temperatures via magnetic cooling, etc. [1, 2]. Also, because a greater part of rare earths ions have an incomplete 4f level and can exhibit electronically forbidden f–f spectra in the ultraviolet, visible or infrared

¹ Technical University of Cluj-Napoca, 103-105 Muncii Avenue, 400641 Cluj-Napoca, Romania

* Corresponding author e-mail: Maria.Cleja@phys.utcluj.ro

region, the optical properties of the glasses doped with this kind of rare earths ions are very important.

Cerium dioxide (CeO_2) containing compounds have been used in various applications such as catalysts, solar cells, oxygen sensors, fuel cells, UV blocks, and polishing materials [3-5], likewise this oxide of cerium has useful properties such as hardness, greater stability at high temperatures, high absorption capacity of UV radiation and good optical and magnetic properties [4, 6]. Due to these interesting properties glasses doped with cerium oxide are also promising materials for optical and emitting devices [7-9].

On the other hand, glasses containing heavy metals like bismuth, are very important because can exhibit near-infrared luminescence, high density, high optical properties, high polarizability [10-12] and for these reasons have multiple applications such as optical amplifiers, optical fibers, electronic devices, thermal and mechanical sensors, reflecting windows, etc. Bismuth trioxide is not known like a glass former but in the presence of B_2O_3 , P_2O_5 , SiO_2 , can become a glass network former because the Bi^{3+} ions are highly polarizable and therefore bismuth atom can exhibit various valence state. The glass networks containing bismuth ions can consist of BiO_6 octahedral and BiO_3 pyramidal units [13-15].

The boron trioxide is one of the classical glass formers. According to the literature [16-19] the structure of glasses containing boron trioxide consists of multiple boroxol rings and BO_3 and BO_4 units linked together by B-O-B bridges. This kind of glasses present also a great variety of applications being used as dielectrics and insulating materials. Their thermoluminescent properties are of a great interest, too [20].

Due to all these reasons, in this paper was considered the $4\text{Bi}_2\text{O}_3\cdot\text{B}_2\text{O}_3$ glass matrix to be a very interesting host for the cerium ions. The aim of this work was to investigate and establish the structural changes induced by the cerium oxide addition and to study the optical, structural and luminescent properties of this kind of glasses.

EXPERIMENTAL

Reagent grade purity Bi_2O_3 , H_3BO_3 and CeO_2 were taken in suitable proportions to prepare the glasses from the $x\text{CeO}_2\cdot(100-x)[4\text{Bi}_2\text{O}_3\cdot\text{B}_2\text{O}_3]$ system. The required amounts of mentioned oxides were milled in an agate ball mill to obtain a fine powder. The obtained mixtures were melted for 20 minutes, using sintered corundum crucibles in an electric furnace at 1200°C . The crucibles were placed into the electric furnace directly at this temperature. The glass samples were obtained by pouring the molten material onto a stainless-steel plate.

The XRD measurements of fine powdered sample were performed with a Shimadzu 6000 XRD diffractometer, in the 2θ range of $10 - 60^\circ$ at a scan rate of 2°

per minute. The diffraction patterns were recorded at the room temperature using Cu-K α radiation with the source power of 40 kV and 30 mA.

The density of samples was determined at room temperature using Archimede's method with distillate water as immersion liquid. The molar volume was calculated from the obtained density using the $V_m = M/\rho$ relation, where M is the molar mass of the sample and ρ is the density of the sample.

The FT-IR absorption spectra of the investigated glasses were registered at room temperature in the 400 - 1500 cm⁻¹ range using a JASCO FT-IR 6200 spectrometer. The studied samples were mixed with KBr in a ratio of 2:300 glass powder: KBr, respectively.

The DR-UV-Vis spectra were recorded with a PerkinElmer Lambda 45 UV-Vis spectrometer equipped with an integrating sphere, at room temperature. The studied samples were measured in MgO pellets. DR-UV-Vis spectra of the investigated glasses were recorded in reflectance units and were transformed in Kubelka-Munk remission function F(R).

The photoluminescence (PL) spectra were registered at room temperature with a Jasco FP-8200 spectrofluorometer using a Xe lamp as excitation source. In order to obtain powders with similar dimensions the obtained glasses have been crushed and sieved. The excitation wavelength was 380 nm.

RESULTS AND DISCUSSION

XRD data

The amorphous nature of the prepared samples was examined using the XRD technique. The XRD patterns recorded for the investigated samples are shown in Fig. 1.

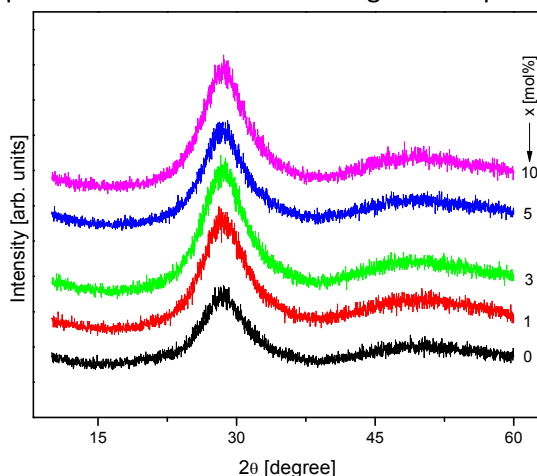


Fig. 1. XRD patterns of $x\text{CeO}_2 \cdot (100-x)[4\text{Bi}_2\text{O}_3 \cdot \text{B}_2\text{O}_3]$ glasses

The XRD patterns exhibit two broad diffuse scattering instead of crystalline peaks. The absence of sharp Bragg peaks in the XRD patterns confirms a long-range structural disorder characteristic of amorphous network. For all studied glasses the angular position for first amorphous halo is at about 28.60° . From the first halo maximum position it can be calculated the average distance between the atoms in the first coordination sphere by using the relation $R = (5 \lambda) / (8 \sin \theta)$ [21]. For all investigated samples this distance was found to be about 3.89 \AA .

Density and molar volume data

Fig. 2 presents the density (ρ) and molar volume (V_m) variations with increasing of CeO_2 content for the $x\text{CeO}_2 \cdot (100-x)[4\text{Bi}_2\text{O}_3 \cdot \text{B}_2\text{O}_3]$ glass system.

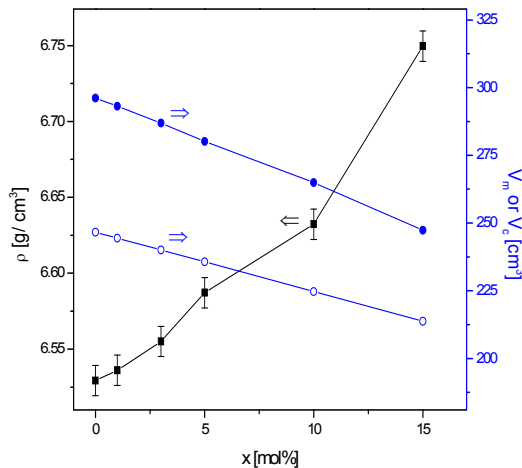


Fig. 2. Composition dependence of crystalline (o) and glassy (●) molar volume and of density (■) of $x\text{CeO}_2 \cdot (100-x)[4\text{Bi}_2\text{O}_3 \cdot \text{B}_2\text{O}_3]$ system

This figure shows that the density increases with increasing of CeO_2 content suggesting that the glass network becomes more compact. Fig. 2 shows also the calculated sums of the theoretical molar volumes (V_c) of the component oxides for the studied glasses considered in their crystalline states. The molar volume of the studied $x\text{CeO}_2 \cdot (100-x)[4\text{Bi}_2\text{O}_3 \cdot \text{B}_2\text{O}_3]$ glasses is always greater than that of their hypothetical crystalline oxide mixtures, indicating the presence of an excess structural volume in the glasses. On the other hand, the increase of cerium oxide content leads to a decrease of both the molar volume and the difference between V_m and V_c . These results show a better packing of coordination polyhedra in the structural network of boro-bismuthate glasses once with increasing of cerium ions content.

FTIR data

Fig. 3 shows the FTIR absorption spectra of the studied boro-bismuthate glasses doped with CeO_2 .

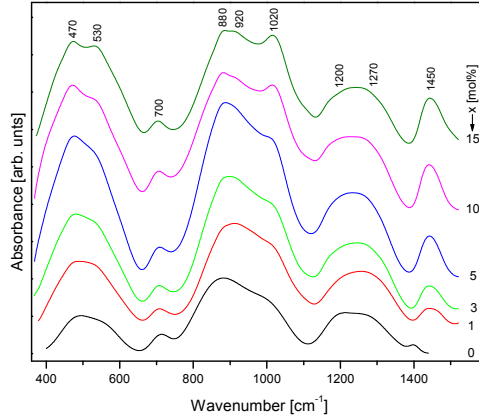


Fig. 3. FTIR spectra of $x\text{CeO}_2 \cdot (100-x)[4\text{Bi}_2\text{O}_3 \cdot \text{B}_2\text{O}_3]$ glasses

It can be observed the presence of three broad bands in the $400\text{-}650\text{ cm}^{-1}$, $650\text{-}1100\text{ cm}^{-1}$ and $1100\text{-}1500\text{ cm}^{-1}$ spectral regions, respectively. These broad bands are the result of the overlapping of several individual bands. Each individual band gives information about the type of vibration and the concentration of a specific structural group. A deconvolution process was performed to extract the band centers, C , and its relative area, A , for each individual band. Fig. 4 presents the deconvoluted spectrum, in Gaussian bands, of the glass containing 15 mol% CeO_2 , as representative example. Table 1 summarizes the bands assignment for the studied glasses.

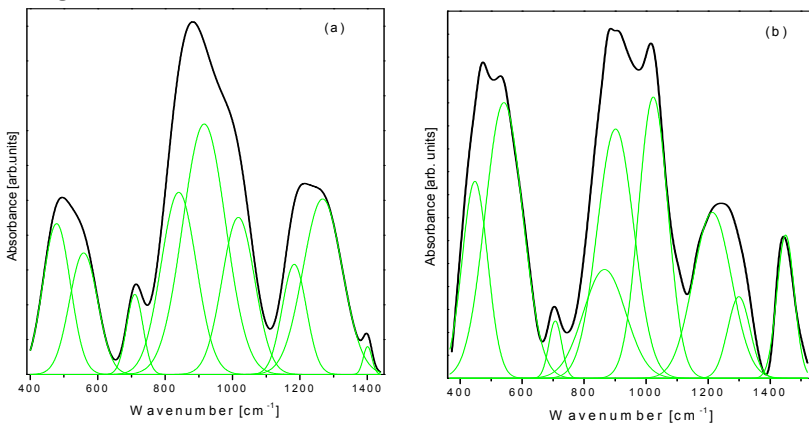


Fig. 4. Deconvoluted FTIR spectra of $x\text{CeO}_2 \cdot (100-x)[4\text{Bi}_2\text{O}_3 \cdot \text{B}_2\text{O}_3]$ glasses using a Gaussian type function for $x = 0\text{ mol}\%$ (a) and $x = 15\text{ mol}\%$ (b)

In the first spectral region, 400 - 650 cm^{-1} , the result of absorption band deconvolution indicates a number of 2 peaks. For the host glass matrix these bands are centered at ~ 478 and $\sim 558 \text{ cm}^{-1}$. These bands were ascribed to the Bi-O bending vibration in BiO_3 units (the absorption band from $\sim 478 \text{ cm}^{-1}$) and respectively in BiO_6 units (the band from $\sim 558 \text{ cm}^{-1}$) [22-25]. As result of the appearance of cerium ions in the glass matrix, the intensity of these bands increase having a maximum for the glasses containing 5 mol% CeO_2 for the band from $\sim 478 \text{ cm}^{-1}$ and 10 mol% CeO_2 for the band from $\sim 558 \text{ cm}^{-1}$. For higher CeO_2 contents the intensity of these bands decreases and shifts to lower wavenumbers, at ~ 447 and $\sim 541 \text{ cm}^{-1}$, respectively.

In the second spectral region, 650 -1100 cm^{-1} , after deconvolution, the following bands located at ~ 710 , ~ 840 , ~ 916 and $\sim 1017 \text{ cm}^{-1}$ were obtained. The band from $\sim 710 \text{ cm}^{-1}$ was assigned to the bending vibrations of B-O-B linkage in the borate network [26-30]. The existence of this band was assumed to point out that at least some super-structural borate units are retained in the structure of boro-bismuthate glasses [12]. The amplitude of this band is approximately the same for all the compositional range.

Table 1. Assignment of the IR bands for the $x\text{CeO}_2 \cdot (100-x)[4\text{Bi}_2\text{O}_3 \cdot \text{B}_2\text{O}_3]$ glasses

Wavenumber [cm^{-1}]	Assignments
454-478	Bi-O bend in BiO_3 units
541-558	Bi-O bend in BiO_6 units
706-710	B-O-B bend
840-859	Bi-O _{sym} stretch in BiO_3 units Bi-O vibration in distorted BiO_6 units
900-918	B-O stretch in BO_4 units from di-borate groups
1009-1026	B-O stretch in BO_4 units from tri-, tetra- and penta-borate groups
1183-1215	B-O _{asym} stretch in BO_3 units from pyro- and ortho-borate groups
1267-1297	B-O stretch in BO_3 units from boroxol rings
1400-1449	B-O ⁻ stretch in BO_3 units from varied types of borate groups

The absorption band at $\sim 840 \text{ cm}^{-1}$ was assigned to the Bi-O symmetrical stretching vibration in BiO_3 units [22]. When the CeO_2 content increases to 15 mol%, this band shifts to higher wavenumbers, around 865 cm^{-1} . This latter band was ascribed to vibrations of strongly distorted BiO_6 octahedral units [22-25]. The compositional evolution of this band suggests a conversion of the BiO_3 into BiO_6 units with the increase of the cerium ions content. Thus, the presence of cerium ions influences the surrounding of the Bi^{3+} cations favoring the formation of BiO_6 units. The absorption bands from ~ 916 and $\sim 1017 \text{ cm}^{-1}$ indicate the presence of the BO_4 structural units in the studied glasses [19]. Thus, the absorption feature from $\sim 916 \text{ cm}^{-1}$ can be due to the B-O stretching vibrations in BO_4 units from di-borate groups, while the band from $\sim 1017 \text{ cm}^{-1}$ was assigned to the B-O stretching vibrations in BO_4 units from tri-, tetra- and penta-borate groups [26-30].

In the third IR spectral region, from 1100 to 1500 cm^{-1} , three bands were obtained centered at ~ 1183 , ~ 1267 and ~ 1400 cm^{-1} . This spectral region originates from the stretching vibration and asymmetric stretching vibrations of B-O and B-O $^-$ bonds respectively, in borate triangular units, which are of the BO_3 and BO_2O^- type [19]. The band at ~ 1183 cm^{-1} was assigned to asymmetric stretching vibrations of B-O $^-$ in BO_3 units from pyro- and ortho-borate [19]. Pyro- and ortho-borate groups contain a large number of non-bridging oxygen. The peak at around 1267 cm^{-1} can be due to stretching vibration of B-O in boroxol rings [26-30]. The band situated at around 1400 cm^{-1} is due to stretching vibrations of B-O $^-$ in BO_3 units from various types of borate groups [26-30].

It is well known that the addition of a modifier oxide, such as CeO_2 , can cause changes in the relative population of BO_3 and BO_4 structural units. The fraction of four-coordinated boron atoms, N_4 , can be used to trace these changes with increasing the cerium ions content. The deconvolution technique can be used to obtain the N_4 values, because the concentration of the structural units is proportional to the relative area of its component band. N_4 is the ratio of the number of BO_4 units (the relative areas of component bands from 900-918, 1009-1026 cm^{-1}) to the number of BO_4 units plus the number of BO_3 units (the relative areas of component bands from 1183-1215, 1267-1299, 1400-1449 cm^{-1}) [24, 25, 31, 32].

For the studied glasses the dependence of N_4 on CeO_2 content is shown in Fig. 5. The obtained value of N_4 for the host glass matrix is 0.634. For glasses doped with CeO_2 the values of N_4 decrease from 0.632 to 0.461 when the content of CeO_2 increases from 1 to 15 mol%. For glasses with $x \leq 10$ mol% the four-coordinated boron atoms are favored in the investigated glass system in comparison with the three-coordinated ones. For higher CeO_2 contents the three-coordinated boron atoms became favored.

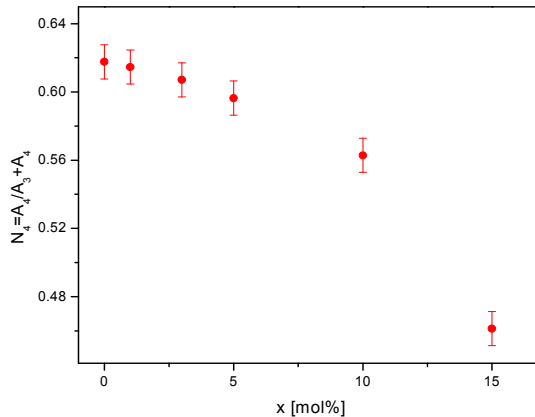


Fig. 5. The composition dependence of N_4 for the studied glasses

The structural changes observed in the network structure at the short-range order level by increasing the cerium ions content in the host glass matrix evidenced from FT-IR data suggest that the cerium ions play the role of vitreous network modifier in the investigated glasses.

DR-UV-Vis data

DR-UV-Vis spectra of the $x\text{CeO}_2 \cdot (100-x)[4\text{Bi}_2\text{O}_3 \cdot \text{B}_2\text{O}_3]$ glasses were recorded at room temperature in reflectance units and were transformed in Kubelka–Munk remission function $F(R)$. The DR-UV-Vis spectra obtained for the studied glasses (after Kubelka–Munk transformation) are shown in Fig. 6a. From this figure it can be observed that our glasses exhibits no obvious absorption peaks in the 350-1000 nm wavelength range being in agreement with previously reported data [33]. The optical band gap energy, E_g , was calculated for all the studied samples by plotting $[F(R) \cdot hu]^2$ as a function of hu , since $F(R)$ is considered proportional to the radiation absorption (h is the Planck constant). Then, the E_g values were estimated by extrapolation of the linear region of the mentioned plots (see Fig. 6b).

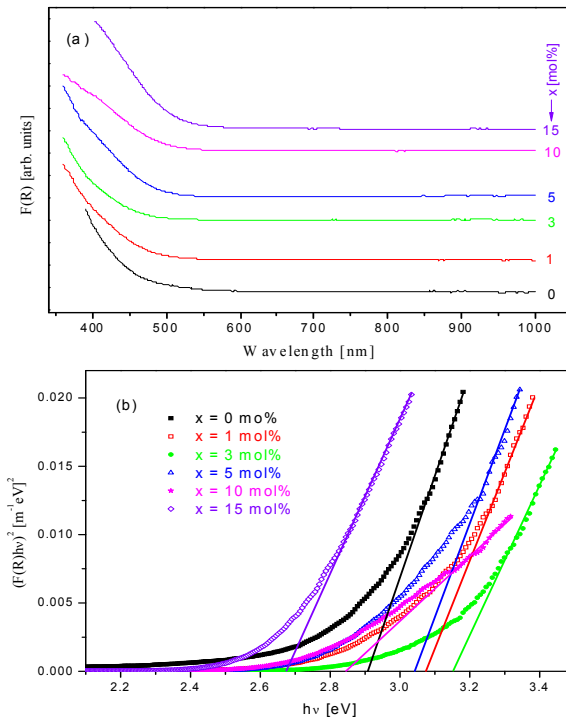


Fig. 6. DR-UV-Vis spectra of $x\text{CeO}_2 \cdot (100-x)[4\text{Bi}_2\text{O}_3 \cdot \text{B}_2\text{O}_3]$ glasses (a). Variation of $(F(R) \cdot hu)^2$ versus hu for the studied glass samples (b).

Fig. 7 shows the composition dependence of E_g obtained for the studied glasses. The value of the optical band gap energy for the host glass matrix is 2.91 eV. For the glasses doped with cerium ions, we note the increase of the E_g values up to 3 mol% CeO_2 . After that the E_g values decrease with increasing of CeO_2 content. The decrease of the optical band gap energy is due to the increase of the amount of non-bridging oxygen atoms from the glass network that occurs with increasing the cerium oxide content of the samples [34]. In the same time, as results from our FTIR data, the BO_4 tetrahedral borate units are converted in BO_3 trigonal units. This process generates an excess of oxygen that will determine the oxidation of cerium ions, $\text{Ce}^{3+} \rightarrow \text{Ce}^{4+}$, and the cerium ions are forced to have the maximum number of coordinated oxygen (eight). Such an assumption offers a reasonable explanation, as will be shown, that luminescent spectra do not exhibit significant luminescence peaks assignable to cerium.

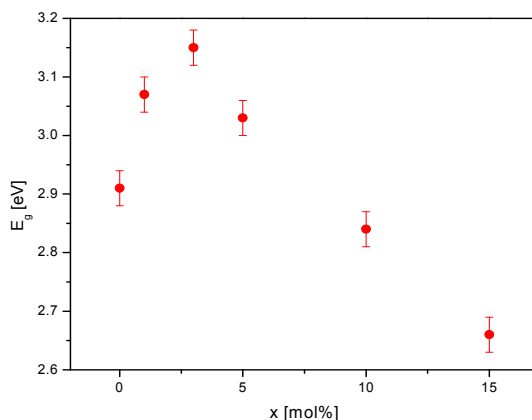


Fig. 7. Variation of E_g versus CeO_2 content for the $x\text{CeO}_2 \cdot (100-x)[4\text{Bi}_2\text{O}_3 \cdot \text{B}_2\text{O}_3]$ glasses

Finally, note that DR-UV-Vis data of the $x\text{CeO}_2 \cdot (100-x)[4\text{Bi}_2\text{O}_3 \cdot \text{B}_2\text{O}_3]$ glasses suggest that their glass network becomes more compact with increasing the cerium oxide content of the samples. This result supports the compositional evolution of density for the studied glasses.

Luminescence data

The luminescence spectra of the $x\text{CeO}_2 \cdot (100-x)[4\text{Bi}_2\text{O}_3 \cdot \text{B}_2\text{O}_3]$ glasses were recorded using an excitation wavelength of 380 nm. These spectra are presented in Fig. 8. The analysis of these spectra shows the presence of three emission bands (400 nm, 438 nm and 700 nm) that appear in all the samples, including the cerium

free sample. This observation suggests that the luminescent peaks may be assigned to the presence of bismuth ions, in different valence states, in all studied samples.

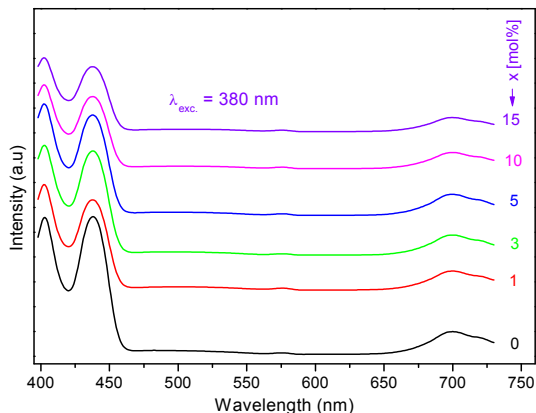


Fig. 8. Luminescence spectra of $x\text{CeO}_2 \cdot (100-x)[4\text{Bi}_2\text{O}_3 \cdot \text{B}_2\text{O}_3]$ glasses

The peaks around 400 nm and 438 nm were attributed to the Bi^{3+} ions, and are probably due to the $^3\text{P}_1 \rightarrow ^1\text{S}_0$ transition and a $\pi^* \rightarrow \pi$ or $n \rightarrow \pi^*$ intraligand transition in polymetallate groups (BiO_3). This assumption is in agreement with literature data [35, 36]. The other peak, located around 700 nm, is due to presence of Bi^0 atoms in the studied samples [37]. Such atoms may appear in the glass network since the relatively high melting temperature (1200°C) produces a thermal dissociation of Bi_2O_3 into elementary Bi.

Note that previous reports [7-9, 34] mentioned that in the 400-500 nm region and around 660 nm luminescence peaks appear due to the presence of Ce^{3+} ions. Note also that the Ce^{4+} ions do not show any luminescence response from 4f orbital which do not contain any electron [38]. The luminescent peaks of Ce^{3+} ions are due to the transitions from the 5d levels to the $^2\text{F}_{5/2}$ and $^2\text{F}_{7/2}$ ground state levels [7-9] and their number strongly depends on the Ce^{3+} ions environment [34]. In our luminescent spectra, these peaks overlap the peaks coming from the bismuth ions. The addition of cerium oxide produces changes of the luminescent peaks intensity but do not affect their position. The luminescent peaks intensity decreases by adding cerium oxide. Since this process becomes very intense over the 5 mol% cerium oxide content this value represents probably the one for which the luminescence quenching occurs.

CONCLUSIONS

Glasses from the $x\text{CeO}_2 \cdot (100-x)[4\text{Bi}_2\text{O}_3 \cdot \text{B}_2\text{O}_3]$ system with $0 < x < 15$ mol% were obtained by using the melt-quenching technique. XRD confirms the amorphous

nature of the studied samples. FT-IR spectra and the compositional variation of V_m and V_c reveal that CeO_2 acts as a structural network modifier and both Bi_2O_3 and B_2O_3 play the role of network formers. The FT-IR data show that the network structure of studied glasses consists of BiO_3 , BiO_6 , BO_3 and BO_4 units. The UV-Vis spectra show no absorption peaks in the 350-1000 nm wavelength range. The calculated optical band gap energy was observed to decrease for cerium oxide contents higher than 3 mol% suggesting that the glass network becomes more compact. These data are in agreement with density measurements. The luminescence data show that the peaks intensity decreases over a 5 mol% content of CeO_2 where the luminescence quenching becomes important.

ACKNOWLEDGMENT

This paper was supported by the Post-Doctoral Programme POSDRU/159/1.5/S/137516, project co-funded from European Social Fund through the Human Resources Sectorial Operational Program 2007-2013.

REFERENCE

1. B. Sun, H. Song, J. Wang, H. Peng, X. Zhang, S. Lu, J. Zhang and H. Xia, *Chem. Phys. Lett.*, 368, 412 (2003).
2. V. Venkatramu, P. Babu and C.K. Jayasankar, *Spectrochim. Acta A*, 63, 276 (2006).
3. X.D. Feng, D.C. Sayle, Z.L. Wang, M.S. Paras, B. Santora, A.C. Sutorik, T.X.T. Sayle, Y. Yang, Y. Ding, X.D. Wang and Y.S. Her, *Science*, 312, 1504 (2006).
4. A. Trovarelli, C. de Leitenburg, M. Boaro and G. Dolcetti, *Catal. Today*, 50, 353 (1999).
5. S.P. Singh, R.P.S. Chakradhar, J.L. Rao and B. Karmakar, *J. Alloys Compd.*, 493, 256 (2010).
6. E. Culea, L. Pop and M. Bosca, *J. Alloys Compd.*, 505, 754 (2010).
7. M. Rodriguez Chialanza, A. Cardenas, E. Castiglioni, J. Castiglioni, J.F. Carvalho and L. Fornaro, *J. Non-Cryst. Solids*, 401, 181 (2015).
8. P. Kaur, S. Kaur, G. P. Singh and D.P. Singh, *J. Alloy Compd.*, 588, 394 (2014).
9. Li-Hua Zheng, Xin-Yuan Sun, Ri-Hua Mao, Hao-Hong Chen, Zhi-Jun Zhang and Jing-Tai Zhao, *J. Non-Cryst. Solids*, 403, 1 (2014).
10. S. Hazra, S. Mandal and A. Ghosh, *Phys. Rev. B*, 56, 8021 (2005).
11. M. Nocun, W. Mozgawa, J. Jedlinski and J. Najman, *J. Mol. Structure*, 744-747, 603 (2014).
12. F.H. ElBatal, S.Y. Marzouk, N. Nada and S.M. Desouky, *Physics B*, 391, 88 (2007).
13. S. Hazra and A. Ghosh, *Phys. Rev. B*, 51, 851 (1995).
14. L. Baia, R. Stefan, J. Popp, S. Simon and W. Kiefer, *J. Non-Cryst. Solids*, 324, 109 (2003).
15. E. Culea, *J. Non-Cryst. Solids*, 357, 50 (2011).

16. D.L. Griscon, "Materials Science Research, Borate Glasses", Plenum, New York, **1978**, pag. 36.
17. J. Krogh-Moe, *Phys. Chem. Glasses*, **3**, 101 (1962).
18. R.L. Mozzi and B.E. Waren, *J. Appl. Crystallogr.*, **3**, 251 (1970).
19. Y.D. Yiannopoulos, G.D. Chryssikos and E.I. Kamitsos, *Phys. Chem. Glasses*, **42**, 164 (2001).
20. A.N. Yazici, M. Dogan, V.E. Kafadar and H. Toktamis, *Nucl. Instrum. Meth. Phys. Res. B*, **246**, 402 (2006).
21. H.P. Klug and L.E. Alexander, "X-Ray Diffraction Procedures", Wiley, New York, **1970**, p. 632.
22. Y. Hu, N.H. Liu and U.L. Lin, *J. Mater. Sci.*, **33**, 229 (1998).
23. R. Iordanova, V. Dimitriev, Y. Dimitriev and D. Klissurski, *J. Non-Cryst. Solids*, **180**, 58 (1994).
24. P. Pascuta, G. Borodi and E. Culea, *J. Non. Cryst. Solids*, **354**, 5475 (2008).
25. P. Pascuta, G. Borodi and E. Culea, *J. Mater. Sci.: Mater. Electron.*, **20**, 360 (2011).
26. E.I. Kamitsos, M.A. Karakassides and G.D. Chyssikos, *J. Phys. Chem.*, **91**, 1073 (1987).
27. M. Abo-Naf, F. H. ElBatal and M.A. Azooz, *Mater. Chem. Phys.*, **77**, 846 (2002).
28. A. Kumar, S.B. Rai and D.K. Rai, *Mater. Res. Bull.*, **38**, 333 (2003).
29. P. Pascuta and E. Culea, *Mater. Lett.*, **62**, 417 (2008).
30. P. Pascuta, *J. Mater. Sci.: Mater. Electron.*, **21**, 338 (2010).
31. K. El-Egili, *Physica B*, **325**, 340 (2003).
32. P. Pascuta, L. Pop, S. Rada, M. Bosca and E. Culea, *J. Mater. Sci.: Mater. Electron.*, **19**, 424 (2008).
33. Y.Q. Qiu, J. Kang, C.X. Li, X.Y. Dong and C.L. Zhao, *Laser Physics*, **20**, 487 (2010).
34. P. Kaur, G. P. Singh, S. Kaur and D.P. Singh, *J. Mol. Structure*, **1020**, 83 (2012).
35. K. Polak and E. Mihokova, *Opt. Mater.*, **32**, 1280 (2010).
36. M. Feyand, M. Koppen, G. Friedrichs and N. Stock, *Chem. Eur. J.*, **19**, 12537 (2013).
37. M. Peng, C. Zollfrank and L. Wondraczek, *J. Phys.: Condens. Matter*, **21**, 285106 (2009).
38. G. K. Das Mohapatra, *Phys. Chem. Glasses*, **39**, 50 (1998).

ROLE OF Gd^{3+} : Ag CO-DOPING ON STRUCTURAL AND OPTICAL PROPERTIES OF LEAD TELLURITE GLASS CERAMICS

M. BOSCA^{1*}, E. CULEA, L. BOLUNDUT, P. PASCUTA, V. POP,
N. TOTHAN, I. VIDA-SIMITI

ABSTRACT. Fourier transform infrared (FTIR) and diffuse reflectance ultraviolet-visible (DR-UV-VIS) spectroscopies were used to investigate the lead tellurite glass ceramics doped with different contents of Gd^{3+} ions and co-doped with fixed amounts of Ag_2O or metallic Ag nanoparticles (AgNPs). FTIR spectral studies have been made to put in evidence the presence of basic structural units in the studied glass ceramics samples. The obtained FTIR spectra reveal vibrational IR bands which are attributed to the presence of TeO_3 , TeO_4 , PbO_3 and PbO_4 structural units in the glass ceramics network. DR-UV-VIS spectra were used to calculate the optical band gap energy (E_g). The obtained E_g values depend on the Gd^{3+} ions content and the nature of the dopant (Ag_2O or AgNPs) present in the studied glass ceramics samples.

Keywords: Lead tellurite glass ceramics; Gd^{3+} ions; Silver oxide; Silver nanoparticles; FTIR; DR-UV-VIS.

INTRODUCTION

Glasses and glass ceramics containing rare-earth (RE) ions attracted much attention in the last years due to their important properties promising for technological applications [1-8]. Thus, studies of these materials draw important potential applications in areas such as solid state lasers, optical fiber amplifiers, optical data storage, sensors, infrared to visible convertors, solar concentrators, phosphors, electro-luminescent devices, display monitor etc. [4, 9-13]. In this view, a considerable interest was accorded to glasses and glass ceramics doped with gadolinium ions [14-18]. The optical and magnetic properties of glasses and glass ceramics containing gadolinium ions are determined by the content and distribution of Gd^{3+} ions in the host matrix as well as by the local environment of gadolinium ions.

¹ Technical University of Cluj-Napoca, 103-105 Muncii Avenue, 400641 Cluj-Napoca, Romania.

* Corresponding author e-mail: Maria.Cleja@phys.utcluj.ro

On the other hand, the properties of glasses and glass ceramics doped with RE ions and co-doped with silver ions or AgNPs are intensively studied because of their interesting optical and luminescent properties that make them suitable for important technological applications in electronics and telecommunication [2, 6, 12, 19-22].

In order to extend the available information concerning lead tellurite glasses and glass ceramics doped with Gd^{3+} ions and co-doped with silver ions or AgNPs, in this paper we present the experimental data obtained by studying such materials by using FTIR and DR-UV-VIS spectroscopies. The aim of this study was to observe the influence of the Gd_2O_3 doping level and of the co-dopant nature (Ag_2O or AgNPs) on the structural and optical properties of the studied samples.

EXPERIMENTAL

Reagents, grade pure Gd_2O_3 , TeO_2 , PbO , Ag_2O and metallic Ag nanoparticles (AgNPs) (particles size of 20-40 nm) were used to obtain samples with the chemical compositions listed in table 1. Required quantities of reagents were mixed together, in stoichiometric amounts, by grinding in an agate mortar to obtain homogeneous mixtures. The obtained mixtures were melted in porcelain crucibles using an electric furnace at $850\text{ }^\circ\text{C}$ for 15 minutes. The melts were quickly cooled to room temperature by pressing between two stainless steel plates. X-ray diffraction data shows that the samples from both studied series were glass ceramics.

The FTIR absorption spectra were recorded at room temperature with a JASCO FTIR 6200 spectrophotometer. All the samples were measured using the KBr pellet technique where 2 mg powder of each sample is mixed with 300 mg of KBr in an agate mortar for obtaining a homogeneous mixture.

DR-UV-VIS spectra were registered at room temperature using a PerkinElmer Lambda 45 UV-VIS spectrometer equipped with an integrating sphere. The obtained samples were measured in MgO pellets.

Table 1. Chemical composition for the studied glass ceramics

Sample no.	(mol%)			
	80TeO ₂ :20PbO	Ag ₂ O	AgNPs	Gd ₂ O ₃
S0	100	-	-	-
S1	99.50	0.50	-	-
S1'	99.70	-	0.30	-
S2	98.50	0.50	-	1
S2'	98.70	-	0.30	1
S3	96.50	0.50	-	3
S3'	96.70	-	0.30	3

S4	94.50	0.50	-	5
S4'	94.70	-	0.30	5
S5	89.50	0.50	-	10
S5'	89.70	-	0.30	10

RESULTS AND DISCUSSION

FTIR data

FTIR spectroscopy is an experimental technique that was used to investigate the local structure of lead tellurite glass ceramics doped with gadolinium ions and co-doped with fixed amounts of silver (Ag₂O or AgNPs). FTIR absorption spectra of studied samples are shown in figure 1. A deconvolution of the experimental FTIR bands was necessary since the majority of these bands are very broad consisting of a superposition of several individual absorption bands where the individual bands are due to vibrations characteristic of the basic structural units from the studied samples. As a representative example, figure 2 illustrates the deconvolution in Gaussian bands for the FTIR spectra of the samples S2 (figure 2a) and S5' (figure 2b). The obtained individual bands were assigned based on data available in the literature [23-28] and are given in table 2.

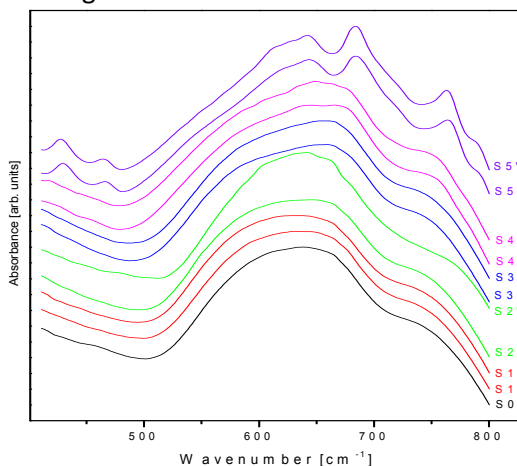


Fig. 1. FTIR spectra of the studied glass ceramics samples

The FTIR data show the presence of PbO₃, PbO₄, TeO₃ and TeO₄ structural units in the studied lead tellurite glass ceramics network. In order to analyze the effect, of increasing the gadolinium ions content and the influence of co-dopants' nature (Ag₂O or AgNPs) on the local structure of studied glass ceramics samples, we have calculated the relative integrated intensity $A_r = A_3 / A_4$, where A_3 and A_4 approximate the relative number of TeO₃ and TeO₄ units.

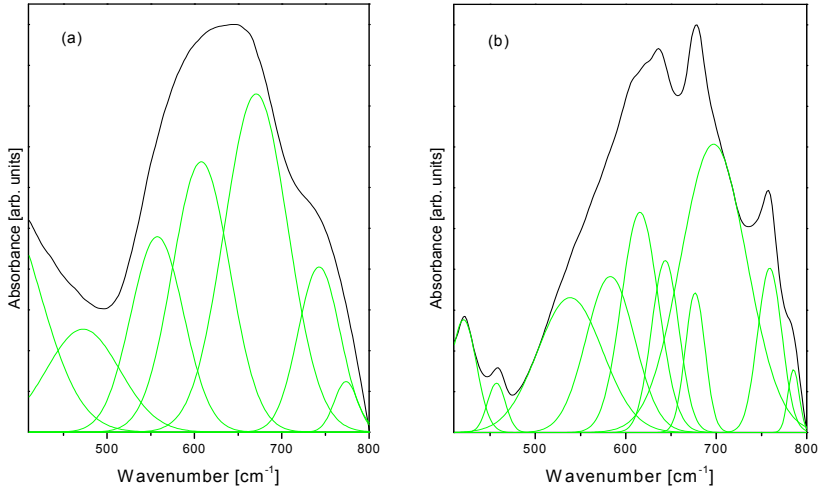


Fig. 2. Deconvoluted FTIR spectra of the samples S2 (a) and S5' (b)

The compositional evolution of A_r for the both series of studied glass ceramics samples (co-doped with Ag_2O or AgNPs) are presented in figure 3. For both series of studied samples, A_r decreases with increasing the gadolinium ions content over the whole compositional range. This evolution can be explained by the progressive conversion of TeO_3 into TeO_4 structural units with increasing the Gd_2O_3 content. This assumption is well supported by the fact that increasing the Gd_2O_3 content of samples generates the increase of their degree of crystallinity and that in crystalline compounds tellurium ions are present mainly in their 4+ valence state. For glass ceramics co-doped with AgNPs the values of A_r are slightly higher than for the samples co-doped with Ag_2O . This suggests that not only the doping level with gadolinium ions but also the nature of the co-dopant (Ag_2O or AgNPs) plays an important role determining the local structure of these samples.

Table 2. Assignment of the IR bands for the studied glass ceramics

Wavenumber [cm^{-1}]	Assignment
362-488	Te-O-Te or O-Te-O bending vibration [23-26] Pb-O stretching vibrations in PbO_4 units [23-26]
537-561	Pb-O symmetrical bending vibration [23, 25] Ag-O bonds vibration [23]
583-617	Te-O stretching vibration in TeO_4 units [24, 26, 27]
644-698	Te-O bonds vibration in TeO_4 units [23, 24, 28] Pb-O vibration in PbO_n pyramidal units ($n = 3$ and/or 4) [23, 24, 28]
742-759	Te-O bonds vibration in TeO_3 units [26]
773-786	Te-O ⁻ bonds vibration in TeO_3 units [26]

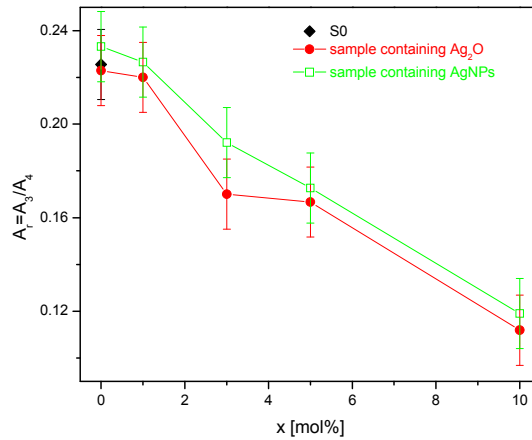


Fig. 3. The A_r ratio as a function of the Gd_2O_3 content for the studied glass ceramics samples

Optical gap energy

Optical band gap energy is an important property of glasses and glass ceramics which can reveal the structural modifications that can occur due to the compositional variation of the studied glass ceramics. In order to determine the optical band gap energy for the studied glass ceramics samples UV-VIS diffuse reflectance measurements were carried out. Generally the Kubelka–Munk remission function, $F(R)$, is used to convert the diffuse reflectance into the equivalent absorption coefficient because this function can be considered proportional to the radiation absorption [29]. The optical band gap energy is determined using the plot of $[F(R) \cdot hu]^2$ as a function of hu . The E_g values were estimated by extrapolation of the linear region of the mentioned plots (see figure 4).

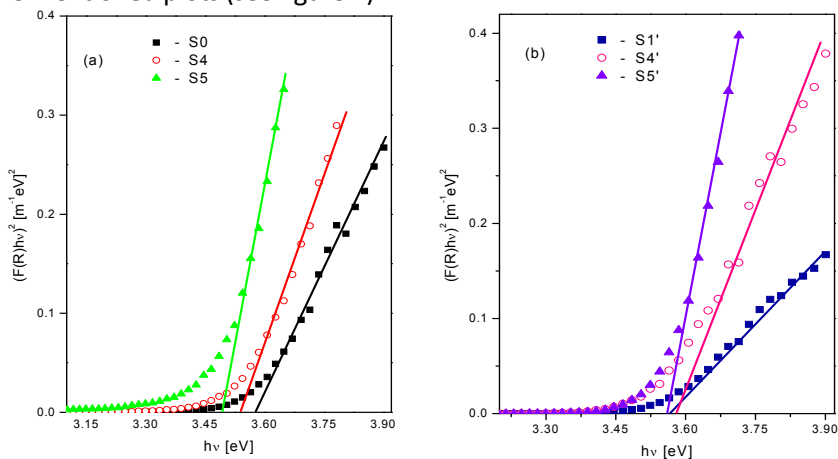


Fig. 4. Variation of $(F(R) \cdot hu)^2$ vs. hu for some samples containing Ag_2O (a) and AgNPs (b)

Figure 5 shows the variation of optical band gap energy with the content of Gd_2O_3 for both series of studied glass ceramics. For the host glass ceramic matrix ($80TeO_2\cdot 20PbO$) the value of E_g is 3.578 eV. The addition of Ag_2O (S1) or AgNPs (S1') to the host glass ceramic lead to a slow decrease of E_g . For samples doped with Gd_2O_3 and co-doped with Ag_2O , the optical band gap energy first increases up to 3 mol% Gd_2O_3 and after that decreases for a further increase of the gadolinium ions content. A similar behavior was observed for the samples co-doped with AgNPs, but in this case the values of E_g increase up to 1 mol% Gd_2O_3 and decrease for higher Gd_2O_3 contents.

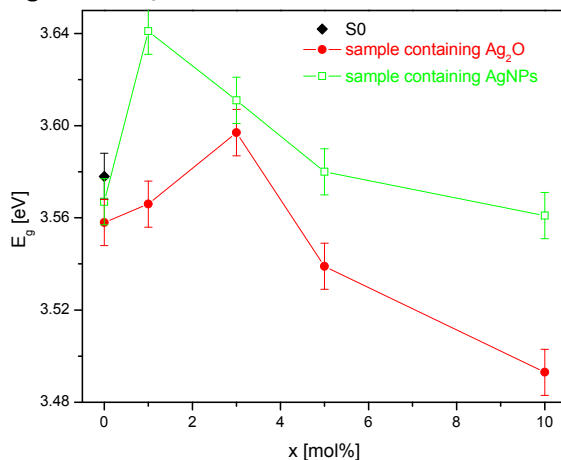


Fig. 5. The evolution of E_g versus Gd_2O_3 content for the studied samples

The decrease of the E_g values with increasing the Gd_2O_3 content for both series of the studied samples can be due to the structural changes that are taking place in these samples. These structural changes are accompanied by a decrease of the average bond energy due probably to the forming of non-bridging oxygen's.

CONCLUSIONS

FTIR data of studied glass ceramics suggest that the local structure of the studied lead-tellurite samples is modified with the addition and increase of Gd_2O_3 content. Thus, FTIR data show a conversion of TeO_3 into TeO_4 structural units with increasing the Gd^{3+} ions content for both series of studied samples. In this process, the nature of co-dopant is also important, the amount of TeO_3 structural units being higher for samples co-doped with AgNPs in comparison with those co-doped with Ag_2O .

The optical band gap energy, E_g , is affected not only by the increasing gadolinium ions content in the studied glass ceramics but also by the nature of co-dopant (Ag₂O or AgNPs). A decrease of E_g is observed for both kinds of samples. This process is related to a decrease of the average bond energy due to the formation of non-bridging oxygen's in the samples.

ACKNOWLEDGMENT

This paper was supported by the Post-Doctoral Programme POSDRU/159/1.5/S/137516, project co-funded from European Social Fund through the Human Resources Sectorial Operational Program 2007-2013.

REFERENCE

1. M. Venkateswarlu, M.V.V.K.S. Prasad, K. Swapna, Sk. Mahamuda, A. Srinivasa Rao, A. Mohan Babu, D. Haranath, *Ceram. Int.*, 40, 6261 (2014).
2. E. Culea, I. Vida-Simiti, G. Borodi, E. N. Culea, R. Stefan, P. Pascuta, *J. Mater. Sci.*, 49, 4620 (2014).
3. A. Lu, X. Hu, Y. Lei, Z. Luo, X. Li, *Ceram. Int.*, 40, 11 (2014).
4. M. Reza Dousti, Raja J. Amjad, *J. Non-Cryst. Solids*, 420, 21 (2015).
5. G. Anjaiah, SK. Nayab Rasool, P. Kistaiah, *J. Lumin.*, 159, 110 (2015).
6. L. Bolundut, E. Culea, G. Borodi, R. Stefan, C. Munteanu, P. Pascuta, *Ceram. Int.*, 41, 2931 (2015).
7. A. Dwivedi, C. Joshi, S.B. Rai, *Opt. Mater.*, 45, 202 (2015).
8. S. Arunkumar, K. Marimuthu, *J. Alloy Compd.*, 627, 54 (2015).
9. W.S. Souza, R.O. Domingues, L.A. Bueno, E.B. da Costa, A.S. Gouveia-Neto, *J. Lumin.*, 144, 87 (2013).
10. R.L. Leonard, S.K. Gray, S.D. Albritton, L.N. Brothers, R.M. Cross, A.N. Eastes, H.Y. Hah, H.S. James, J.E. King, S.R. Mishra, J.A. Johnson, *J. Non-Cryst. Solids*, 366, 1 (2013).
11. J. Suresh Kumar, K. Pavani, M.P.F. Graça, M.J. Soares, *J. Alloy Compd.*, 617, 108 (2014).
12. E. N. Culea, P. Pascuta, M. Pustan, D. R. Tamas-Gavrea, L. Pop, I. Vida-Simiti, *J. Non-Cryst. Solids*, 408, 18 (2015).
13. Hyun-A Park, Yi Kwon Lee, Won Bin Im, Jong Heo, Woon Jin Chung, *Opt. Mater.*, 41, 67 (2015).
14. S. Rada, M. Culea, M. Rada, P. Pascuta, V. Maties, E. Culea, *J. Mol. Struct.*, 937, 70 (2009).
15. Y. B. Saddeek, I.S. Yahia, K.A. Aly, W. Dobrowolski, *Solid State Sci.*, 12, 1426 (2010).
16. P. Pascuta, *J. Mater. Sci.: Mater. Electron.*, 21, 338 (2010).
17. N. Elkhoshkhany, Rafik Abbas, R. El-Mallawany, A.J. Fraih, *Ceram Int.*, 40, 14477 (2014).

18. H. Luo, X. Hu, W. Liu, Y. Zhang, A. Lu, X. Hao, *J. Non-Cryst. Solids*, 389, 86 (2014).
19. Z. Ashur S. Mahraz, M.R. Sahar, S.K. Ghoshal, M.R. Dousti, R.J. Amjad, *Mater. Lett.*, 112, 136 (2013).
20. E. Culea, I. Vida-Simiti, G. Borodi, E. N. Culea, R. Stefan, P. Pascuta, *Ceram. Int.*, 40, 11001 (2014).
21. R. J. Amjad, M.R. Dousti, M.R. Sahar, S.F. Shaukat, S.K. Ghoshal, E.S. Sazali, Fakhra Nawaz, *J. Lumin.*, 154, 316 (2014).
22. M. Reza Dousti, R.J. Amjad, R. Hosseinian S., M. Salehi, M.R. Sahar, *J. Lumin.*, 159, 100 (2015).
23. M. Bosca, L. Pop, G. Borodi, P. Pascuta, E. Culea, *J. Alloy Compd.*, 479, 579 (2009).
24. S. Rada, A. Dehelean, E. Culea, *J. Non. Cryst. Solids*, 357, 3070 (2011).
25. E. Culea, *J. Non-Cryst. Solids*, 357, 50 (2011).
26. E. Monsour, *J. Mol. Struct.*, 1014, 1 (2012).
27. E. A. Mohamed, F. Ahmad, K. A. Aly, *J. Alloy Compd.*, 538, 230 (2012).
28. M. Çelikbilek, A.E. Ersundu, S. Aydın, *J. Non-Cryst. Solids*, 378, 247 (2013).
29. G. Theophil Anand, L. John Kennedy, J. Judith Vijaya, *J. Alloy Compd.*, 581, 558 (2013).

PHENOMENOLOGICAL MODELING OF SOUND FIELD GENERATED BY TRANSVERSAL VIBRATIONS OF STRAIT-LINED AND CYLINDRICAL SOURCES

IOAN COSMA^{1*}, DIANA IOANA POPESCU²

ABSTRACT. The paper presents two physical models meant to calculate the characteristics of noise fields produced by real strait-lined sources. Our study highlights the complexity of phenomenological and mathematical correlations between the parameters that should depict the field of traveling waves generated by real cylindrical surfaces. Acoustically, the distribution of sound flows is modeled through beady vibrating string or cylindrical-tube sources. Our results, in conjunction with sound level sonometric measurements, permit many comparative analysis of effective perturbation in sound propagation. Together with point or spherical models, our results can be implemented in the training of future specialists in applied acoustics of environmental ecology.

Keywords: *Strait-lined and cylindrical sources, noise level distribution modeling*

1. INTRODUCTION

The vibrating systems become sources of simpler or more complex sounds, depending on how the normal modes are excited, more or less relevantly. These facts are most obvious on the vibrating strings, plates, blades and tubes. Through pulsed collision, their walls transmit momentum to the molecular layer of ambient air and so compressional waves that travel by successive compressions and relaxations are generated. Physiologically, these ondulatory or wave movements, also called sounds, are perceptible by the sense of hearing. Waves behaviors are determined by the inertial and elastic properties of air, through the density ρ , and the parameter γp_0

¹ Technical University, Memorandum Str. 28, 401248 Cluj-Napoca, Romania

* Corresponding author e-mail: icosma@phys.utcluj.ro, Diana.Popescu@mep.utcluj.ro,

² Technical University, Memorandum Str. 28, 401248 Cluj-Napoca, Romania

(γ - adiabatic exponent, p_0 -atmospheric pressure). Each mode of oscillation, from the set of possible modes of vibrating sources, acts as a simple oscillator in a forced sustained oscillation. These sources transmit a part of their energy to the air and thus the system will be maintained stationary. As the emission of successive wave fronts is normal, they will also have a geometric shape similar to the radiating surface.

Due to restoring forces in a local environment, disturbances occur and they spread almost as mechanical waves. This mechanism and progressive form of vibratory motion can be described by traveling oscillatory displacements and changes of local pressure. Acoustically, in real cases, the noise field should be taken as those generated by stationary incoherent, extended sources, or by judicious distributed sources [1, 2, 3]. For calculation the spatial distribution of noise intensity, one has to define the principles which justify the connection with the energetic-stochastic character of the real composition of the sound field generated by the equivalent sources. So, our models relate to the study of noise levels produced at the receptors placed in different points of sound field.

2. MODELING OF SOUND FIELDS GENERATED BY STRAIT-LINED SOURCES

Dynamically, the amounts of pressure and intensity of sound wave will characterize, in time and in space, this very widespread and complex form of undulatory motion of matter. Considering the field of restoring forces as a conservative one, the rate of energy exchanges into and out of a given region of the fluid will be equal. The spreading mechanism of the deformation and movement is specified by the instant, local mater density and intensity of the wave's energy. The relationship between them shows that waves carry mechanical vibratory energy through elastic medium without an effective drift-movement of the mater, or that all waves, mechanical and of other nature, have a macroscopic traveling-progressive character.

All possible vibration modes of the tubular sources will be assimilated to a breathing mode in which the cylinder wall radius expands and contracts. All parts are moving at the same rate. This type of vibrators, called monopole, radiates sound equally [4, 5] well in all directions. The sound pressure radiated by a monopole source varies with angle, but pressure is the same for all radial angles. This moving shows the motion of the cylinder as well as the resulting motion of the particles in the fluid surrounding the circle cylinder. Each particle oscillates back and forth about some equilibrium radius. Thus, the phase of their relative motions produces an outward traveling spherical wave. In a non-dispersive medium the wave-fronts (points of constant phase) are circles and the maximum particle displacement

(amplitude) is the same at any point on a wave-front. According to superposition principle, the study of incoherent waves emitted by real sound radiators implicates the use the energetic scalar amounts. Thus, in each considered volume of the sound field, the integral energy of the complex wave will result as a sum of all specific energies of each component mode of complex generative vibration.

Considering the sound intensity as the rate of wave's energy passing through the unit of oriented area S , around a point on the wave front [6, 7, 8], the local density of wave energy, related to sound intensity, will respect the equations:

$$\varepsilon = \frac{\delta E}{\delta V} = \frac{W\delta t}{Sv\delta t} = \frac{W}{Sv} = \frac{I}{v} \Rightarrow \vec{I} = \frac{W}{\vec{S}} = \varepsilon \vec{v} \quad (1)$$

where W is the power of sound flow. Trough wave front speed, v , we can see the vectorial character of the wave intensity I . Based on the above considerations we developed two models for strait-linear noise sources.

2.1. Model of rectilinear beady sources

To develop the model for calculating the intensity of noise produced by

rectilinear source, we consider that this is equivalent with a strait-lined string system consisting of punctual or spherical adjacent beady sources, emitting each omni-directionally. In figure 1, one can follow all the considerations for finding the sound intensity in the observation point P located at the distance r from the axis Ox of the rectilinear source.

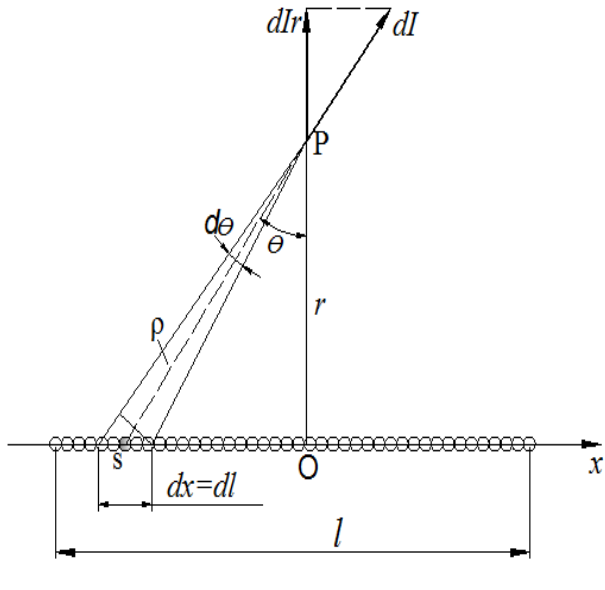


Fig. 1. Linear beady sound source

Considering the infinitesimal length $dl=dx$ of vibrating rectilinear beady sources, the linear density of emission being

$w = dW/dl$, as in the case of a point or spherical source, its contribution to the intensity of the sound field at the point P, will be:

$$dI = \frac{w dl}{4\pi\rho^2},$$

Consistently, the radial intensity projection normally to the sources direction is:

$$dI_r = \frac{w dx}{4\pi\rho^2} \cos\theta$$

Noting that we have the distances $\rho=r/\cos\vartheta$ and $dl=dx=\rho d\vartheta/\cos\vartheta$ and then substituting, we obtain the radial contribution to the intensity of the punctual source S, of coordinate $x=OS$.

Considering a sufficiently long rectilinear beady string sources (comparatively with the observation distance) the angle ϑ takes values ranging from $-\pi/2$ to $+\pi/2$. Thus, the full amount of contributions to the intensity will be:

$$I_r = \int_{-\frac{\pi}{2}}^{+\frac{\pi}{2}} \frac{w \cos\theta}{4\pi r} d\theta = \frac{w \sin\theta}{4\pi r} \Big|_{-\frac{\pi}{2}}^{+\frac{\pi}{2}} = \frac{w}{4\pi r} (1+1) = \frac{w}{2\pi r} \quad (2)$$

So, the received noises inverse-proportionally decrease with the distance to strait-lined source. For a real flow consisting of noise sources having diverse emission powers and forms, the linear density of the emission can be considered as the statistical average for each particular $w=w(r)$ distribution.

2. 2. The model of tubular sound source (Hollow cylinder sound source model).

We present a phenomenological model of tubular sound sources that explain more intuitive the emission (radiation) of the sound. This is based on the normal transfer of momentum and mechanical energy from the wall transversal vibration of hollow-cylinder to the air which becomes the porter of progressive compressional (longitudinal) sound waves.

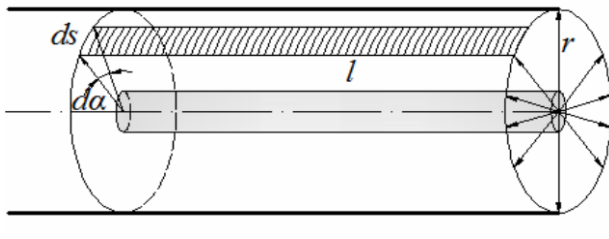


Fig. 2. Hollow cylinder sound source

For finding the spatial distribution of intensity in the fields generated by strait-lined sources, we will take into account that a cylindrical-tubular source radiates wave

field with a radial symmetry in two dimensions. The transverse vibrations of the hollow-cylinder walls act upon air strata generating radial oscillatory forces and thereby compressional wave fronts will propagate in the form of coaxial cylindrical layers.

In figure 2 one can see that the infinitesimal area of a thin strip included between two generatrix of the cylindrical wave front will be $dS=lds=lr d\alpha$, where l is the length, $ds=r d\alpha$ the strip width and $d\alpha$ is the plan angle under which is seen the arc ds located at distance r from the axis of the tubular source. Under these conditions, the area through which the sound emitted flows will be:

$$S = \int_0^{2\pi} l r d\alpha = 2\pi r l$$

So, in a point of the sound field generated by the cylindrical source with radial emission power W , the noise intensity will be:

$$I(r) = \frac{E}{t S} = \frac{W}{2\pi r l} = \frac{w l}{2\pi r l} = \frac{w}{2\pi r} \quad (2')$$

where $w=W/l$ is the power output per unit length of the source. The physical limitation $r \geq r_0$ is required, i.e. the distances to observer have to be equal or greater than the radius r_0 of the hollow-cylindrical source.

It is noted that these two modeling, by pearly spherical string and respectively hollow-cylindrical sources, lead to the same sound intensity expressions (2) and (2'). This may indicate that the stationary vibrations of these sources generate a sound field with cylindrical symmetry, which topographically has a wave-form of coaxial cylindrical layers.

Because the sound intensity decreases inverse proportionally with the distance from the axial source and between two cylindrical coaxial surfaces of rays r_1 and r_2 the radial waves system carries the same energy per unit time, we have:

$$\frac{I_1}{I_2} = \frac{r_2}{r_1} \quad \text{and the pressure} \quad \frac{p_1}{p_2} = \sqrt{\frac{I_1}{I_2}} = \sqrt{\frac{r_2}{r_1}}$$

As the sound pressure is proportional to the oscillation amplitude and to the speed of these movements, it is evident that the elongation of the two-dimensional waves decreases inverse proportionally to the square root of the distance. So, with $r^2=x^2+y^2$, it is assumed that the kinematics equation of the undulatory sinusoidal movement will be:

$$\Psi(r, t) = \frac{A(0)}{\sqrt{r}} \sin \tilde{\omega}(t - \frac{r}{v}) \quad (3)$$

This function can be considered a consistent solution of the wave's differential equation in two-dimensions:

$$\frac{\partial^2 \Psi}{\partial t^2} = \frac{v^2}{r^2} \frac{\partial}{\partial r} r^2 \frac{\partial \Psi}{\partial r}$$

Thus, the modeling of the sound intensity generated by linear beady or tubular cylinder sources is confirming through cylindrical symmetry of elongations $\Psi(r, t)$ of 2D radial scattering.

Some sources of sound such as e.g. the vibrating string of musical instruments can be, mathematically, approximated by a (circular) cylindrical source of infinite extent, which facilitates an analytical solution. [9, 10].

3. LEVEL OF NOISE GENERATED BY THE STRAIT-LINED SOURCES

The loudness of psychophysical normal audible sensations, including other noxious effects, increases logarithmically with the increasing of physical stimuli intensity. For characterize auditory sensation, it is unanimous accepted to use so called noise level that is the logarithm of relative intensity of sounds. It is a dimensionless quantity that measures, less subjectively, the energy action effect of the stimulus upon sensory organs that, psychologically, is reflected through the loudness of sensation [11, 12].

Using equations (2) the sound level at the distance r from a linear-beady or hollow-cylindrical source, having the emission power per unit length w , will be:

$$L(r) = 10 \log \frac{I(r)}{I_{ref}} = 10 \log \frac{w}{2\pi r I_{ref}} = 10 \log \frac{w}{10^{-12}} - 10 \log r - 10 \log 2\pi \Rightarrow \quad (4)$$

$$L = L_w - 10 \log r - 8$$

The dimensional homogeneity of these equations is ensured if: $w_{ref}=10^{-12}$ W/m and $r_{ref}=1m$. $L_w=120 \log w$ is the level of sound power per length unit of source with cylindrical symmetric emission.

Usually, the sound loudness or listening intensity in a point is evaluated by the level of sound pressure. Since $I=p^2/\rho v$ with $I_{ref}=10^{-12}$ W·m⁻² and reference pressure $p_{ref}=2 \cdot 10^{-5}$ Pa, between the sound level referred to pressure and to intensity in a given point of the sound field, under normal conditions of air, there is a difference of less than one decibel, witch usually, is neglected. Indeed:

$$10 \log \left(\frac{p^2(r)}{p_{ref}^2} \frac{I_{ref}}{I(r)} \right) = 10 \log \left(\frac{\rho v I_{ref}}{p_{ref}^2} \right) = 10 \log \frac{1.28 \cdot 331 \cdot 10^{-12}}{4 \cdot 10^{-10}} = 0.25 \text{ dB} \quad (5)$$

According to equations (5), through divergent cylindrical symmetry scattering, the level of the noise generated by strait-lined sources decreases linearly with the logarithm of the distance to axis source, slower than those with spherical scattering, which decreases with $\log r^2$.

In reality, due to absorption, the amplitude of progressive wave is exponentially attenuated with distance. For the waves with cylindrical symmetry, the amplitude is given by the equation:

$$A(r) = \frac{A(0)}{\sqrt{r}} e^{-\chi r}$$

where $A(0)= A(r=R)$ is the amplitude of sound waves excited in the air at the surface of the hollow-cylindrical source. The amplitude attenuation coefficient χ is one half of the intensity absorption coefficient ($\alpha=2\chi$) noise level in air will be:

$$L(r) = L_w - 10\alpha|r| - 10\log|r| - 8 = L_{w_0} - 10(\chi r + \log r) - 8 \quad (6)$$

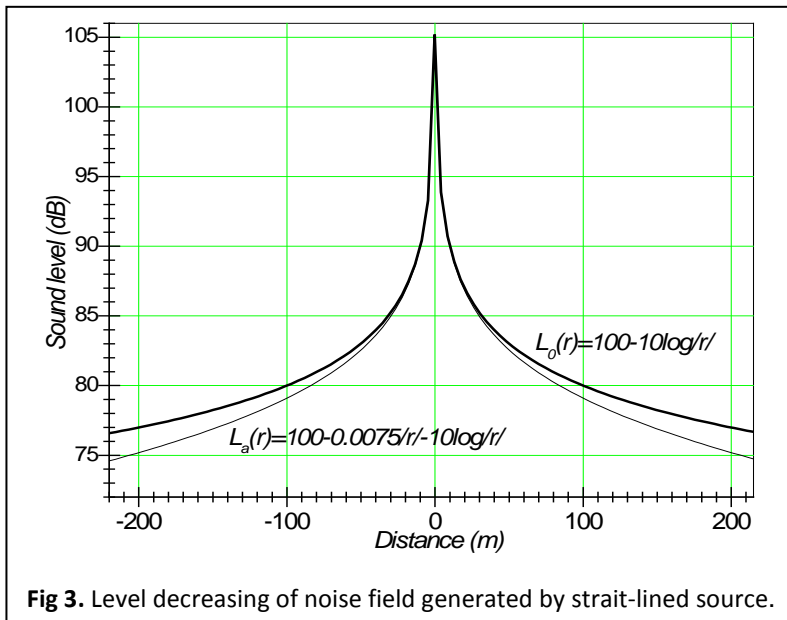


Fig 3. Level decreasing of noise field generated by strait-lined source.

In figure 3 graphs one can see the variation of the real level $L_a(r)$ comparatively with theoretical level $L_o(r)$, without absorption, only through cylindrical divergent scattering. It is necessary to note that in habitual case of air, the absorption causes a linear decreasing of the noise level stronger than the divergent scattering.

4. CONCLUSIONS

Starting from the physical-energetic analysis, we have modeled the emission and propagation of noises produced by rectilinear sources through transversal vibrations of hollow-cylinder or beady string. Our study on modeling the noise field generated by strait-line sources highlights the complexity of phenomenological and mathematical correlations between the observables that characterize sound fields. Having a high degree of generality, our models permit a phenomenological understanding and study of the sound intensity spatial distribution and of energetic and acoustic noise parameters. According to both models, through divergent cylindrical symmetry scattering, the level of the noise generated by strait-lined source decreases linearly with the logarithm of distance to source's axis ($\log r$), slower than for spherical sources with three dimensions sound scattering, which decreases with $\log r^2$. So through scattering, in the noise field, the power dissipation is a 3D phenomenon if the sound front expands as the surface of a sphere $4\pi r^2$ and it is a 2D phenomenon if sound front expands in two dimensions as the circumference $2\pi r$ of a circle.

Correlated with the acoustic and geometric parameters of composed strait-lined sources, trough stochastic mean values, our modeling also allows a prediction of sound level and of noise exposure dose. In conjunction with sonometric measurements and spectral noises analysis, our models can be used for analysis of other various facts of environmental and industrial acoustics. The results presented in this paper may have a wide field of applications and developments. Much of acoustic concepts and data presented in [13, 14, 15, 16], phenomenological explained and specified in our work, can be also implemented in the training of future specialists in environmental ecology.

REFERENCES

1. Skudrzyk, E. (1971). *The Foundations of Acoustics*, Wien: Springer-Verlag.
2. Morse, P.M. (1983). *Vibration and Sound* (2nd edition), New York: The American Institute of Physics.
3. Dowling, A.P. (1977). Steady-state radiation from sources. Chapter 9. In M.J. Crocker (Ed.), *Encyclopedia of Acoustics*, New York: JohnWiley & Sons.
4. Russel, D.A. Sound Radiation from Cylindrical Radiators, <http://www.acs.psu.edu/drussell/Demos/radiation/radiation.html>. Accessed 7 June 2013.
5. Jacobsen, F., Juhl, P. (2011). Radiation of Sound, http://web-files.ait.dtu.dk/fjac/p_home_page/notes/Radiation.pdf. Accessed 10 July 2013.

6. Fahy, F.J. (2003). Sound Energy and Intensity. Chapter 5. In *Foundations of Engineering Acoustics*, (pp. 74-95). Academic Press.
7. Fahy, F.J. (2003). Sources of Sound. Chapter 6. In *Foundations of Engineering Acoustics*, (pp. 96-139). Academic Press.
8. Brunskog, J. (2013). Sound radiation from finite surfaces, *Proceedings of Meetings on Acoustics ICA 2 - 7 June 2013, Montreal, Vol.19*, <http://acousticalsociety.org/>.
9. Morse, P.M. and Ingard, K.U. (2007). *Theoretical Acoustics*, New York: McGraw-Hill.
10. Pierce, A.D. (2007). Basic linear acoustics. Chapter 3. In T.D. Rossing (Ed.), *Springer Handbook of Acoustics*, New York: Springer.
11. Cosma, I., Popescu, D.I. (2010). Entropical Aspects in Auditory Processes and Psychoacoustical Law of Weber-Fechner, *Modern Physics Letters B*, 24(16), 1815-1824
12. Jacobsen, F., Poulsen, T., Rindel, J.H., Gade, A.C., Ohlrich, M. (2011). *Fundamentals of Acoustics and Noise Control*, Technical University of Denmark. <http://www.euitt.upm.es/>. Accessed 12 July 2013.
13. Lamancusa, J.S. (2009). Outdoor Sound Propagation. In *Penn State, Noise Control*, 7/20/2009, http://www.me.psu.edu/lamancusa/me458/10_osp.pdf. Accessed 5 May 2013.
14. Kragh, J. (2001). News and needs in outdoor noise prediction, *The 2001 International Congress and Exhibition on Noise engineering control*, The Hague, Netherlands, 2001 August 27-30. www.madebydelta.com/imported/images/DELTA_Web/documents/TC/acoustics/in01_672.pdf. Accessed 20 October 2013.
15. Carvalho da Paz, E., Zannin, P. H. T. (2010). Urban daytime traffic noise prediction models, *Environmental Monitoring and Assessment*, 163 (1-4), 515-529.
16. Defrance, J. et al. (2007)., Outdoor Sound Propagation Reference Model Developed in European Harmonise Project, *Acta Acustica United with Acustica*, 93, 213-227.

UNIFORMITY DEGREE OF SOME SPHERICAL GRIDS USED IN MAGNETIC RESONANCE POWDER SIMULATIONS

C. CRĂCIUN^{1*}

ABSTRACT. This paper compares the uniformity degree of nine spherical grids used in magnetic resonance powder simulations. The comparison is based on known mesh quality measures, which depend on the grid points and the generated Voronoi regions on the unit sphere. According to computations, the distributions of the grids' geometric properties characterise better the grids' quality than the global uniformity metrics.

Keywords: *spherical grid, uniformity degree, Voronoi cell*

INTRODUCTION

The spherical grids used in magnetic resonance powder simulations have been previously assessed using three approaches. The first approach computes geometric homogeneity metrics, depending on the grid points' location on the unit sphere and the generated Voronoi tessellation [1]. The second approach compares the grids based on the quality of their magnetic resonance simulations [2,3]. The third approach, used in the context of continuous-wave electron paramagnetic resonance (CW EPR) powder simulations, is based on EPR-related metrics [4]. These EPR metrics depend on the distribution of the resonance magnetic fields inside the grids' Voronoi regions.

This paper follows the first approach and computes other uniformity metrics than previously reported for nine spherical grids. The metrics are known mesh quality measures and have been selected from those presented in references [5,6].

The paper is structured as follows. The *Theoretical details* section presents the uniformity metrics. The *Computational details* section describes the numerical methods and the software used in calculations. The results and the grids' comparison are given in the *Results and discussion* section. Final section summarizes current work.

¹ Babeş-Bolyai University, Faculty of Physics, 1 Kogălniceanu str., 400084 Cluj-Napoca, Romania.

* Corresponding author e-mail: cora.craciun@phys.ubbcluj.ro

THEORETICAL DETAILS

For each grid, let P_k , for $k = 1, \dots, N$, be the grid points located on the unit sphere. Each grid point P_k is characterised by its Cartesian coordinates, given as a column vector \mathbf{x}_k . Let denote by V_k the Voronoi cell generated by P_k on the unit sphere. The uniformity metrics computed in this paper are the following [5,6]:

1. The mesh rati

$$\gamma = \frac{\max_{k=1, \dots, N} \gamma_k}{\min_{k=1, \dots, N} \gamma_k} - 1,$$

where γ_k is the minimum Euclidean distance between the grid point \mathbf{x}_k and the other grid points [5]:

$$\gamma_k = \min_{j=1, \dots, N, j \neq k} |\mathbf{x}_k - \mathbf{x}_j|, \text{ for } k = 1, \dots, N.$$

2. The covariance measure

$$\lambda = \frac{1}{\bar{\gamma}} \left[\frac{1}{N} \sum_{k=1}^N (\gamma_k - \bar{\gamma})^2 \right]^{1/2} = \left[N \frac{\sum_{k=1}^N \gamma_k^2}{\left(\sum_{k=1}^N \gamma_k \right)^2} - 1 \right]^{1/2},$$

where $\bar{\gamma} = \frac{1}{N} \sum_{k=1}^N \gamma_k$. The covariance measure represents the relative standard deviation of the γ_k values.

3. The regularity measure

$$\chi = \max_{k=1, \dots, N} \chi_k - 1,$$

where

$$\chi_k = \sqrt{3} h_k / \gamma_k, \text{ for } k = 1, \dots, N,$$

and h_k is the maximum Euclidean distance between the grid point \mathbf{x}_k and the other points of the Voronoi cell V_k :

$$h_k = \max_{\mathbf{y} \in V_k} |\mathbf{x}_k - \mathbf{y}|, \text{ for } k = 1, \dots, N.$$

As in reference [4], each h_k value may be approximated with the Euclidean distance between the grid point \mathbf{x}_k and the furthestmost vertex of its Voronoi cell.

4. The second moment trace measure

$$\tau = \max_{k=1,\dots,N} |T_k - \bar{T}|$$

where:

$$T_k = \text{trace}(\mathbf{M}_k), \text{ for } k = 1, \dots, N, \text{ and } \bar{T} = \frac{1}{N} \sum_{k=1}^N T_k.$$

\mathbf{M}_k is the second moment tensor of the Voronoi cell V_k [6]:

$$\mathbf{M}_k = \frac{1}{M_k} \int_{V_k} (\mathbf{x} - \bar{\mathbf{x}}_k)(\mathbf{x} - \bar{\mathbf{x}}_k)^T d\mathbf{x}$$

where M_k is the zeroth moment (the mass) of V_k :

$$M_k = \int_{V_k} d\mathbf{x}$$

and $\bar{\mathbf{x}}_k$ is the first moment (the centre of mass) of V_k :

$$\bar{\mathbf{x}}_k = \frac{1}{M_k} \int_{V_k} \mathbf{x} d\mathbf{x}.$$

The integral in the expression of the second moment tensor \mathbf{M}_k may be computed probabilistically, by randomly sampling the Voronoi cell V_k with N_k points, \mathbf{y}_j , for $j = 1, \dots, N_k$ [6]:

$$\mathbf{M}_k = \frac{1}{N_k} \mathbf{S}_k - \bar{\mathbf{x}}_k \bar{\mathbf{x}}_k^T$$

where:

$$\bar{\mathbf{x}}_k = \frac{1}{N_k} \sum_{\mathbf{y}_j \in V_k} \mathbf{y}_j \text{ and } \mathbf{S}_k = \sum_{\mathbf{y}_j \in V_k} \mathbf{y}_j \mathbf{y}_j^T.$$

Smaller values of all these uniformity metrics correspond to more uniform grids [5].

COMPUTATIONAL DETAILS

The spherical grids compared in this paper (with abbreviation and size given in parenthesis) are the following: Igloo (562) [7], Lebedev (Leb, 590) [8-13], Spiral (578) [14], Fibonacci (Fib, 579) [15], the Zaremba, Conroy, and Wolfsberg

grid (ZCW, 610) [16-18], the golden ratio-based ZCW (ZCW-n, 578) [4], the Alderman-Solum-Grant grid (ASG, 578) [19], SOPHE (578) [20], and EasySpin (ES, 578) [1,21]. More details about these grids, their generation and random sampling may be found in references [1,2,4]. The Voronoi tessellation of the grids was computed using the STRIPACK package (R.J. Renka) [22], in the implementation available at [23] (stripack.f90, version 2007). For the second moment trace measure, the grids' Voronoi cells were randomly sampled using the J. Arvo's stratified sampling procedure for spherical triangles [24,25] and the pseudo-random number generator from GNU Octave [26,27]. The random sampling was repeated three times for each grid. The spherical grids were sampled with about 392000 random points, as described in [4]. The figures were generated within the R software environment [28].

RESULTS AND DISCUSSION

1. Distribution of the grids' geometric properties

The uniformity metrics presented in this paper depend on geometric quantities calculated for all grid points or for all Voronoi cells of a spherical grid. The mesh ratio γ and the covariance measure λ depend on the shortest distances γ_k ($k = 1, \dots, N$) between the grid points. The regularity measure χ depends on the χ_k values, which are directly proportional to the longest distances h_k between the grid points and the other points of the corresponding Voronoi cells, and inversely proportional to γ_k . The τ measure depends on the traces T_k of the second moment tensors of the Voronoi cells.

Figure 1 shows the distributions of the γ_k , χ_k , and T_k values for the nine investigated grids, in beanplot and boxplot representation [28]. In case of T_k , one out of three distributions obtained by each grid's random sampling is presented. The median, range, and interquartile range (IQR) [28] of the distributions are given in Table 1. The grids have close median values for the same type of distribution and therefore we focus on the range and IQR values.

- a) The Spiral, Igloo, ZCW, ZCW-n, and Fibonacci grids have less distributed γ_k values (lower IQR) than the other grids. This shows that, for these grids, the shortest distances between the grid points are highly homogeneous on the whole unit sphere. The γ_k distributions for Spiral, ZCW, and ZCW-n, however, have high range due to some extreme outliers.

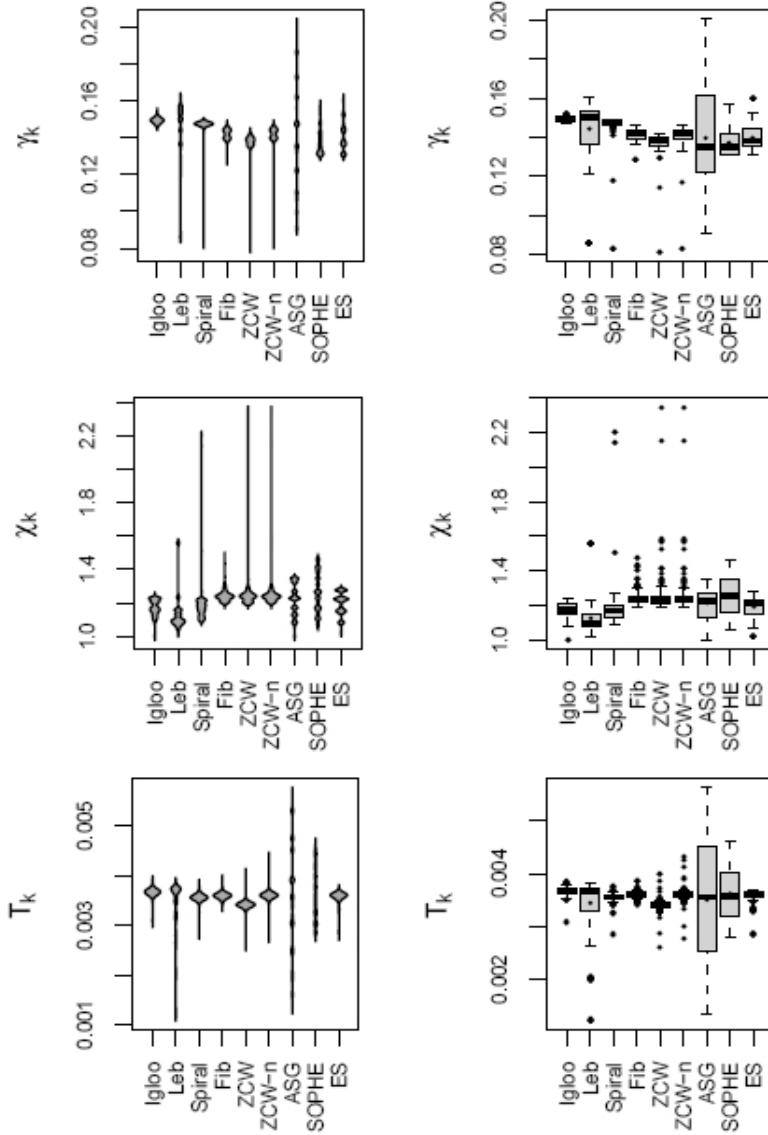


Fig. 1. The distributions of the γ_k , χ_k , and T_k quantities in beanplot (left) and boxplot (right) representation. The boxplots contain: boxes from the first to the third quartile of data (IQR); whiskers up to the most extreme points, but not further than 1.5IQR; a horizontal line inside the boxes for the median and a full knot for the mean value; open knots for the outliers [28].

Table 1. Statistical quantities for the distributions of the grids' geometric properties

Grid	γ_k			χ_k		
	median	range	IQR	median	range	IQR
Igloo	0.1493	0.0055	0.0012	1.1729	0.2409	0.0635
Leb	0.1502	0.0745	0.0174	1.0977	0.5383	0.0751
Spiral	0.1474	0.0642	0.0001	1.1720	1.1124	0.0762
Fib	0.1422	0.0175	0.0045	1.2371	0.2880	0.0323
ZCW	0.1385	0.0610	0.0034	1.2371	1.1598	0.0388
ZCW-n	0.1423	0.0629	0.0045	1.2369	1.1596	0.0327
ASG	0.1351	0.1104	0.0395	1.2259	0.3482	0.1373
SOPHE	0.1352	0.0261	0.0109	1.2559	0.4088	0.1886
ES	0.1383	0.0294	0.0086	1.2154	0.2602	0.0765

Grid	T_k^1		
	median	range	IQR
Igloo	0.0037	0.0008	0.00007
Leb	0.0037	0.0026	0.00045
Spiral	0.0036	0.0009	0.00005
Fib	0.0036	0.0005	0.00004
ZCW	0.0034	0.0014	0.00003
ZCW-n	0.0036	0.0015	0.00004
ASG	0.0036	0.0043	0.00196
SOPHE	0.0036	0.0018	0.00083
ES	0.0036	0.0008	0.00006

¹ The statistical quantities are averages of the values obtained from three random samplings of the grids. For all grids, the ratio between the standard deviation and the mean for the three samplings was 0.01–0.05% for the median, 0.2–5.1% for the range, and 0.1–5.2% for IQR.

EasySpin and SOPHE have more distributed data, but a range which is more than twice smaller than for ZCW and ZCW-n.

- b) The χ_k distributions for the Fibonacci, ZCW, and ZCW-n grids have the smallest IQR values. Nevertheless, the distributions for ZCW and ZCW-n present many outliers and have the highest range. The range is the smallest for Igloo, EasySpin, and Fibonacci grids.
- c) The T_k distributions for the Fibonacci, EasySpin, Igloo, Spiral, ZCW, and ZCW-n grids have lower range and IQR values than for the Lebedev, SOPHE, and ASG grids. In case of SOPHE and ASG, the high IQR values indicate a wide spread of the T_k values within the whole range.

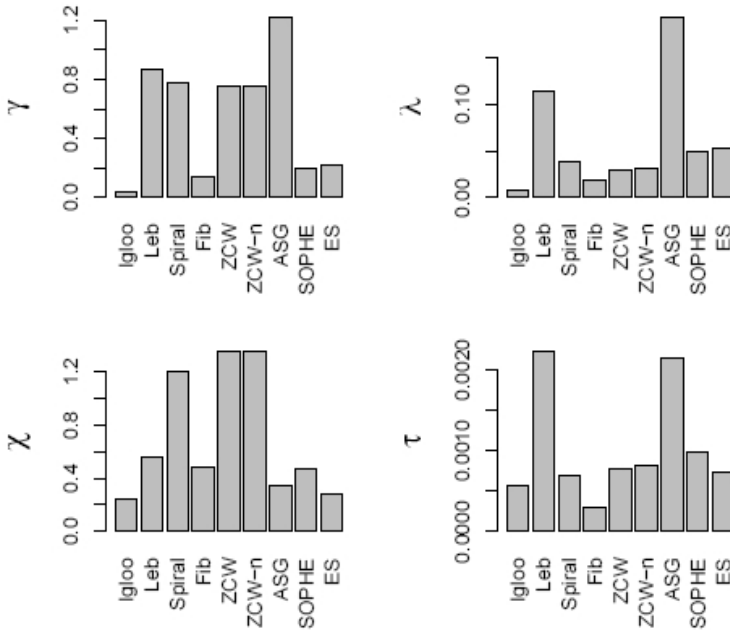


Fig. 2. The uniformity metrics

2. The uniformity metrics

The four metrics computed in this paper, which are global measures of the grids' uniformity, are presented in Figure 2. For each grid, the second moment trace measure τ is the average of the values obtained from three random samplings of the grid.

- The mesh ratio values γ agree with the range values of the γ_k distributions (Table 1). According to γ , Igloo, Fibonacci, SOPHE, and EasySpin are the most uniform. The ZCW, ZCW-n, Spiral, and Lebedev grids have mesh ratio values between 5.5 and 6.4 times higher than the Fibonacci grid, while the ASG grid has a value about nine times higher.
- The covariance measure λ differentiates less than the mesh ratio γ between the spiral-based grids Spiral, ZCW, and ZCW-n, on the one hand, and the triangular grids SOPHE and EasySpin, on the other hand. Based on covariance measure, Igloo and Fibonacci grids are the most uniform and the Lebedev and ASG grids the least.
- Spiral, ZCW, and ZCW-n have the highest regularity measure χ , about 5–6 times higher than Igloo. From the four metrics investigated, the regularity

measure is the single one for which the Lebedev and ASG grids present relatively small values.

- d) The Fibonacci grid has the smallest second moment trace measure τ . The metric is 2–3.5 times higher for Igloo, Spiral, ZCW, ZCW-n, EasySpin, and SOPHE, and about 7.5 times higher for the ASG and Lebedev grids.

It should be noted that all uniformity metrics except the covariance measure λ depend on extreme values of some quantities calculated for the grid points or for the Voronoi cells of the grids. In some cases, the distributions of these quantities are characterised by relatively small IQR values, but present extreme outliers. This is the case, for example, for the χ_k and γ_k distributions of the Spiral, ZCW, and ZCW-n grids. Therefore, the distributions of the grids' geometric quantities characterise better the grids than the uniformity metrics, as already observed in [4].

The comparison of the grids according to the uniformity metrics and distributions is summarised in Table 2. The Fibonacci, Igloo, and EasySpin grids present low-range distributions and relatively small uniformity metrics in most cases. Moreover, the Fibonacci, ZCW, ZCW-n, Spiral, Igloo, and EasySpin grids have distributions with relatively low IQR values. As shown in reference [4], the Fibonacci, ZCW, ZCW-n, Spiral, and EasySpin grids do also generate low-noise simulated CW EPR powder spectra for some spin system symmetries.

Table 2. The spherical grids, in increasing order according to the uniformity metrics and the grids' geometric properties

Metric		The grids' order
γ_k	range	Igloo, Fib, SOPHE, ES, ZCW, ZCW-n, Spiral, Leb, ASG
	IQR	Spiral, Igloo, ZCW, ZCW-n, Fib, ES, SOPHE, Leb, ASG
γ		Igloo, Fib, SOPHE, ES, ZCW, ZCW-n, Spiral, Leb, ASG
λ		Igloo, Fib, ZCW, ZCW-n, Spiral, SOPHE, ES, Leb, ASG
χ_k	range	Igloo, ES, Fib, ASG, SOPHE, Leb, Spiral, ZCW-n, ZCW
	IQR	Fib, ZCW-n, ZCW, Igloo, Leb, Spiral, ES, ASG, SOPHE
χ		Igloo, ES, ASG, SOPHE, Fib, Leb, Spiral, ZCW, ZCW-n
T_k	range	Fib, Igloo, ES, Spiral, ZCW, ZCW-n, SOPHE, Leb, ASG
	IQR	ZCW, Fib, ZCW-n, Spiral, ES, Igloo, Leb, SOPHE, ASG
τ		Fib, Igloo, Spiral, ES, ZCW, ZCW-n, SOPHE, ASG, Leb

CONCLUSIONS

This paper has compared nine spherical grids used in magnetic resonance powder simulations, according to the following uniformity metrics: the mesh ratio,

the covariance, the regularity, and the second moment trace measure. The metrics depend on geometric quantities, such as distances between the grid points or between points of the Voronoi cells. For each spherical grid, these quantities have some distribution on the unit sphere. Three out of four investigated metrics depend only on the distributions' extreme values, which may be some outliers. Therefore, the distributions of the grids' geometric properties are better measures of the grids' quality than the global uniformity metrics.

REFERENCES

1. S. Stoll, Ph.D. Thesis, ETH Zurich, Switzerland, 2003.
2. A. Ponti, *J. Magn. Reson.*, 138, 288 (1999).
3. M. Bak, N.C. Nielsen, *J. Magn. Reson.*, 125, 181 (1997).
4. C. Crăciun, *J. Magn. Reson.*, 245, 63 (2014).
5. H. Nguyen, J. Burkardt, M. Gunzburger, L. Ju, Y. Saka, *Comput. Geom.*, 42, 1 (2009).
6. J. Burkardt, M. Gunzburger, J. Peterson, R. Brannon, Technical Report: SAND2002-0099, Sandia National Laboratories, February 2002.
7. M.J. Nilges, Ph.D. Thesis, University of Illinois, Urbana, Illinois, 1979.
8. V.I. Lebedev, *Comput. Math. Math. Phys.*, 15, 44 (1975).
9. V.I. Lebedev, *Comput. Math. Math. Phys.*, 16, 10 (1976).
10. V.I. Lebedev, *Siberian Math. J.*, 18, 99 (1977).
11. V.I. Lebedev, A.L. Skorokhodov, *Russ. Acad. Sci. Dokl. Math.*, 45, 587 (1992).
12. V.I. Lebedev, *Russ. Acad. Sci. Dokl. Math.*, 50, 283 (1995).
13. V.I. Lebedev, D.N. Laikov, *Russ. Acad. Sci. Dokl. Math.*, 59, 477 (1999).
14. M.J. Mombourquette, J.A. Weil, *J. Magn. Reson.*, 99, 37 (1992).
15. R. Swinbank, R.J. Purser, *Quart. J. Roy. Meteorol. Soc.*, 132, 1769 (2006).
16. S.K. Zaremba, *Ann. Mat. Pura Appl.*, 73, 293 (1966).
17. H. Conroy, *J. Chem. Phys.*, 47, 5307 (1967).
18. V.B. Cheng, H.H. Suzukawa Jr., M. Wolfsberg, *J. Chem. Phys.*, 59, 3992 (1973).
19. D.W. Alderman, M.S. Solum, D.M. Grant, *J. Chem. Phys.*, 84, 3717 (1986).
20. D. Wang, G.R. Hanson, *J. Magn. Reson. A*, 117, 1 (1995).
21. S. Stoll, A. Schweiger, *J. Magn. Reson.* 178, 42 (2006).
22. R.J. Renka, *ACM Trans. Math. Softw.*, 23, 416 (1997).
23. http://people.sc.fsu.edu/~jburkardt/f_src/f_src.html
24. J. Arvo, in: S.G. Mair, R. Cook (Eds.), Proceedings of the 22nd Annual Conference on Computer Graphics and Interactive Techniques (SIGGRAPH '95), ACM, New York, pp. 437-438 (1995).
25. J. Arvo, Stratified sampling of 2-manifolds, in: SIGGRAPH 2001 Course Notes, vol. 29 (2001).
26. <http://www.gnu.org/software/octave/>
27. M. Matsumoto, T. Nishimura, *ACM Trans. Model. Comput. Simulat.*, 8, 3 (1998).
28. <http://www.r-project.org/>

SURFACTANT EFFECT ON THE STRUCTURAL AND MAGNETIC PROPERTIES OF Fe POWDERS PREPARED BY WET MILLING

R. HIRIAN¹, S. MICAN^{1*}, B. NEAMȚU², V. POP¹

ABSTRACT. The effect of wet milling with benzene on the structural and magnetic properties of Fe powder was investigated. Average crystallite sizes of 14 nm and 7 nm were obtained for the dry-milled and wet-milled samples respectively. It was found that benzene reacts with the Fe powder during wet milling, carbon entering into the Fe structure. After annealing, the average crystallite sizes remained at 27 nm for dry-milled Fe and 25 nm for wet-milled Fe. Some of the benzene evaporated during annealing, however, a significant amount of benzene still remained in the powder mixture after annealing.

Keywords: ball milling, surfactant, α -Fe, powders, crystal structure, microstructure.

INTRODUCTION

Permanent magnets are used in a wide range of applications from small-scale electric and electronic devices to large-scale energy applications, becoming critical components for the development of advanced technologies. Recent developments in applications like the growing hybrid and electric car industry and in the energy sector with applications in wind turbine generators [1-3], where the quantity of magnetic materials is very high, have caused a strong increase in the demand for permanent magnets. Until recently, the lowest cost per energy-density unit was obtained for Nd₂Fe₁₄B-type permanent magnets [2-5]. However, a major disadvantage of rare-earth-based permanent magnets has emerged lately due to the high and fluctuating market price and unreliable supply of rare-earth elements [6, 7]. A proposed solution to this problem is to use magnets with

¹ Babeş-Bolyai University, Faculty of Physics, 400084, Cluj-Napoca, Romania.

* corresponding author e-mail: sever.mican@ubbcluj.ro

² Technical University of Cluj-Napoca, Materials Science and Engineering Department, RO-400641, Cluj-Napoca, Romania

reduced or no rare-earth content such as manganese based materials, soft/hard magnetic nanocomposites (spring magnets) [8] or the tetragonal distorted Fe based alloys or Fe-Co materials. For the new Fe₁₆N₂ phase obtained by chemical methods or in thin layers, the iron magnetic moment was reported to be 3.0 μ_B /Fe [9-11]. The problem, which remains to be solved, is given by the rather low coercivity and thermal stability. The introduction of atomic nitrogen in to the Fe structure is not a trivial task, as we want to avoid the formation of Fe-N chemical compounds. A proposed solution is to synthesise nitrided nano sized Fe powders by means of mechanical milling or annealing in a nitrogen rich atmosphere. The Fe crystallite size and distribution can be controlled through properly selected milling parameters, the most important ones being milling type, milling energy (speed and time), and process control agents (lubricants and surfactants) [12]. The use of a surfactant during milling minimizes cold welding between particles [12]. However, the surfactant can interact with the powder during milling, forming compounds which get incorporated into the powder particles during milling [12]. Hydrocarbons could introduce carbon into the powder particles, resulting in the formation of carbides [12]. In this work we investigate the effect of dry and wet milling on the structural and magnetic properties of Fe powders. The microstructure evolution and the elimination of the surfactant, used for wet milling, were investigated in annealed Fe powders.

EXPERIMENTAL DETAILS

The starting material used in this study was commercial NC 100.24 Fe powder (Höganäs product) below 40 μm . Two samples of milled Fe were prepared using a planetary mill (Fritsch Pulverisette 4). The first Fe powder sample was dry-milled in Ar for 4 h. The second sample was prepared by milling Fe powder mixed with 5 ml of benzene under Ar for 4 h. The milling vials (with a volume of 80 ml) and balls (diameter $\varnothing = 15$ mm) were made of 440C hardened steel. The ratio between the rotation speed of the disk and the relative rotation speed of the vials was $\Omega/\omega=333/900$ rpm with a ball-to-powder weight ratio of 10:1. Differential thermal analysis (DTA) was employed to study the structural transformations and phase transitions in the temperature range 100-700 °C under Ar atmosphere with a temperature ramp rate of 20 °C/min. A heat treatment was done at 400 °C for 1 h under vacuum. The structure and microstructure of the Fe powder samples were investigated using an Inel Equinox 3000 X-Ray diffractometer with Co K α radiation and Bragg-Brentano focusing geometry. The average crystallite sizes of the powder samples were determined from the full width at half-maximum (FWHM) values of the diffraction peaks using the Williamson-Hall method [13]. The FWHM values were obtained by fitting the peaks using a normalized pseudo-

Voigt function. For the calculation of the average crystallite size, the instrumental contribution to the peak width was subtracted from the obtained FWHM values. The instrumental broadening was measured from the X-ray diffraction pattern of a reference sample. Magnetic susceptibility versus temperature measurements were recorded using a Faraday balance.

RESULTS AND DISCUSSIONS

The DTA curve of the 4 h wet-milled Fe sample shows two peaks centred around 330 °C and 550 °C respectively, which are not present in the dry milled samples, Figure 1. The 4 h wet-milled Fe sample annealed at 400 °C for 1 h shows only one DTA peak, around 550 °C. The absence of the peak at 330 °C in the annealed wet-milled sample could indicate the evaporation of benzene from the powder mixture. The peak at 550 °C corresponds to the decomposition of benzene into diphenyl [14]. The presence of this peak in the annealed wet-milled Fe sample indicates that while most of the benzene has evaporated, there is a significant quantity still mixed with the milled Fe powder. This fact proves the importance of the milling environment on the physical properties of milled powders.

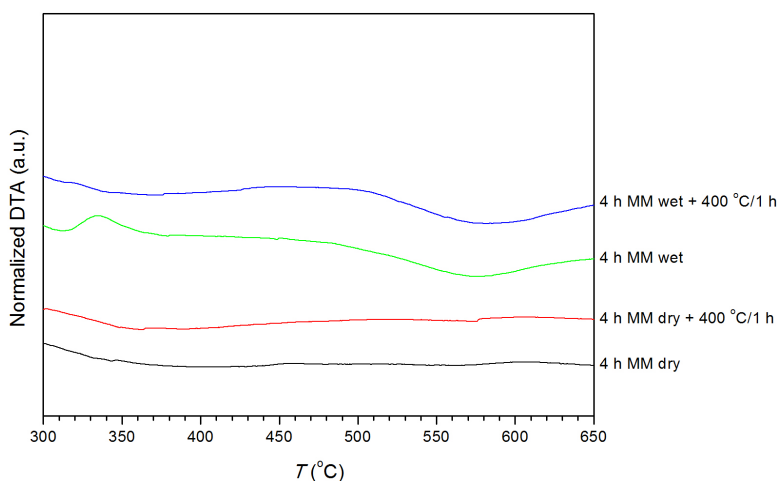


Fig. 1. Differential thermal analysis curves for the 4 h MM as-milled and annealed samples. For clarity, the curves were shifted vertically.

The X-ray diffraction (XRD) patterns for the as-milled and annealed Fe samples, along with the starting Fe sample are shown in Figure 2. The XRD peaks get broader after milling due to the smaller Fe crystallite sizes, Table 1, and the

presence of strain induced by milling. The Fe XRD peaks of the wet-milled sample are broader than those of the dry-milled one due to the smaller Fe crystallites of the wet milled sample. This is due to the reduced effect of cold welding during milling [12]. Because of the elimination of internal stress and crystallite growth after annealing, the XRD peak width diminishes. It is worthwhile to note that the annealed wet-milled Fe sample shows slightly smaller crystallite sizes compared to the annealed dry-milled one, Table 1.

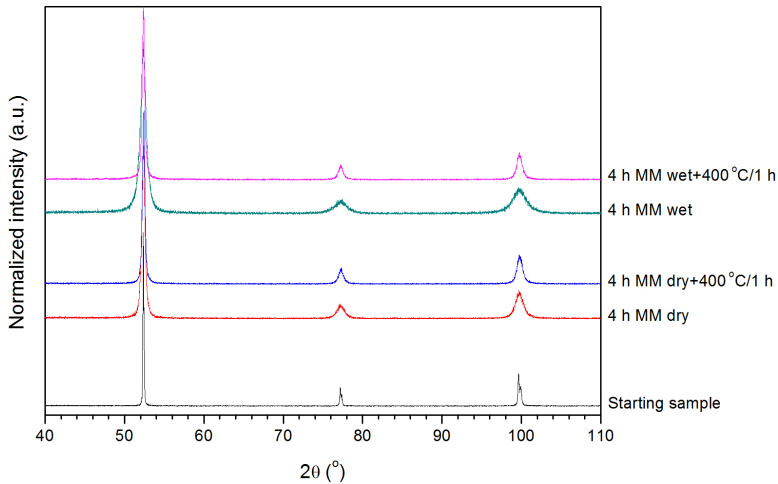


Fig. 2. X-ray diffraction patterns of the as-milled and annealed Fe samples. The XRD pattern of the starting Fe sample is shown for comparison. For clarity, the curves were shifted vertically.

Table 1 Average crystallite sizes, d , determined from XRD patterns for the as-milled and annealed Fe samples.

Sample	d (nm) \pm 2 nm
Fe 4 h MM dry	14
Fe 4 h MM wet	7
Fe 4 h MM dry + 400 °C/1 h	27
Fe 4 h MM wet + 400 °C/1 h	25

The thermomagnetic measurements for the as-milled samples, Figure 3, show that the 4 h dry-milled Fe sample shows almost no thermal hysteresis and a Curie temperature of about 765 °C. However, the 4 h wet-milled Fe sample shows a lower Curie temperature around 745 °C and a very broad thermal hysteresis. The lower Curie temperature of the wet-milled sample could be attributed to the

introduction of carbon in the Fe structure during milling due to the decomposition of benzene [12]. The broad thermal hysteresis could be attributed to the transformation of pearlite into austenite [15]. A similar behaviour was reported in the resistivity versus temperature curves for Fe containing 0.83% carbon, the pearlite to austenite transformation taking place around 730 °C and the reverse transformation occurring around 690 °C [15].

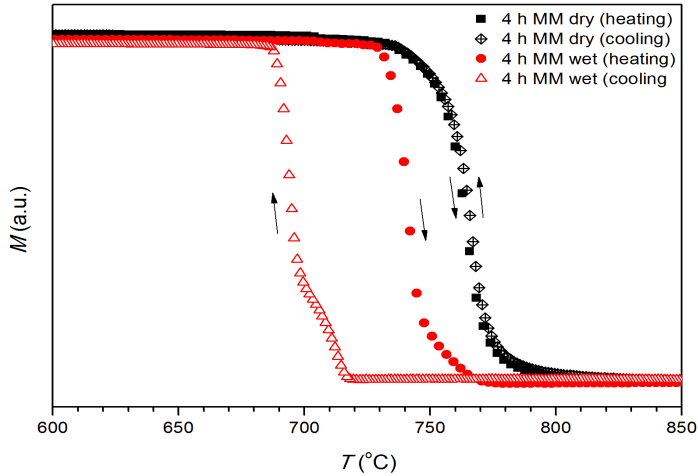


Fig. 3. Magnetization versus temperature curves during heating and cooling for the 4 h as-milled Fe samples.

CONCLUSIONS

The effect of dry and wet mechanical milling on the structural and magnetic properties of Fe powders was investigated. DTA investigations have shown that benzene evaporates during annealing, however, there was a significant quantity still mixed with the milled Fe powder after annealing. Milling with benzene led to smaller Fe crystallite sizes in both the as-milled and annealed samples. Thermomagnetic measurements indicated the entering of C in the Fe structure during wet milling, resulting from the decomposition of benzene.

ACKNOWLEDGMENT

The authors would like to acknowledge support from the Romanian UEFISCDI Project No. PN-II-PT-PCCA-2013-4-0971.

REFERENCES

1. R. Skomski, P. Manchanda, P. Kumar, B. Balamurugan, A. Kashyap, and D. J. Sellmyer, *IEEE Trans. Magn.*, 49, 3215 (2013).
2. N. Poudyal and J. P. Liu, *J. Phys. D: Appl. Phys.*, 46, 043001 (2013).
3. R. L. Stamps, S. Breitzkreutz, J. Åkerman, A. V. Chumak, Y. Otani, G. E. W. Bauer, J.-U. Thiele, M. Bowen, S. A. Majetich, M. Kläui, I. L. Prejbeanu, B. Dieny, N. M. Dempsey, and B. Hillebrands, *J. Phys. D: Appl. Phys.*, 47, 333001 (2014).
4. O. Gutfleisch, M. A. Willard, E. Brück, C. Chen, S. G. Sankar, and J. P. Liu, *Adv. Mater.*, 23, 821 (2011).
5. E. Burzo, *Rep. Prog. Phys.*, 61, 1099 (1998).
6. A. Golev, M. Scott, P. D. Erskine, S. H. Ali, and G. R. Ballantyne, *Resources Policy*, 41, 52 (2014).
7. L. Baldi, M. Peri, and D. Vandone, *Energy Policy*, 66, 53 (2014).
8. E. Kneller and R. Hawig, *IEEE. Trans. Magn.*, 27, 3588 (1991).
9. Migaku Takahashi, H. Shoj, *J. Magn. Magn. Matter.*, 208, 145 (2000).
10. Eiji Kita, K. Shibata, H. Yanagihara, Y. Sasaki, M. Kishimoto, *J. Magn. Magn. Matter.*, 310, 2411 (2007).
11. Jian-Ping Wang Nian Ji, Xiaoqi Liu, Yunhao Xu, C. Sanchez-Hanke, *APS March Meeting 2010*, abstract T33.003.
12. C. Suryanarayana, *Prog. Mater. Sci.*, 46, 1 (2001).
13. G. K. Williamson and W. H. Hall, *Acta Metallurgica*, 1, 22 (1953).
14. J. Zanetti and G. Egloff, *The Journal of Industrial and Engineering Chemistry*, 9, 350 (1917).
15. I. E. Kontorovich, "Heat Treatment of Steel and Cast Iron", Metallurgizdat, Moscow, 1950, chapter 1.

FORMULATION AND OPTIMIZING OF A SKIN BARRIER REGENERATING COSMECEUTICAL PRODUCT

A. M. JUNCAN^{1*}

ABSTRACT. This study has as main objective the development and formulation of a skin barrier regenerating dermatocosmetic product for daily care, which incorporates effective emollients, such as Shea butter, an emollient and moisturizing cosmetic ingredient recognized for its regenerative effects, and an innovative emollient - Sucragel AOF (Glycerin (and) Prunus Amygdalus Dulcis (Sweet Almond) Oil (and) Sucrose LAURATE (and) Citrus Aurantium Dulcis (Orange) with moisturizing proven cosmetic efficacy and GATULINE® BIO SKIN-REPAIR (Alcohol (and) Water (and) onopordum Acanthium Flower/Leaf/Stem Extract), used in the developed formulation to support the cosmetic claimed of the product. An important study is the quality control of the regenerating cream by determining the physico-chemical characteristics and appropriate pharmacotechnical (pH, viscosity) characteristics, both initially and over time (30 days from the preparation of the product). The formulation is monitored under accelerated stability studies over a period of 30 days while maintaining the product at 4, 20 and 40 °C.

Keywords: *cosmeceutical, skin barrier regenerating, physico-chemical characteristics, accelerated stability studies*

INTRODUCTION

New insights about the function of the skin, as well as the development of new products for skin care, make it necessary to question or redefine the definitions of cosmetics and drugs.

The introduction of the term “cosmeceutical” enables us to classify more precisely a product with an activity that is *intended* to treat or prevent a (mild) skin (abnormality) [1]. In order to avoid introducing new definition criteria, it was

¹ “Vasile Goldiș” Western University of Arad, Faculty of Pharmacy, Liviu Rebreanu Str. 86, 310045, Arad, Romania. S.C FarmPrev SRL, Suceava Str. 24-26, 400219, Cluj-Napoca, Romania.

* Corresponding author e-mail: anca_juncan@yahoo.com

suggested that cosmeceuticals are only regarded as a subclass within the domain of a cosmetic or drug.

The desire to maintain a youthful image combined with an emerging global market with disposable income has driven the development of many new industries. The cosmeceutical industry is based on the development and marketing of products that lie between cosmetics and pharmaceuticals. Although a number of products advertise predictable outcomes, the industry is largely unregulated and any consumers of cosmeceutical products should consult a dermatologist prior to use.

Dr. Albert Kligman originally coined the term cosmeceutical, describing a hybrid category of products found on the spectrum between drugs and cosmetics that exert a pharmaceutical therapeutic benefit but not necessarily a biological therapeutic benefit. Cosmeceuticals have become the fastest-growing segment of the personal care industry. Consumers and dermatologists alike can be overwhelmed with the sheer number of cosmeceutical products available. The multitudes of products are not strictly regulated, and consumers are often exposed to product information that is not scientifically sound or backed by rigorous clinical studies. Although certain cosmeceuticals may not deliver the effects they claim, there may be benefits because of their emollient action, although it is difficult to discern whether these effects can be attributed to the active ingredient or the vehicle. Recent trends in cosmeceutical development include those that address skin protection from radiation and oxidant damage, with a focus on nonirritating ingredients to improve the appearance of skin.

Skincare cosmeceuticals account for approximately 80% of the total U.S. and European cosmeceutical market. In 2011, the cosmeceutical market resumed growth rates close to those experienced between 2004 and 2007. U.S. demand for cosmeceuticals was projected to increase by 7.4% in 2012 and to continue to increase in the subsequent years (Figure 1) [2].

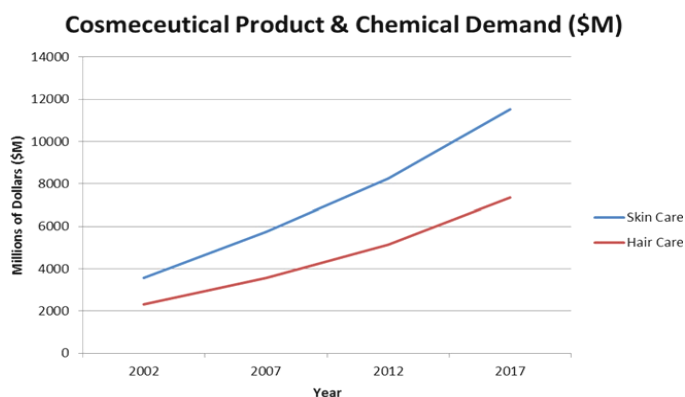


Fig. 1. Cosmeceutical product and chemical demand (\$M) for hair and skin care

The essence of innovative cosmeceuticals is their functional active ingredients. Hundreds of substances have been screened, synthesized, and tested and many have been included in commercially available products. The desired functions of a cosmeceutical might require a coordinating action of multiple ingredients. Moreover, there are problematic skin conditions that might change the interactive pattern and outcome between cosmeceuticals and skin. Scientific clinical evaluation is a must for research, development, and application of cosmeceuticals [3].

Millions of people suffer daily from skin dryness itching, scaling, and redness due to a large variety of causes. The skin barrier, composed of corneocyte and intercellular lipids, can only withstand a finite amount of damage until skin disease results. Predisposing factors to skin disease include low humidity conditions from cold dry weather and insufficient or defective sebum production [4].

“Dry skin” is a term used by consumers, cosmetic scientists, and dermatologists. Although this condition remains one of the most common of human disorders, it has never been defined unambiguously. Usually it is described in terms of symptomatology, its physical signs, and its etiology with names such as xerosis, dermatitis, winter itch, rough skin, dry skin, and chapping. However, dry skin is characterized by a rough, scaly and flaky skin surface, especially in low humidity conditions and is often associated with the somatory sensations of tightness, itch, and pain [5].

Dry skin is one of the common problems due to defective stratum corneum. It is a condition featured by some subjective or objective denominators, including sensory characteristics with dry, uncomfortable, itchy, stinging, and tingling sensation; tactile characteristics with a rough, uneven, and sandlike feeling; and visible characteristics with redness, lackluster surface, dry, white patches, flaky appearance, cracks, and even fissures. In addition, several skin diseases are also featured by dry skin, including atopic dermatitis, ichthyosis, and the like. Moisturizers are agents designed to repair the damaged stratum corneum to make the stratum corneum softer and more pliant by increasing its hydration, resulting in smooth, more supple, and healthier looking skin. Moreover, moisturizers are also designed to act as adjuvant treatment option for some dermatologic diseases with feature of dry skin. From the view of safety, therapeutic moisturizers should be noncomedogenic, devoid of irritant ingredients, and compatible with many other therapeutic regimens [3].

Moisturizers have been traditionally used to alleviate dry skin. They can reduce transepidermal water loss by promoting barrier repair, soothe exposed dermal nerve endings by creating a temporary artificial barrier, and restore skin softness. Recently, moisturizers have been shown to prevent the induction of primary irritation and to accelerate the process by which the skin heals itself. This

is an important function, since a quality moisturizer formulation should not only reduce dry skin and irritation, but also prevent the return of these conditions, which can lead to skin disease [4].

The demand for effective non-prescription topical products to treat inflammatory diseases such as eczema, atopic dermatitis, seborrheic dermatitis, and even psoriasis has led to the introduction of products based on either novel synthetic chemicals or on botanical “actives” which claim to be effective anti-inflammatory compounds. Some of the many purported botanical anti-inflammatory “active” ingredients in cosmeceutical products include bee pollen, curry extract, jewelweed, green tea extract, aloe, bilberry, tea tree oil, lavender essential oil, *Boswellia*, and willow bark. Although there are a wide number of topical anti-inflammatories available as prescriptions which are effective in treating skin inflammation, all have some side effects that negatively impact their usefulness. Topical steroids are effective for treating many dermatologic diseases but can lower collagen production in dermal fibroblasts, reduce their proliferation, and cause skin thinning. Topical immunomodulators are immunosuppressive and can lead to increased risk for infection and even cancer. Clearly, there is a continued need for identifying newer anti-inflammatory technologies that effectively treat skin disorders without having such strong immunosuppressive effects. Botanically derived anti-inflammatory compounds as well as newer synthetic drugs, should help meet this need [6].

EXPERIMENTAL

Qualitative data of the skin barrier regenerating cream formulation is presented in Table 1.

Figure 2 shows by comparison, the composition of the studied cream. The different ratios between lipophilic and hydrophilic components are noticed.

Standards and Reagents

Sample preparation of the skin barrier regenerating cream

Phase A (SUCRAGEL AOF (Glycerin, Prunus Amygdalus Dulcis (Sweet Almond) Oil, Sucrose Laurate, Aqua), Cerasynt SD (Glyceryl Stearate), Lanette D (Cetearyl Alcohol), Shea butter (Butyrospermum Parkii), Cacao butter (Theobroma Cacao), Jojoba (Simmondsia Chinensis) Oil, Phytosqualan (Squalane), dermofeel® TOCO 70 non-GMO (Tocopherol, Helianthus Annuus (Sunflower) Seed Oil)) was melted on water bath at 75°C. Phase B (demineralized water, dermorganics® Glycerin (Glycerin),

dermosoft® LP (Caprylyl Glycol, Glycerin, Glyceryl Caprylate, Phenylpropanol)) was heated at 80°C. Phase A1 (xanthan gum) was dispersed in phase B. Phase A was emulsified with phase B under stirring and cooling down to 40°C was started under medium stirring. Phase C (GATULINE® SKIN-REPAIR BIO (Alcohol (and) Water (and) Onopordum Acanthium Flower/Leaf/Stem Extract) and Honey LG (Mel Extract) was added under stirring.

Table 1. Qualitative formulation Skin barrier regenerating cream

Phase	Ingredient	INCI designation	Function	Supplier
A	SUCRAGEL AOF	Glycerin, Prunus Amygdalus Dulcis (Sweet Almond) Oil, Sucrose Laurate, Aqua	emollient	AlfaCos
	Cerasynt SD	Glyceryl Stearate	emollient/emulsifying	ISP
	Lanette D	Cetearyl Alcohol	emollient/emulsifying/emulsion stabilising/opacifying/viscosity controlling	Cognis
	Karite CP	Butyrospermum Parkii Butter	skin conditioning/emollient	SOPHIM
	Cacao Butter	Theobroma Cacao Butter	emollient	Sophim
	Jojoba oil	Simmondsia Chinensis Oil	emollient	SOPHIM
	Phytosqualane	Squalane	emollient/skin conditioning	SOPHIM
	dermofeel® TOCO 70 non- GMO	Tocopherol, Helianthus Annuus (Sunflower) Seed Oil	antioxidant	Dr. Straetmans
A1	Keltrol RD	Xanthan Gum	binding/emulsion stabilising/viscosity controlling/gel forming	CP Kelco
B	Deionised Water	Aqua	solvent	/
	dermorganics® Glycerin	Glycerin	denaturant/humectant /solvent	Dr. Straetmans
	dermosoft® LP	Caprylyl Glycol, Glycerin, Glyceryl Caprylate, Phenylpropanol	preservative	Dr. Straetmans
C	GATULINE® SKIN-REPAIR BIO	Alcohol (and) Water (and) Onopordum Acanthium Flower/Leaf/Stem Extract	active ingredient	Gattefosse
	Honey LG	Mel Extract	active ingredient	Naturex

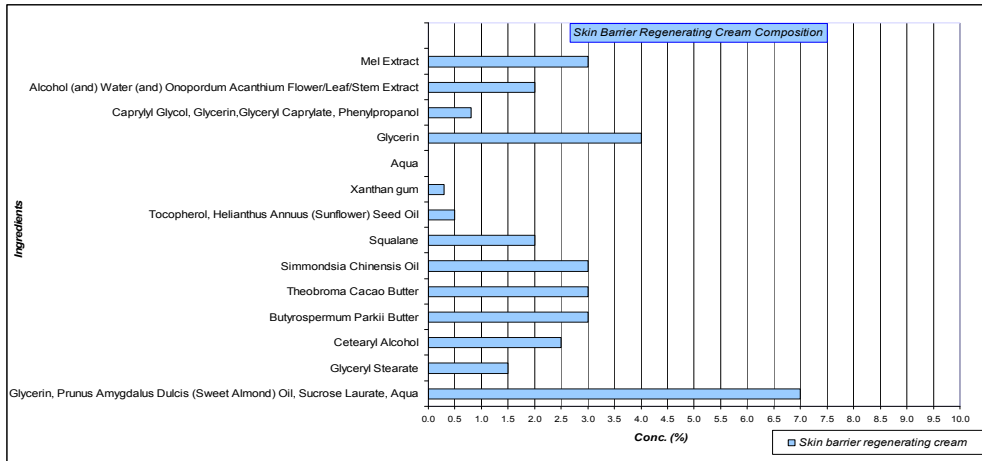


Fig. 2. The composition of the Skin barrier regenerating cream in a graphical representation

Physico-chemical characteristics of the developed Skin barrier regenerating cream- relevant characteristics, acceptance criteria, test methods

Quality control consisted of the following determinations:

Appearance

The appearance, color and odor were tested organoleptically.

pH determination

Was performed using a pH meter (Mettler Toledo (Schwerzenbach, Switzerland)).

Determination of the viscosity

Was performed using a HAAKE Viscotester VT550 (spindle R = 6, shear rate $D=5\text{ s}^{-1}$, temperature $T=20^{\circ}\text{C}$).

Accelerated stability studies

The developed dermatocosmetic formulation was monitored under accelerated stability studies. Accelerated stability tests were performed over a period of 30 days while maintaining the product at 4, 20 and 40 ° C.

RESULTS AND DISCUSSION

Presentation report of the developed dermatocosmetic formulation

The Skin barrier regenerating cream is specially created as a dermatocosmetic

formulation and as contained active ingredients for sensitive skin, irritated, dry, with tendency of dehydration. The formulated cream associates a complex of emollients (Jojoba, Squalane, Shea butter) with role in restoring the hydro-lipid protective barrier of the skin, contributing to a good softening and moisturizing of the sensitive skin with innovative active ingredients with specific action- directly stimulates epidermal regeneration and promotes cutaneous repair (GATULINE® BIO SKIN-REPAIR (INCI name Alcohol (and) Water (and) Onopordum Acanthium Flower/Leaf/Stem Extract).

Phytosqualane has a geriatric type activity on wrinkled skin, reducing fine lines.

Shea butter is known for its excellent softening, moisturizing and nourishing properties with a good spreadability and leaving a non greasy feeling to the skin.

α -tocopheryl acetate (dermofeel® E 74 A) is an effective antioxidant, helping to combat skin aging processes caused by free radicals. It softens the skin and improves skin elasticity.

Honey extract tones and revitalizes, restores and nourishes the skin, restores altered connective tissue due to external factors.

Applied regularly, the developed dermatocosmetic cream means an ideal product for improving the appearance of sensitive, irritated and dehydrated skin. The cream prevents and alleviates skin irritation, restores the skin's water balance and ensures effective hydration throughout the day.

Physico-chemical characteristics of the developed Skin barrier regenerating cream

Quality control of the developed dermatocosmetic cream revealed: achieving an acceptable cosmetic preparation with elegant appearance and appropriate physico-chemical and pharmacotechnical (pH, viscosity) characteristics. The initial determination results are shown in Table 2.

Table 2. Initial physico-chemical determination of the cosmeceutical cream

Nr.	Properties	Admissibility conditions
1.	Appearance	- homogeneous emulsion
2.	Colour	- soft light white
3.	Odour	-characteristic
4.	pH	- 5,5
5.	Viscosity	-6.500 mPas.S

Accelerated stability studies performed over a period of 30 days, while maintaining the product at 4, 20 and 40°C, showed that the formulated and studied dermatocosmetic product is stable. The results are shown in Table 3.

Table 3. Physico-chemical determination of the cosmeceutical cream

<i>Test</i>	<i>Admissibility conditions (initial)</i>	<i>Admissibility conditions (after 30 days)</i>
Appearance	homogeneous emulsion	proper
Odour	characteristic	proper
Colour	soft light white	proper
pH	5,5	5,5
Viscosity	5.500 mPas.S	6.500 mPas.S

CONCLUSIONS

Cosmetics are commercially available products that are used to improve the appearance of the skin. Consumer demand for more effective products that more substantively beautify the appearance has resulted in increased basic science research and product development in the cosmetics industry. The result has been more ingredients that may actually improve not just the appearance of the skin, but the health of the skin as well. We now have products that renew, restore, and rejuvenate—not just cleanse, protect, and moisturize [7]. The latest innovation in the field of cosmetics is the development of active cosmetics.

Currently, cosmetics are not only intended for the improvement of the appearance or odor of the consumer, but are also intended for the benefit of their target, whether it is the skin, the hair, the mucous membrane, or the tooth. With this functional approach, products became diversified and started to claim a multitude of actions on the body. In order for cosmetic products to support these activities, raw materials became more efficacious, safe, bioavailable, and innovative, while remaining affordable. Subsequently, the cosmetic market greatly expanded, becoming accessible to millions of consumers worldwide [8].

The research presented in this paper had as main objective the development and formulation of a skin barrier regenerating dermatocosmetic. The developed dermatocosmetic formulation associates two valuable emulsifiers for effective support of the cosmetic cream- Shea butter, a known emollient in cosmetics for its regenerative and moisturizing effects and Sucragel AOF with strong moisturizing effects. The developed formulation incorporates an innovative active ingredient- GATULINE® BIO SKIN-REPAIR (Alcohol (and) Water (and) Onopordum Acanthium

Flower/Leaf/Stem Extract)- acting on keratinocyte differentiation, stimulating the optimal epidermal reconstruction of dry or damaged skin. The emollient raw materials, respectively Shea butter was added in a 5% concentration in the formulation and Sucragel AOF in 7%. The concentration of active ingredient has been introduced in the formulation at a concentration of 2%. The cream prevents and alleviates skin irritation, restores the skin's water balance and ensures effective hydration.

Quality control of the developed dermatocosmetic cream revealed: achieving an acceptable cosmetic preparation with elegant appearance and appropriate physico-chemical and pharmacotechnical (pH, viscosity) characteristics (after preparation and after 30 days of preparation).

Accelerated stability studies performed over a period of 30 days, while maintaining the product at 4, 20 and 40°C, showed that the formulated and studied dermatocosmetic product is stable.

ACKNOWLEDGMENTS

Special thanks are extended to Azelis Romania for providing cosmetic ingredients used for the cosmeceutical product formulation.

REFERENCES

1. P. Elsner, H. I. Maibach, "Cosmeceuticals. Drug vs. Cosmetics", Marcel Dekker, New York, 2000, chapter 2.
2. F. S. Brandt, A. Cazzaniga, M. Hann, *Semin. Cutan. Med. Surg.*, 30 (2011).
3. X.-H. Gao, L. Zhang, H. Wei, H.-D. Chen, *Clin. Dermatol.*, 26 (2008).
4. A. F. Simion, E. S. Abrutyn, Z. D. Draelos, *J. Cosmet. Sci.*, 56, (2005).
5. J. L. Leyden, A. V. Rawlings, *Skin Moisturization*, Marcel Dekker, New York, 2002, chapter 6.
6. Z. D. Draelos, *Cosmetic Dermatology-Products and Procedures*, Wiley, New York, 2010, chapter 35.
7. M. P. Lupo, *Clin.Dermatol.*, 19, 2001.
8. A. O. Barel, M. Paye, H. I. Maibach, *Handbook of Cosmetic Science and Technology*, Marcel Dekker, New York, 2001, chapter 1.

RAMAN IMAGING OF DENTAL FOLLICLE MESENCHYMAL STEM CELLS

LOREDANA F. LEOPOLD¹, CRISTINA COMAN¹, ISTVAN SZ. TODOR²,
LASZLO SZABO², OLGA SORIȚĂU³, PIROSKA VIRAG³, CARMEN M. MIHU⁴,
VLAD MOISOIU^{2,4*}, NICOLAE LEOPOLD²

ABSTRACT. Raman spectroscopy is slowly but surely becoming an important investigative method in cellular samples. In this study, the potential of Raman mapping was assessed on dental follicle mesenchymal stem cells (MSCs). Raman spectra were recorded with the 532 nm laser line at $\sim 1 \mu\text{m}$ spatial resolution. Principal Component Analysis (PCA) of the recorded Raman spectra provided false color Raman maps, evidencing cellular components such as the nucleus, nucleolus, endoplasmic reticulum and cytoplasmic RNA. A high concentration of this last component can be considered as a universal marker for stem cells. Given that stem cells are in a state where they are always ready to undergo transcription, a large concentration of RNA is found in the cytoplasm of these cells, as they rapidly need to produce proteins that specialize the cell during differentiation.

Keywords: Raman mapping, principal component analysis, dental follicle mesenchymal stem cells, DNA, RNA

INTRODUCTION

Raman mapping (or Raman scanning) is a function of Raman spectroscopy in which the laser spot travels through the investigated sample and acquires a

¹ Faculty of Food Science and Technology, University of Agricultural Sciences and Veterinary Medicine, Mănăştur 3-5, 400372 Cluj-Napoca, Romania.

² Faculty of Physics, Babeş-Bolyai University, Kogălniceanu 1, 400084 Cluj-Napoca, Romania.

³ Radiotherapy, Tumor and Radiobiology Laboratory, The Oncology Institute "Prof. Dr. Ion Chiricuță", Cluj-Napoca, Romania.

⁴ Department of Histology, Iuliu Hațieganu University of Medicine and Pharmacy, Victor Babeş 8, 400012 Cluj-Napoca, Romania

* Corresponding author e-mail: vlad.moisoiu@gmail.com

spectrum at set intervals. The end result of Raman mapping is an image of the scanned object that has highly precise structural information. The difference between Raman spectroscopy and Raman mapping is that singular Raman spectra only provides concrete chemical information at distinct positions within the sample while Raman imaging provides chemical information coupled with spatial information [1].

There are already many studies that focus on the acquisition of standard Raman point spectra and they provide an important basis on future imaging studies. These existing spectroscopic studies have already assigned the important spectral components for a great number of cells types and they provide a background of knowledge that Raman imaging can take advantage of. The dimensionality gained from Raman imaging takes Raman spectroscopy to new heights as a spectroscopic method, as it offers it the ability to investigate dynamic changes within the cell with a high spatial accuracy and a remarkable specificity [1-3].

Several Raman studies focused on different aspects of stem cell development have been already published. Notingher et al. have investigated the differentiation of both murine embryonic stem cells, as well as mouse neural stem cells. The translation of mRNA was monitored by quantifying both, the peak corresponding to the RNA backbone at 813 cm^{-1} and the phenylalanine peak at 1005 cm^{-1} , which is an indicator of proteins [4]. These studies have shown an easily distinguishable method of detecting cytoplasmic RNA, without interference from DNA, based solely on the peak at 813 cm^{-1} .

Ghita et al. have worked extensively on imaging stem cells through Raman spectroscopy [5]. The Raman band at 813 cm^{-1} , which corresponds to the O-P-O vibration of the RNA phosphate backbone, has been shown to be a good indicator of the differentiation state of the cells, and as such has allowed the fast detection of stem cell derived glial cells from stem cells. Neural stem cells have a high concentration of tRNA in the cytoplasm, unlike glial cells, and this has been shown to be a good distinguishing factor between the two types of cells.

Konorov et al used the DNA band at 783 cm^{-1} from a large number of nuclei in order to acquire information about the cell cycle of human embryonic stem cells [6]. Through this method, they were able to determine the state of division of human embryonic stem cells by quantifying the corresponding DNA and RNA peaks from the Raman spectra. As such, the intensity of the band at 783 cm^{-1} proved to be a good identifier of cell phase.

Another purely spectroscopic study on stem cells was performed by Tan et al., showing that spectra of human induced pluripotent stem cells are very similar to spectra of human embryonic stem cells, whilst at the same time being distinguishably different from spectra of differentiated human embryonic stem

cells [7]. The PCA discrimination method that they employed showed a clear divide between the differentiated and undifferentiated cells, which could be mainly attributed to the reduced protein to nucleic acid ratio within the differentiated cells. The authors have stated that proper Raman imaging has to be employed in order to obtain a more complete overview of the cells.

These preliminary studies show that Raman spectroscopy has the potential to become a leading method in the investigation of stem cells as it provides accurate, highly specific results, a great resolution and, more importantly, it is non-invasive to the cell. Therefore, Raman investigated cells can still be used in biomedical applications afterwards and, as such, Raman might be the ideal discriminating method between usable stem cells and unusable differentiated cells, on a per application basis.

Even with these important advantages, Raman imaging studies on stem cells are still not widespread and only a few groups are focusing on this function of Raman spectroscopy when regarding stem cell research.

Some of the most studied stem cells are hematopoietic and mesenchymal lineages as they are commonly used for bone marrow transplantation. Mesenchymal stem cells (MSCs), are pluripotent stromal cells that can differentiate into a variety of cell types, including osteoblasts (bone cells), chondrocytes (cartilage cells), myocytes (muscle cells) and adipocytes (fat cells). Recently, the presence of mesenchymal stem cells was detected in dental tissues (dental pulp, periodontal ligament, and dental follicle) [8]. The dental follicle is a loose connective tissue surrounding the developing tooth. Dental follicle stem cells could therefore become a safe and cheap source of MSCs. As dental follicle is present in impacted, extracted and disposed of teeth, which are regarded as medical waste in dental practice, dental follicle stem cells can be isolated and grown under defined tissue culture conditions.

In this study we assess the potential of Raman mapping on dental follicle MSCs. The obtained Raman maps show different cellular components, and most importantly, a high concentration of cytoplasmic RNA, an indicator for undifferentiated stem cells.

EXPERIMENTAL

Cell culture. Briefly, dental follicle mesenchymal stem cells were cultured in standard stem cell medium DMEM, 4.5 g/l glucose/F12-HAM, 15% FBS (Fetal Bovine Serum), 100 U/ml penicillin-100 µg/ml streptomycin, 2 mM L-glutamin, 1% NEA (Non-Essential Aminoacids), 1 mM sodium piruvate, 55 µM β-mercaptoetanol (Sigma, UK). Prior to Raman measurements, the cells were fixed on 15 mm diameter, 1 mm thick MgF₂ plates with 4% ice-cold paraformaldehyde and stored at 4°C until analysis.

Raman microspectroscopy measurements. For Raman measurements, a Raman microspectrometer (InVia, Renishaw) was used. The instrument was based on a upright microscope (Leica) with a 60×/NA 0.90 water-immersion objective (Olympus), a 532 nm, 150 mW diode laser, a spectrometer equipped with a 1800 lines/mm grating, CCD detector and an automated step-motor stage. The instrument was calibrated prior to each experiment using an internal standard silicon sample, and the spectral resolution in the 220–1970 cm^{-1} region was $\sim 4 \text{ cm}^{-1}$. The Raman map was obtained by raster-scanning an area comprising 21x31 points on the cell surface, through the laser focus in $\sim 1 \mu\text{m}$ steps. The exposure time for each spectrum was 5 s. A total number of 651 spectra were recorded. Spectra preprocessing consisted of cosmic ray removal.

RESULTS AND DISCUSSION

The optical microscopy image of a typical dental follicle mesenchymal stem cell (MSC), obtained with the 60x objective is displayed in Fig. 1. Optical images were recorded before and after the Raman mapping process, which provided us with the certitude that the cell was not damaged after laser illumination during mapping.



Fig. 1. Microscopic image of a dental follicle mesenchymal stem cell.

Raman mapping at a $\sim 1 \mu\text{m}$ spatial resolution was performed by using a 532 nm laser line. The literature mentions the preponderant use of the 785 and 532 nm laser lines for cellular mapping [1-3]. Both laser lines show certain advantages and disadvantages, thus choosing the proper laser wavelength remains an option of the operator, depending on the type of cellular probe. If

excitation at 532 nm causes strong fluorescence for a sample, the 785 nm line is a good alternative, as its lower energy photons should overcome this inconvenience. As the intensity of Raman scattering increases with the fourth power of the frequency of the exciting radiation, the intensity of the Raman inelastic scattered photons will be higher with a 532 nm excitation than with a 785 nm excitation. Moreover, regular CCD detectors have a maximum efficiency of detection within the 500-600 nm spectral region, which also coincides with the maximum efficiency of transmittance for most objectives.

In our study, we used the 532 nm laser excitation line in order to maximize the above mentioned parameters especially due to the fact that no fluorescence was observed when exciting with this laser line.

Analyzing the recorded Raman raw spectra, some bands can be assigned by visual inspection, but the main information can be accessed only after noise and redundant information reduction and enhancement of the information rich signal by PCA. PCA provides a certain number of false color score plots and the corresponding loadings plot. In order to decide which of the score plots provide relevant information, the loadings plot has to be evaluated in order to find positive or negative peaks which can be assigned to cellular components.

Fig. 2 shows the scores and loadings plot of the first principal component (PC1).

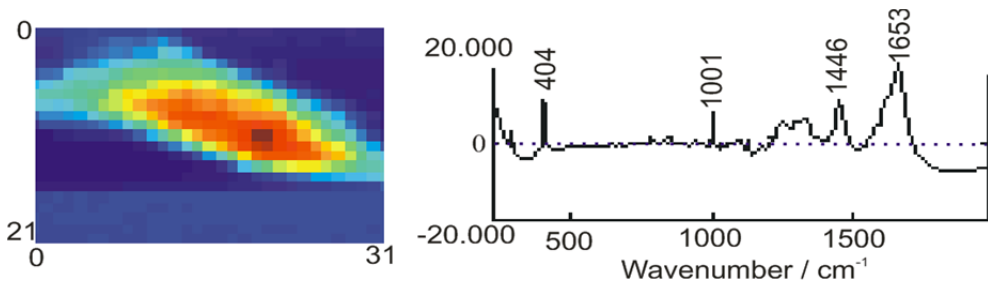


Fig. 2. Scores plot and loadings plot of PC1.

The positive bands from the loadings plot of PC1 can be assigned to bands that are present in all analyzed points during the Raman mapping: 404 cm^{-1} from the MgF_2 substrate, 1001 cm^{-1} due to ring stretching of phenylalanine aromatic amino acid, 1446 cm^{-1} due to C-H bending vibration and 1653 cm^{-1} due to water and amide I band. Given that PC1 contains contributions from both phenylalanine stretching and C-H bending, it is fair to assume that it may provide a good indication of cellular volume, as recently shown by Boitor et al. in an AFM-Raman study [9]. However, no distinct structural information can be extracted from PC1.

Cellular structural information can be first extracted from PC4. Fig. 3 shows the scores plot of PC4, depicting the nucleus (blue) and endoplasmic reticulum (red), as can be deduced from the loadings plot of PC4.

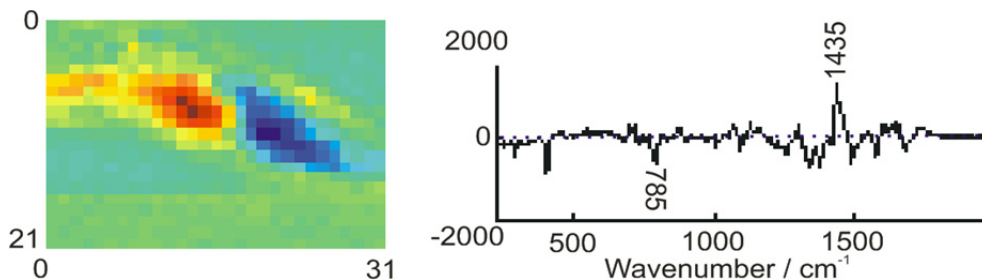


Fig. 3. Scores plot and loadings plot of PC4.

The loadings plot shows positive and negative peaks, with corresponding false colors: red for positive peaks and blue for negative peaks. The negative peak at 785 cm^{-1} , can be considered representative for the negative part of the loadings plot of PC4, being assigned to the stretching vibration of the O-P-O bond, which can be found in the DNA backbone. As such, this peak is a great indicator of DNA, and can be used as an extremely accurate method of pinpointing the nucleus, the main part of cellular DNA being stored in this component. Given that the peak is below the zero line within the PC, the nucleus is represented by the color blue (which sits at the bottom of the color scale) in the PC4 image.

The PC4 image also shows another main component that is inversely proportional to the DNA peak. This red region expresses an intense peak at 1435 cm^{-1} , which usually represents the same vibration that contributes to the peak at 1446 cm^{-1} (Fig. 2) but is shifted to a lower wavenumber because of the specific bonds the CH_2 molecule makes within lipids. Given that the endoplasmic reticulum is strongly involved in the synthesis of lipids, it is highly apparent that the region highlighted in red is in fact the endoplasmic reticulum [10]. The spectral component of this region is inversely correlated to the spectral component of the DNA, and is therefore represented by the color red, which sits at the top of the color scale.

This PC only has one defining characteristic, which is the peak at 813 cm^{-1} . This peak is important as it is the main indicator of undifferentiated MSCs. This peak appears as a result of the stretching vibration of the O-P-O bond within the RNA backbone, the same vibration that causes the appearance of the 785 cm^{-1} of the DNA, but is shifted to a higher wavenumber because of the single stranded nature of RNA, as opposed to DNA.

The last and most important PC of the ones built from the MSC Raman spectra is PC6 (Fig. 4).

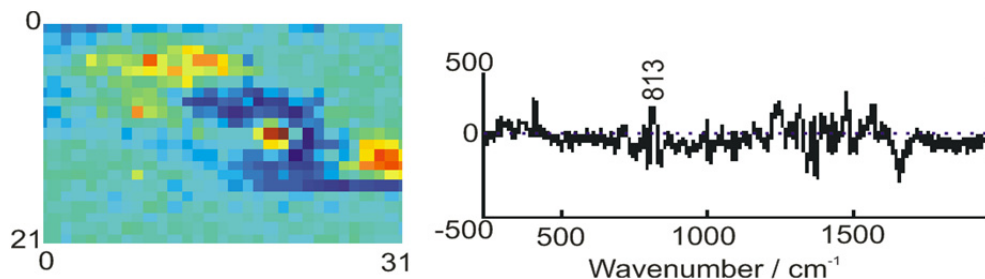


Fig. 4. Scores plot and loadings plot of PC6.

The PC6 scores plot from Fig. 4 shows the cytoplasmic RNA highlighted in red and yellow, but also an intense red point which can be distinguished in a region which was assigned to the cellular nucleus in PC4 (Fig. 3). This point is most likely indicative of the cellular nucleolus, whose one main component is RNA. Given that stem cells are in a state where they are always ready to undergo transcription, a large concentration of RNA is found in the cytoplasm of these cells, as they rapidly need to produce proteins that specialize the cell during differentiation.

As cells that are already differentiated do not present such an intensive transcription process, the concentration of cytoplasmic RNA is obviously lower, below the detection limit of conventional Raman spectrometers.

CONCLUSIONS

Raman mapping is a technique that is capable to provide spectacular results as it combines both spatial and spectral information. The Raman maps obtained from dental follicle MSCs show various cellular components represented in false colors as a function of their respective PCA scores. The most important investigated cellular component was the high, detectable concentration of cytoplasmic RNA, which is an accurate indicator of undifferentiated MSCs. Thus, we believe that Raman spectroscopy has the potential to become a leading method in the investigation of stem cells as it provides accurate, highly specific results, with a good spatial resolution and, more importantly, in a non-invasive manner. Therefore, Raman investigated cells can still be used in biomedical applications after their identification and, as such, Raman is the ideal discriminating method between usable stem cells and unusable differentiated cells, on a per application basis.

ACKNOWLEDGMENTS

LFL and CC highly acknowledge support from PN-II-RU-TE-2014-4-2211 project; ISzT, LSz and NL highly acknowledge support from PN-II-RU-TE-2012-3-0227 project; VM acknowledges a fellowship of the Romanian Ministry of Education UEFISCDI PN-II-RU-BT-2013-1 project number 8/01.04.2014; Ms. Agota E. Kacso is highly acknowledged for her programming support. Dental follicle stem cells were a gift from Dr. Ondine Lucaciu. The Raman measurements in this study were conducted using the Babeş-Bolyai University research infrastructure financed by the Romanian Government through the programme PN II – Capacities, project title Integrated Network for Interdisciplinary Research (INIR).

REFERENCES

1. B. Kann, H.L. Offerhaus, M. Windbergs, C. Otto, *Adv. Drug Delivery Rev.*, 89, 71 (2015).
2. K. Kong, C. Kendall, N. Stone, I. Notingher, *Adv. Drug Delivery Rev.*, 89, 121 (2015).
3. S.F. El-Mashtoly, H.K. Yosef, D. Petersen, L. Mavarani, A. Maghnouj, S. Hahn, C. Kötting, K. Gerwert, *Anal. Chem.*, 87, 7297 (2015).
4. I. Notingher, I. Bisson, J.M. Polak, L.L. Hench, *Vib. Spectrosc.*, 35, 199 (2004).
5. A. Ghita, F.C. Pascut, M. Mather, V. Sottile, I. Notingher, *Anal. Chem.*, 84, 3155 (2012).
6. S.O. Konorov, H.G. Schulze, J.M. Piret, M.W. Blades, R.F.B. Turner, *Anal. Chem.*, 85, 8996 (2013).
7. Y. Tan, S.O. Konorov, H.G. Schulze, J.M. Piret, M.W. Blades, R.F.B. Turner, *Analyst*, 137, 4509 (2012).
8. S. Gronthos, M. Mankani, J. Brahim, P.G. Robey, S. Shi, *Proc. Natl. Acad. Sci. U.S.A.*, 97, 13625 (2000).
9. R. Boitor, F. Sinjab, S. Strohbuecker, V. Sottile, I. Notingher, *Faraday Discuss.*, 2015, DOI: 10.1039/C5FD00172B
10. P. Fagone, S. Jackowski, *J. Lipid Res.*, 50, S311 (2009).

EXPERIMENTAL AND FINITE ELEMENT ANALYSIS REGARDING THE INFLUENCE OF FRICTION CONDITIONS ON MATERIAL FLOW IN METAL FORMING PROCESSES

M. POP^{1*}, D. FRUNZA¹

ABSTRACT. When friction occurs between tool and workpiece, surface expansion and high normal pressure between work piece and die, leads to adhesions(cold-weld), abrasion of die and work material. To reduce the friction, it requires a suitable lubricant. In the present work different lubricated condition were tested in the extrusion process of lead. The influence of lubricated conditions on the material flow and process parameters were determined. Experimental values were compared with simulation.

Keywords: friction, plastic deformation, simulations.

INTRODUCTION

One of the most important considerations in optimizing metal forming processes is the friction between the workpiece and forming tools. Material flow is directly linked to the frictional conditions, and this in turn influences the required forming load and the mechanical properties of the final product. Other aspects of product quality, such as surface finish and dimensional accuracy are also affected by the friction condition. In addition, tool design, tool life, and productivity depend on the ability to determine and control friction.

In forging, the flow of metal is caused by the pressure transmitted from the dies to the deforming workpiece. Therefore, the frictional conditions at the die/workpiece interface greatly influence metal flow, formation of surface and internal defects, stresses acting on the dies, and load and energy requirements [1]. Also in metal forming, friction is a crucial factor that determines whether an

¹ Technical University of Cluj-Napoca, 103-105 Muncii Avenue, 400641 Cluj-Napoca, Romania.

* Corresponding author e-mail: mariana.pop@ipm.utcluj.ro

industrial process can be run with acceptable, economic result. In many forming applications, the actual friction conditions are not sufficiently known. The friction phenomenon in metal forming is of great importance. Various reasons for this are: forming loads and stresses transferred to the dies depend on friction and can be reduced by use of appropriate lubricants; the surface quality of the formed workpiece depends on the lubricant used; wear of the dies can be reduced if lubricant films are applied, which provide reduced friction, or even full or partial separation, between the die and the workpiece during forming. Major factors affecting friction include the normal stress along the die–material interface, the lubrication condition, the relative velocity, the temperature, the roughness, and the mechanical properties of the material and/or the die. A detailed investigation of these factors is not easy because the die–material interface in metal forming is under high pressure and temperature [2].

THEORETICAL DETAILS

No surface is geometrically perfect. Surfaces contain irregularities that form peaks and valleys. Thus, contact between the die and the workpiece is maintained over limited portions of the apparent interface. The apparent area of contact is the total area, but the actual area of contact is limited to that between the peaks of the opposing asperities (Fig. 1).

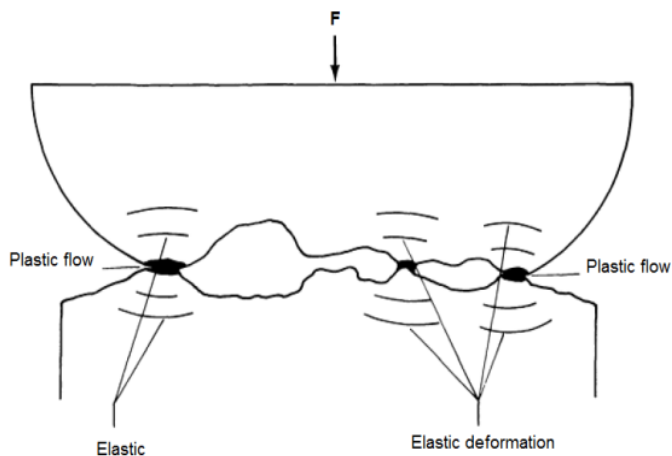


Fig.1. Representation of surface irregularities [3].

Figure 2 illustrates this fundamental phenomenon as it applies to the upsetting of a cylindrical workpiece. As figure shows, under frictionless conditions, the workpiece deforms uniformly and the resulting normal stress, σ_n , is constant across the diameter.

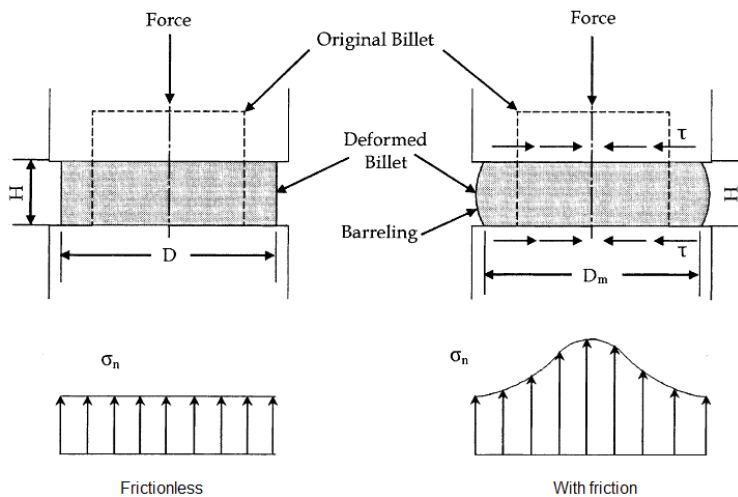


Fig.2. Upsetting of cylindrical workpiece [1].

Where some level of frictional stress is present, the deformation of the workpiece is not uniform (i.e., barreling).

As a result, the normal stress, σ_n , increases from the outer diameter to the center of the workpiece and the total upsetting force is greater than for the frictionless conditions [1].

Excessive friction leads to heat generation, wear, pick-up and galling of the tool surface, which contribute to the premature failure of the tools. Friction can increase the inhomogeneity of deformation, leading to defects in the finished products. In order to reduce the detrimental effects of friction, lubricants are used extensively. Nevertheless, it should be noted that it is not always the practice to reduce the interfacial friction to a minimum value.

In order to evaluate the performances of various lubricants under various material and process conditions and to be able to predict forming pressures, it is necessary to express the interface friction quantitatively. There are two laws that can be utilized for this purpose: Coulomb and Tresca. The Coulomb friction law

uses a coefficient of friction, μ , to quantify the interface friction. Equation 1 shows that μ is simply the ratio of the frictional shear stress, τ , and the normal stress (pressure), σ_n .

$$\tau = \sigma_n \mu \quad (1)$$

At high contact pressures instead of the Coulomb friction model, it is recommended to use the Tresca model. Tresca proposed a different friction model, which is able to describe the physics of the friction at an interface at high contact pressures. *Tresca's friction model* is commonly expressed as:

$$\tau = f\bar{\sigma} = \frac{m}{\sqrt{3}}\bar{\sigma} = mk \quad (2)$$

The interface shear friction law uses a friction factor, f , or a shear factor, m , to quantify the interface friction. Equation 2 shows that the frictional shear stress, τ , is dependent on the flow stress of the deforming material, $\bar{\sigma}$, and the friction factor, f , or the shear factor, m .

The parameter m is called the friction factor, and can vary in the range $0 < m < 1$. In the case of sticking between workpiece material and the die, this factor equals 1, and the friction shear stress transferred through the interface equals the shear flow stress of the softer contact body, so that the situation agrees with the physics of the interface. In metal forming simulations, friction has traditionally been assumed to follow the Coulomb friction and the constant shear friction [2,4,5,6,7].

The finite element analysis (FEA) based simulation of metal forming processes has been widely used to predict metal flow and to optimize the manufacturing operations.

Friction during extrusion can lead to the development of tensile stresses at the surface of heterogeneous alloys. Thus, lubrication is often required, although in some cases, hot extrusion is done without lubrication (especially for aluminum alloys). Of all bulk deformation processes, extrusion is perhaps the most sensitive to lubrication, partly because the non-steady-state conditions at the beginning and end of extrusion are conducive to instabilities, and partly because any unwanted change in lubrication leads to defects that affect not only the appearance but also the properties and integrity of the product [8]. In forward extrusion, the material is pushed through the container and the die by means of the ram (Fig.3).

The aim of this paper is to present by using numerical simulation the influence of friction condition on deformation parameters in direct extrusion.

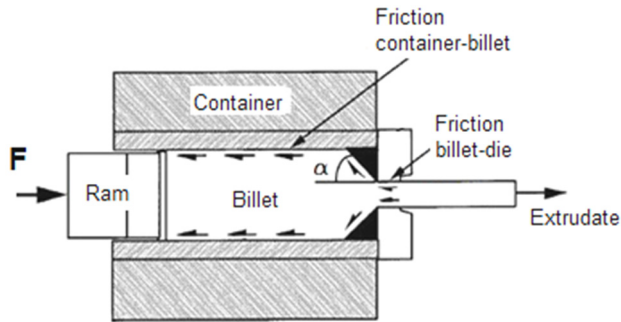


Fig.3. Principle of direct extrusion.

RESULTS AND DISCUSSION

The lead (Pb99,5) samples were used to study the influence of lubrication conditions of the process on the extrusion force and material flow pattern. The cast lead alloys of dimensions 60mm in diameter produced were machined into smaller lead alloy specimens of dimensions 30 mm in diameter and 20 mm in height. The billets were subjected to upsetting tests on Heckert type hydraulic press with maximum force of 200KN. The ram speed during the tests were 0,5mm/s. The assembly ram-billet-die is presented in figure 4.

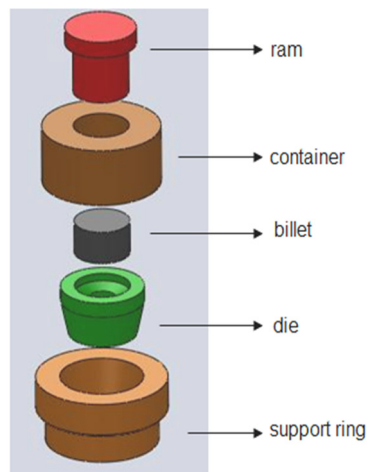


Fig.4. Assembly ram-billet-die.

The geometry of the dies generated in SolidWorks are presented in figure 5.

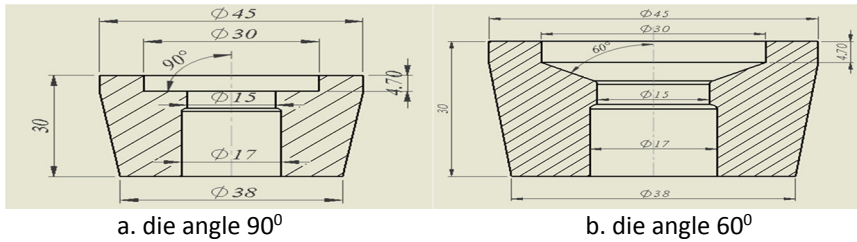
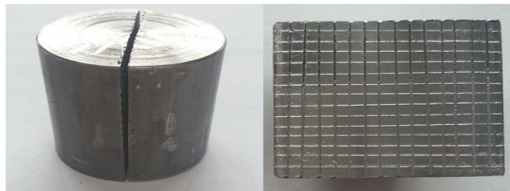


Fig.5. Geometry of the dies.

Figures 6 and 7 presents the shape of the flow lines in the extruded material function of die angle and lubrication conditions.



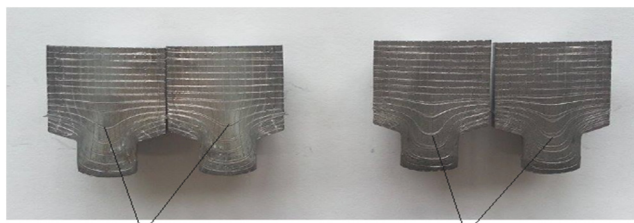
Initial sample



a. Dead zone

b. Shape of flow lines

Fig. 6. Extruded samples on die with 90° angle
a. unlubricated; b. lubricated with mineral oil.



a. Shape of flow lines

b. Shape of flow lines

Fig. 7. Extruded samples on die with 60° angle
a. unlubricated; b. lubricated with mineral oil.

The extrusion load, F , using a modified upper bound equation is given by the following expression [9].

$$F_d = 2k \left[4\mu \left(\frac{H}{D} + \frac{h}{d} \right) + \left(\frac{\mu}{\sin \alpha} + 1 \right) \ln \frac{D^2}{d^2} \right] \frac{\pi D^2}{4} \quad (3)$$

where μ is the coefficient of friction at die/billet interface, D the billet diameter (mm); d the die land diameter (mm), h the die land height (mm), α the die half angle ($^\circ$), H the billet height (mm) and k is the maximum tangential stress at die-billet interface (N/mm²).

The simulation program FORGE is based on the finite element method for cold and hot metal forming. It enables the thermo-mechanical simulation of the plastic deformation processes of metals in an axisymmetric, homogeneous and isotropic state of deformation and obeys the von Mises criterion. The calculations of the metal flow, stress field, strain, strain rate and temperature are conducted on the assumption of the viscoplastic model of the deformed body.

The geometries of the billet, die, container and ram were generated in SolidWorks and the meshes within their space domains in FORGE 3D. The physical properties of the aluminium alloy used in the computer simulation are given in Table 1. The billet was considered thermo-viscoplastic while the tools rigid, and both of these material models neglected the elastic deformation. The shear-type friction conditions at the workpiece and tooling interfaces were imposed as part of the boundary conditions.

Table 1.

Properties	Material Lead
Density (g/cm ³)	11,34
Heat capacity (J/g °C)	2,39
Thermal conductivity (W/m°C)	35
Emissivity	0,08

The process parameters used in the simulations are given in Table 2.

Table 2.

Billet height [mm]	30
Billet diameter [mm]	30
Die semi angle α [$^\circ$]	60,90

Extrusion ratio	2
Billet temperature [°C]	20
Container and die temperature [°C]	20
Ram speed [mm/s]	0,5
Friction factor at the workpiece–die interface	0,1; 0,3

Fig. 8 shows the initial meshes of the billet and the tooling, together with a cross-section cutting through the die.

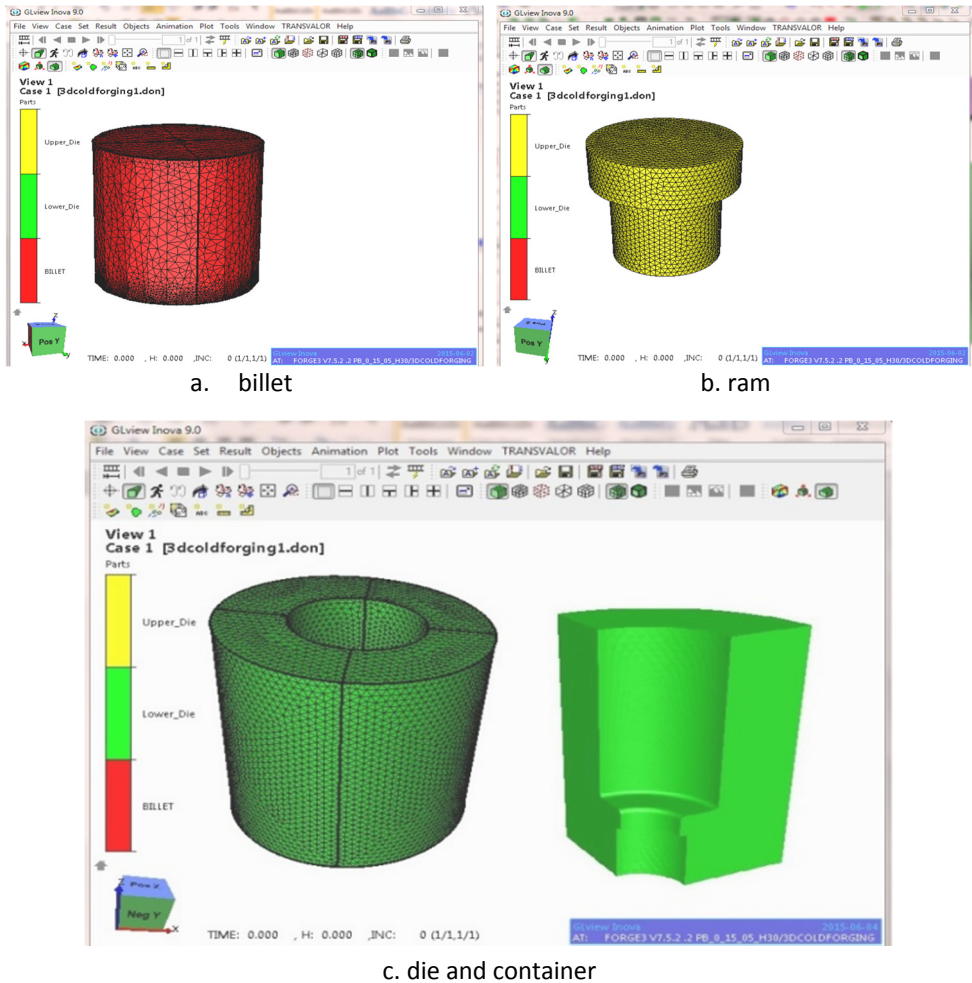


Fig.8. Initial meshes of the billet, container, die and ram and the cross-section of the die.

SIMULATION RESULTS

The results obtained for effective strain, equivalent von Mises stress, extrusion force and friction power distribution in different extrusion conditions are presented in figures below.

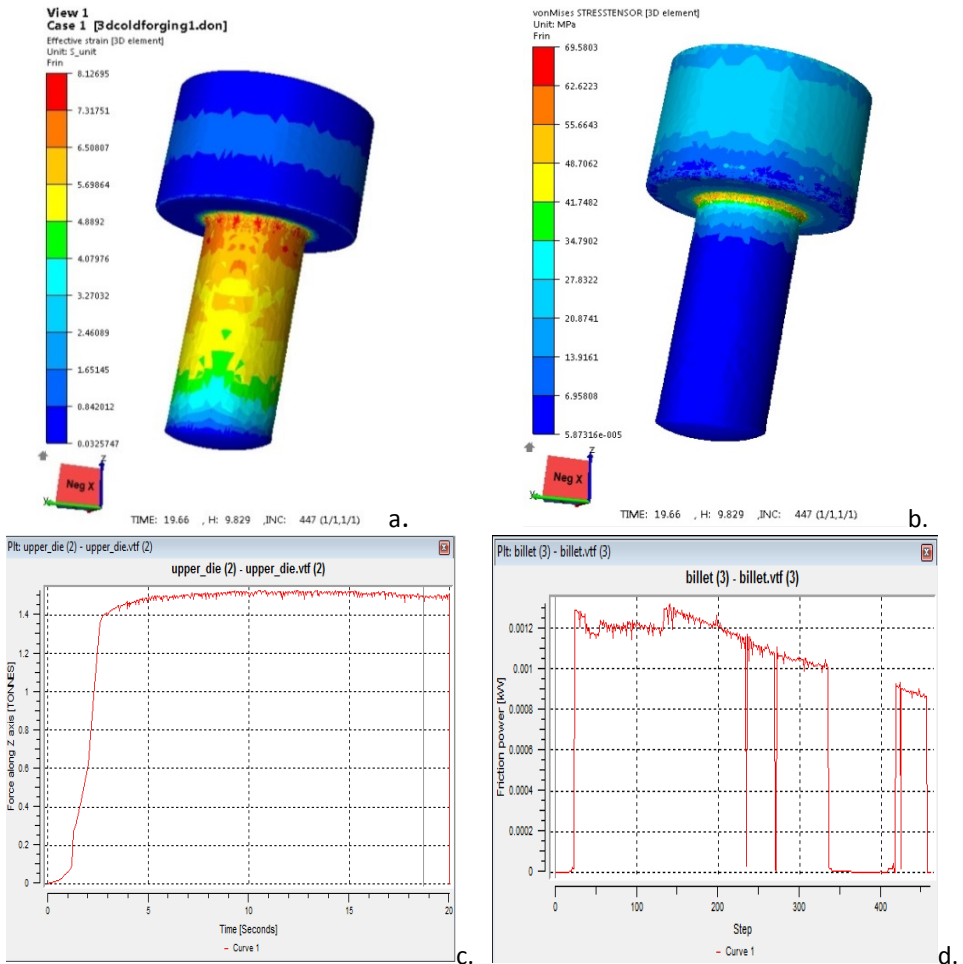


Fig.9. Deformation parameters for die angle 90° in unlubricated condition
 a. effective strain; b. von Mises stress; c. force; d. friction power.

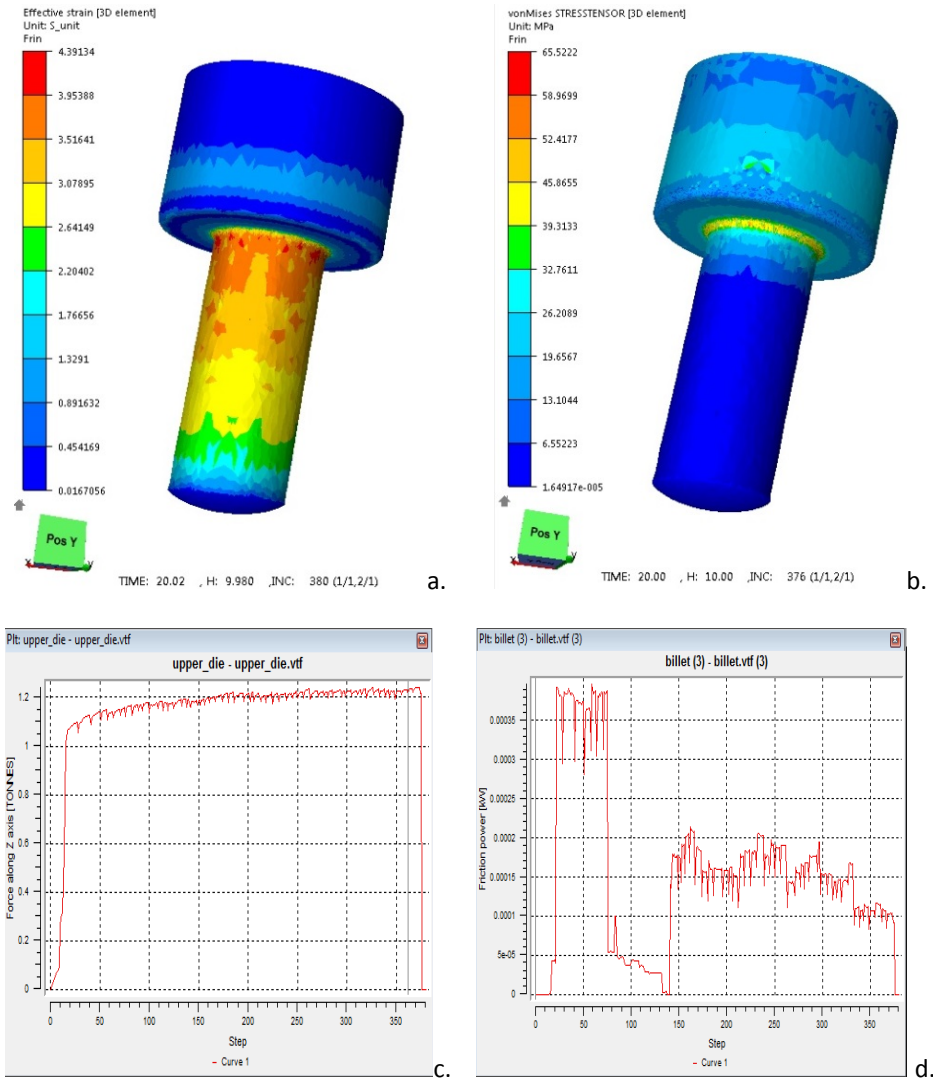


Fig.10. Deformation parameters for die angle 90° in lubricated condition
 a. effective strain; b. von Mises stress; c. force; d. friction power.

Lubrication plays an important role in cold extrusion process since good lubricants prevent direct metallic contact, with the reduction of extrusion load and the improvement of product quality and tool life.

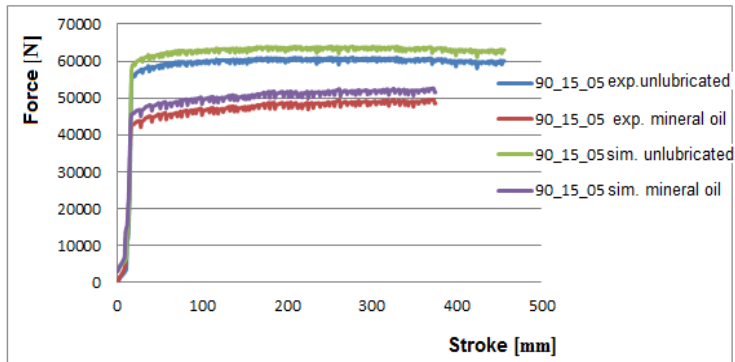


Fig.11. Experimental and simulated force distribution for die angle 90° , in unlubricated and lubricated condition.

The forward extrusion process was carried out on 99,5 lead with unlubricated and lubricated with mineral oil. The experimental study was conducted to highlight the importance coefficient of friction of plastic deformation processes. Coefficient of friction in the processes of plastic deformation depends on many factors such as: the angle of the die, lubrication conditions, forming speed, the geometry of the tool. To highlight the friction coefficient, measurements were performed on a particular method of forming namely by cold extrusion deformation under certain conditions and with different die angles.

The first measurements took place on a die with an angle of 90° unlubricated, highlighting the flow of the material. The right angle causes the material to flow more unfavorable and the presence of the dead zones namely that the material in this area does not flow and friction between the billet and the die is high. Because of the obstruction caused by the sharp corner of the die, material flow through this area it is visible from the heavily distorted form of the discretized network. The surface of the discretized network elements is different in the area of contact with the walls of the die than in the central portion of the sample, suggesting a non-uniform distribution of the deformation. Due to the friction between the preform and the container material tends to flow more rapidly into the material than on the surface

CONCLUSIONS

The force required for the extrusion process is greater if the case of die with angle 90° and lower extrusion force required if case of mineral oil lubrication.

In the extrusion with 60° die angle both in unlubricated and lubricated states the forces are lower than in extrusion with 90° angle of die.

The flow of material in this case is greatly influenced by the angle of the die and the friction is reduced for mineral oil lubrication.

Comparisons were made for the experimental extrusion load with simulated extrusion load. It is found that for all conditions, experimental extrusion load is minimum, simulated extrusion load is maximum.

The average error between the experimental and simulation is below 10%.

The close agreement between the simulation results confirms the validity of the extrusion for evaluating conditions.

REFERENCES

1. Altan, T., Ngaile, G., Shen, G., Cold and hot forging, Fundamentals and applications, ASM International, 2004;
2. M.S. Joun, H.G. Moon, I.S. Cho, M.C. Lee, B.Y. Jun, Effects of friction laws on metal forming processes, Tribology International 42 (2009) 311–319;
3. Friction, lubrication and wear technology, ASM Handbook, vol. 18;
4. Zienkiewicz O.C., Jain P.C., Onate E., Flow of solids during forming and extrusion: some aspects of numerical solutions, Int J. Solids Struct 1978; 14:15–38;
5. Hirai T., Ishise T., Plastic metal flow under frictional boundary in forward extrusion die and stress distribution of the die, Int. J. Mach Tool Des Res 1986; 26:217–29;
6. Coupez T., Soyris N., Chenot J.L., 3-d finite element modeling of the forging process with automatic remeshing. J Mater Proc Technol 1991; 27: 119–33;
7. Oh S.I., Wu W.T., Tang J.P. Simulations of cold forging processes by the DEFORM system. J Mater Proc Technol 1992; 35:357–70;
8. ASM International, Handbook of Workability and Process Design, Ed. by George E. Dieter, Howard A. Kuhn, S. Lee Semiatin, 2003;
9. Dragan I., Tehnology of Plastic Deformation, EDP, Bucharest, Romania, 1981.

SYNTHESIS, STRUCTURAL CHARACTERIZATION AND *IN VITRO* EVALUATION OF BIOACTIVITY OF SILVER CONTAINING BIOACTIVE GLASSES

R. A. POPESCU^{1,2}, K. MAGYARI¹, I. PAPUC², L. BAIA^{1*}

ABSTRACT. Five silver doped SiO₂–CaO–P₂O₅ based bioactive glasses were synthesized and structurally characterized in order to find the optimal concentration that can be further used in scaffold fabrication for bone tissue engineering. Initially, the recorded XRD patterns confirmed the existence of a preponderantly amorphous structure for all samples, though the presence of some crystallization centres associated with tricalcium phosphate phase was also revealed. The UV-vis spectra evidenced signal originated from the surface plasmon resonances of the silver nanoparticles. The signature of both types of isolated and cluster silver nanoparticles were signalized, the amount of the silver aggregates was found to progressively increase starting with 0.5 mol% Ag₂O. Bioactivity assessment was also performed for the obtained samples, and it was determined a good response to all compositions. However, for the sample with 0.5 mol% Ag₂O the content of the self-assembled hydroxyapatite phases was more noticeable and also was taken into consideration the absence of a high signal from AgCl. This can be considered the optimum concentration of silver, from the obtained samples range, that can be further used for scaffold preparation.

Keywords: XRD, Uv-Vis, bioactivity, silver.

INTRODUCTION

In the last years, substantial growth has been reported in the area of biomaterials used for tissue reconstruction [1]. A large attention was captured by some bioactive ceramics used as artificial bone grafts, because of their properties

¹ Faculty of Physics & Interdisciplinary Research Institute on Bio-Nano-Sciences, Babes-Bolyai University, 400084 Cluj-Napoca, Romania.

² Faculty of Veterinary Medicine, University of Agricultural Science and Veterinary Medicine, 400372 Cluj-Napoca, Romania.

* Corresponding author e-mail: lucian.baia@phys.ubbcluj.ro

to form *in vivo* a bone-like apatite layer able to promote the osteoformation [2, 3]. An important feature is their ability to improve revascularization, osteoblast adhesion, enzyme activity, and differentiation of mesenchymal stem cells [4, 5].

This is a domain of intense research, which is distinctly manifested in the rising number of publications in the field of bioactive glasses, their attributes and applications [4, 6]. There are two principal ways to prepare bioactive glasses, namely, the melt quenching method and sol-gel one [7]. Sol-gel derived bioactive glasses are produced by the hydrolysis of organic precursors followed by the polycondensation. Finally the gel is heat treated to form a glass and to remove the organic part [7, 8].

Silver is recognized as an antiseptic agent that was frequently used in diverse implant materials such as bioactive glasses, metallic alloys and polymers [9, 10]. It should be noted that there was no observed cytotoxicity effect for animal cells when silver ion concentrations released were lower than 1.6 mg/L [10-12].

Bioactive glasses containing Ag₂O are attractive materials because they combine antibacterial effect of silver with the glass bioactivity [13, 14]. It is well known that silver ions have positive effect against microbial threat, being very efficient in small quantities [15]. A number of studies revealed that the addition of Ag₂O into bioactive glass decreases the probability of bacterial contamination and does not negatively affect the glass matrix bioactivity [16, 17].

The aim of this study was to produce a wide range of bioactive glasses containing silver, to characterize them and to find the optimal concentration that can be further used in scaffold fabrication for bone tissue engineering. In this regard was made also a bioactivity test to sustain and improve the previously obtained results [18].

EXPERIMENTAL

Synthesis of the glass

The samples belonging to the 60SiO₂·(32-x)CaO·8P₂O₅·xAg₂O (mol%) system with x=0; 0.5; 1; 1.5; 2 and 2.5, were prepared by sol-gel method. The precursors used were tetraethyl orthosilicate (TEOS), triethyl phosphate (TEP), calcium nitrate tetrahydrate (Ca(NO₃)₂·4H₂O) and silver nitrate (AgNO₃) hydrolyzed in the presence of nitric acid; the (HNO₃+H₂O)/(TEOS+TEP) molar ratio was equal to 8. Reactants were added consecutively after 1-hour intervals, under continuous stirring. The solutions (*sols*) were poured into closed containers that were kept at 37°C until gelation (*gels*) was reached (1-2 days). The resultant gels were aged at 37°C for 2 days and it were dried at 120°C for 24 h.

Material stabilization was carried out at 600°C for 3 hours. This temperature was determined by differential thermal analysis of the dried gels. Prior characterization the obtained glass was milled.

Methods

X-ray Diffraction

The X-ray diffraction analysis (XRD) was carried out on a Shimadzu XRD 6000 diffractometer using CuK α radiation ($\lambda=1.54$ Å), with Ni-filter. The diffractograms were recorded in 2θ range from 10° to 80° with a speed of 2°/min.

UV-vis Spectroscopy

Absorption measurements of the samples were performed with an Analytic Jena Specord 250 plus UV-Vis spectrometer. The spectral resolution was of 2 nm.

FT-IR Spectroscopy

The FT-IR absorption spectra were recorded with a JASCO 6200 (Jasco, Tokyo, Japan) spectrometer, at room temperature, in the 400–4000 cm⁻¹ range with a spectral resolution of 4 cm⁻¹ and using the well-known KBr pellet technique. The recorded spectra were smoothed by a 5-point Savitzky-Golay smoothing function for background correction.

Assessment of the bioactivity

In order to check the bioactivity, the obtained powders were immersed in simulated body fluid (SBF), in closable conical polypropylene tubes that were placed in an incubator at a constant temperature of 37 °C, under static condition for 7 days. The SBF was prepared according to Kokubo's protocol [19]. The solution was buffered at a pH of 7.4 at 37°C. The weight of glass per volume of SBF used was 10 mg/ml for each sample. After 7 days, the powders were filtrated, rinsed several times with distillate water, and dried.

RESULTS AND DISCUSSION

Structural Characterization

The XRD patterns disclose the amorphous structure of the samples after heat treatment. However, around $2\theta\sim 32^\circ$ could be observed some signals associated with a few crystallization centers. These suggest the formation of tricalcium phosphate phase, found as Ca₃(PO₄)₂ H₂O [20].

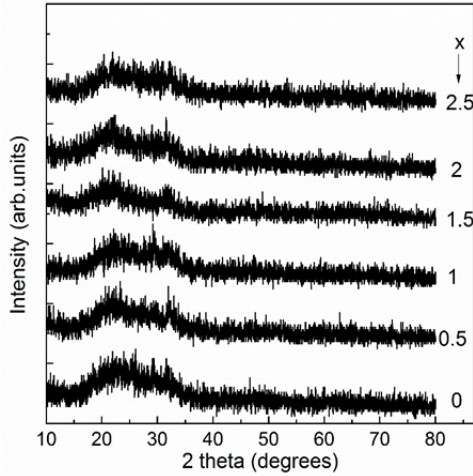


Fig. 1. XRD patterns of the $60\text{SiO}_2 \cdot (32-x)\text{CaO} \cdot 8\text{P}_2\text{O}_5 \cdot x\text{Ag}_2\text{O}$ (mol%) samples

In the FT-IR spectra could be observed absorption bands characteristic to Si-O-Si stretching (1040 and 860 cm^{-1}) and Si-O-Si bending vibrations (510 cm^{-1}). Water is displayed on the wide absorption signal around 1640 cm^{-1} . The band at 1440 cm^{-1} indicates the existence of the carbonate group and the 560 and 580 cm^{-1} signals prove the presence of the phosphate groups [20]. The recorded FTIR spectra do not show significant changes. This is most probable a consequence of the low content of Ag_2O .

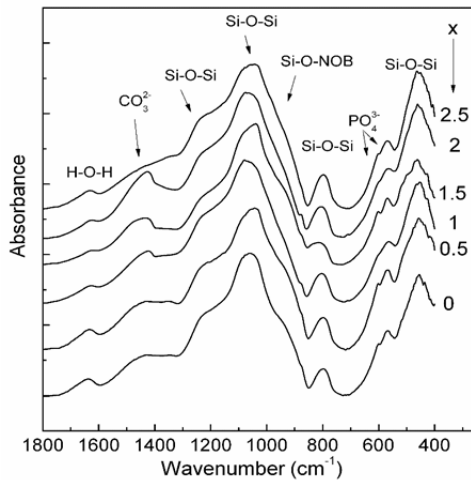


Fig. 2. FT-IR spectra of the $60\text{SiO}_2 \cdot (32-x)\text{CaO} \cdot 8\text{P}_2\text{O}_5 \cdot x\text{Ag}_2\text{O}$ (mol%) samples

Uv-vis spectra showed between 300 and 330 nm a signal occurred due to electronic transitions in Ag metallic species [21]. This signal increases in intensity as the silver concentration rises [22]. According to the literature, the silver doped samples could reveal surface plasmon resonance bands in the 400-500 nm as a result of the Ag nanoparticles presence [21, 22]. By analysing our Uv-vis spectra can be observed the occurrence of an absorption signal with a maximum at around 420 nm. This signal is most prominent on x=0.5 mol% Ag₂O sample and is associated with the existence of silver nanoparticles inside the glass matrix [22]. The shape of the band is asymmetric because another signal, which is due to the surface plasmon resonances of the agglomerations of Ag nanoparticles, is convoluted with that given by surface plasmon resonances of the isolated Ag nanoparticles. Once the silver amount increases one can observe a slight shift of the band around 420 nm towards 450 nm, as a consequence of either the increase amount of Ag nanoparticle clusters, or the rising of the silver nanoparticles dimension [21, 22].

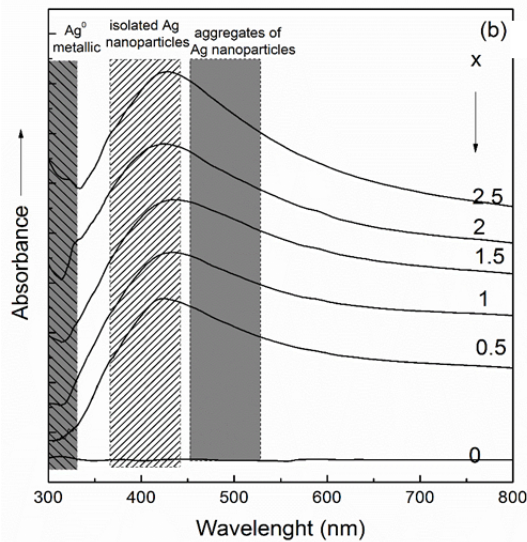


Fig. 3. UV-vis spectra of the 60SiO₂·(32-x)CaO·8P₂O₅·xAg₂O(mol%) samples

Assessment of the bioactivity

After 7 days of samples immersion in SBF, the XRD patterns reveals the occurrence of hydroxyapatite (HA) phase between the recorded signals at 2θ~26° and 32°. Likewise could be observed specific signals for silver chloride at 2θ~46°. To easily associate apatite and silver chloride phases, XRD pattern of HA and AgCl are included as references [23, 24] According to the literature, AgCl has no

negative effects on living organisms, moreover it is preferred in detriment of high silver nanoparticles concentration of [25].

In the FT-IR spectra of the samples immersed in SBF, the bands at 604 and 564 cm^{-1} show an almost proportional intensity at each concentration. This indicates a good bioactivity of all samples [20]. However, the sample with 0.5 mol% Ag_2O shows the highest bioactivity potential of all if we are taking into consideration also the absence of a high signal from AgCl .

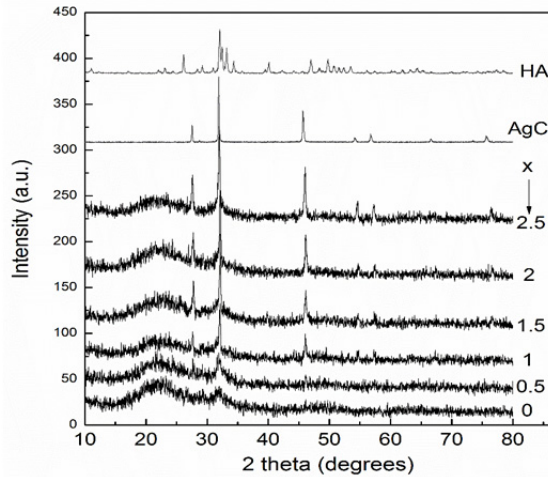


Fig. 5. XRD patterns of the $60\text{SiO}_2 \cdot (32-x)\text{CaO} \cdot 8\text{P}_2\text{O}_5 \cdot x\text{Ag}_2\text{O}$ (mol%) samples after immersion in SBF for 7 days. The XRD patterns of HA and AgCl are also included for comparison purpose

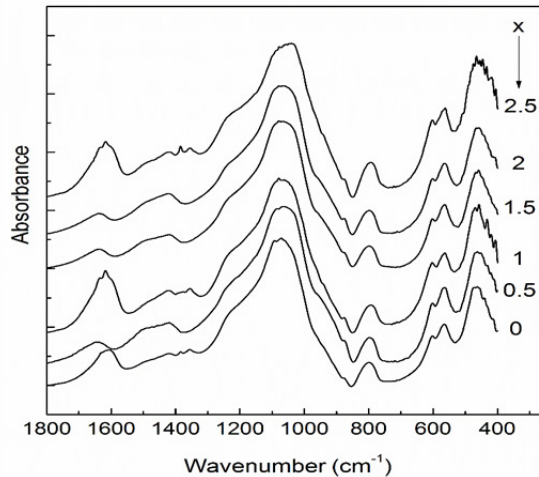


Fig. 6. FT-IR spectra of the $60\text{SiO}_2 \cdot (32-x)\text{CaO} \cdot 8\text{P}_2\text{O}_5 \cdot x\text{Ag}_2\text{O}$ (mol%) samples after immersion in SBF for 7 days

CONCLUSIONS

In this paper a wide range of compositions containing silver oxide were synthesized having $\text{SiO}_2\text{-CaO-P}_2\text{O}_5$ as a base formula. The obtained results guided us to sum the entire range of concentrations to a single one that was the most suitable for our future purposes.

The XRD patterns, FT-IR and UV-Vis spectra show structural characteristics that indicate the bioactive character of all investigated samples. Concentration with $x=0.5$ mol% Ag_2O proved to be the most suitable because of both the absence of an important amount of AgCl and its bioactive character. Thus, the composition that fits most of the requirements for its further use at scaffold fabrication is $60\text{SiO}_2\cdot 31.5\text{CaO}\cdot 8\text{P}_2\text{O}_5\cdot 0.5\text{Ag}_2\text{O}$ (mol%).

ACKNOWLEDGMENTS

This paper is a result of a doctoral research made possible by the financial support of the Sectoral Operational Programme for Human Resources Development 2007-2013, co-financed by the European Social Fund, under the project POSDRU/187/1.5/S/155383-“Quality, excellence, transnational mobility in doctoral research”.

REFERENCES

1. M. Catauro, M. G. Raucci, F. D. E. Gaetano, and A. Marotta, *J. Mater. Sci.: Materials in Medicine*, 5, 831 (2004).
2. C. Gruian, A. Vulpoi, E. Vanea, B. Oprea, H.-J. Steinhoff, and S. Simon, *J. Phys. Chem. B*, 117(51), 16558 (2013).
3. C. Balagna, C. Vitale-Brovarone, M. Miola, E. Verne, R. A. Canuto, S. Saracino, G. Muzio, G. Fucale, and G. Maina, *J. Biomater. Appl.*, 25(6), 595 (2011).
4. G. Kaur, O. P. Pandey, K. Singh, D. Homa, B. Scott, and G. Pickrell, *J. Biomed. Mater. Res. Part A*, 102(1), 254 (2014).
5. M. Miola, M. Bruno, G. Maina, G. Fucale, G. Lucchetta, and E. Vernè, *Mater. Sci. Eng. C*, 43, 65 (2014).
6. H. Zhu, C. Hu, F. Zhang, X. Feng, J. Li, T. Liu, J. Chen, and J. Zhang, *Mater. Sci. Eng. C*, 42, 22 (2014).
7. J. R. Jones, L. M. Ehrenfried, P. Saravanapavan, and L. L. Hench, *J. Mater. Sci. Mater. Med.*, 17(11), 989 (2006).

8. M. Catauro, F. Bollino, F. Papale, and S. Vecchio Cipriotti, *J. Non. Cryst. Solids*, 422, 16 (2015).
9. K. Glinel, P. Thebault, V. Humblot, C. M. Pradier, and T. Jouenne, *Acta Biomater.*, 8(5), 1670 (2012).
10. X. Chatzistavrou, J. C. Fenno, D. Faulk, S. Badylak, T. Kasuga, A. R. Boccaccini, and P. Papagerakis, *Acta Biomater.*, 10(8), 3723 (2014).
11. A. R. Shahverdi, A. Fakhimi, H. R. Shahverdi, and S. Minaian, *Nanomedicine Nanotechnology, Biol. Med.*, 3(2), 168 (2007).
12. K. H. Cho, J. E. Park, T. Osaka, and S. G. Park, *Electrochim. Acta*, 51(5), 956 (2005).
13. A. Vulpoi, C. Gruian, E. Vanea, L. Baia, S. Simon, H.-J. Steinhoff, G. Göller, and V. Simon, *J. Biomed. Mater. Res. Part A*, 100A(5), 1179 (2012).
14. S.-H. Luo, W. Xiao, X.-J. Wei, W.-T. Jia, C.-Q. Zhang, W.-H. Huang, D.-X. Jin, M. N. Rahaman, and D. E. Day, *J. Biomed. Mater. Res. Part B Appl. Biomater.*, 95B(2), 441 (2010).
15. K. Magyari, C. Gruian, B. Varga, R. Ciceo-Lucacel, T. Radu, H.-J. Steinhoff, G. Váró, V. Simon, and L. Baia, *J. Mater. Chem. B*, 2(35), 5799 (2014).
16. M. Bellantone, N. J. Coleman, and L. L. Hench, *J. Biomed. Mater. Res.*, 51, 484 (2000).
17. A. Vulpoi, V. Simon, H. Ylanen, and S. Simon, *J. Compos. Mater.*, 48(1), 63 (2014).
18. R. A. Popescu, K. Magyari, R. Stefan, I. Papuc, and L. Baia, *Stud. UBB Phys.*, 60(1), 103 (2015).
19. T. Kokubo and H. Takadama, *Biomaterials*, 27(15), 2907 (2006).
20. K. Magyari, L. Baia, A. Vulpoi, S. Simon, O. Popescu, and V. Simon, *J. Biomed. Mater. Res. Part B Appl. Biomater.*, 103B, 261 (2015).
21. L. Baia, D. Muresan, M. Baia, J. Popp, and S. Simon, *Vib. Spectrosc.*, 43(2), 313–318 (2007).
22. K. Magyari, R. Stefan, D. C. Vodnar, A. Vulpoi, and L. Baia, *J. Non. Cryst. Solids*, 402, 182 (2014).
23. Downs RT. The RRUFF Project: An integrated study of the chemistry c, Raman and infrared spectroscopy of minerals. In: Program and Abstracts of the 19th General Meeting of the International Mineralogical Association in Kobe, Japan; 2006. O03–13. RRUFF ID: R060180. <http://rruff.info/general5HA/display5default/R060180>,
24. Downs RT. The RRUFF Project: An integrated study of the chemis-try c, Raman and infrared spectroscopy of minerals. In: Program and Abstracts of the 19th General Meeting of the International Mineralogical Association in Kobe, Japan; 2006. O03–13. RRUFF ID: R050360, <http://rruff.info/chem=Cl,Ag/display=default/R050360>
25. S. Zhang, C. Du, Z. Wang, X. Han, K. Zhang, and L. Liu, *Toxicol. Vitro.*, 27(2), 739 (2013).